Thermoelastic Deflections of Thin-Shell Composite Space Structures

Thesis by
John Monroe Pederson, Jr.

In Partial Fulfillment of the Requirements for the
Degree of
Doctor of Philosophy

CALIFORNIA INSTITUTE OF TECHNOLOGY
Pasadena, California

2025
Defended October 29, 2024

John Monroe Pederson, Jr.
ORCID: 0009-0002-8500-2285

ACKNOWLEDGMENTS

Describing the impacts that so many brilliant people have had on this work through the enrichment of my life would be a Sisyphean task; no sooner would I exhaust the contribution of one before I would have to start afresh with another. But the mere attempt at such has left me happy, just as Albert Camus predicted in *Le Mythe de Sisyphe*. "Acknowledgment" is a fitting word, since all the words I could write are a mere mention compared to what each person listed has meant to me.

The first thanks must go to the instigator, co-creator, and inexhaustible aid to this undertaking – my advisor, Prof. Sergio Pellegrino. From the first day I stepped onto Caltech's campus (and right into his office) as a naïve undergrad, he has taken me under his wing and kept me on course to complete a fulfilling doctoral work. His experienced insight, unfailing direction, and quick wit have been the perfect support to this joint endeavor.

Eric Sunada, Lead Thermal Technologist in Propulsion, Thermal, and Materials Systems at the Jet Propulsion Laboratory, gave my advisor and I invaluable insight on the thermal experiments and modeling in this thesis. He provided the thinnest thermocouples used in this work, and even offered his student-program vacuum chamber for tests preliminary to those described here; to him I owe many thanks.

JPL also provided the experimental measurements of lamina and laminate properties used throughout the simulations herein; Emma Bradford provided those of surface emissivity and absorptivity, and Dr. William Warner provided the thermal expansion coefficients and specific heat capacities.

TA Instruments, specifically Justin C. Wynn, generously provided the isotropic measurements of our composite laminate's thermal conductivity in Appendix A.

Alexandra Haraszti, currently a graduate student at Stanford, contributed heavily to figuring out the refractive correction for the DIC measurements during her time as a SURF student at Caltech. The noise floor for our deflections is below 10 μm in large part due to her efforts as an exceptional experimentalist.

Alan Truong, research scientist in the Space Structures Lab, manufactured both types of unit structures tested in this thesis; his ability to deduce how to successfully co-cure a 12-μm layer of graphite with our already ultrathin laminates is a testament to his skill and dedication, and his work made this work possible.

Mike Kelzenberg, senior research scientist in the Atwater group at Caltech, also deserves a mention; he was the first person to suggest putting a smartphone thermal camera into the vacuum chamber and see if it *didn't* explode. This idea ended up being responsible for the bulk of the thermal data in this work.

My candidacy committee, composed of Prof. Beverley McKeon, Prof. Dan Meiron, and Prof. Ares Rosakis, provided helpful direction and questioning; each of their comments and later advice led to improved conclusions that are reflected in this work, for which I am quite grateful. My defense committee, composed of Prof. Dan Meiron, Prof. Guruswami Ravichandran, and Prof. John Sader, did the same.

My advisor has also created an incredible and brilliant team of lab members, all of whom I was fortunate enough to call my coworkers. This work would have been severely reduced in scope without their constant presence, guidance, support, and camaraderie. While everyone in the lab has played an important role in my time here, the following members deserve my specific thanks. Uba K. Ubamanyu's personable manner and teaching ability helped me very much in learning to use the DIC stereo camera rig; Armanj Hasanyan also contributed to lowering the noise floor of both our measurements in preliminary testing. Brayden Aller and Sahangi Dassanayake, members of my masters cohort, have also been a wonderful presence in and outside of the lab for my entire stay, and made my experience there even better.

The Caltech Space Solar Power Project, an effort between three professors' groups to beam solar energy from orbit to the Earth, has been a fascinating collaboration, and even contributed the subject of the culminating simulation in this thesis.

The administrators and staff of GALCIT also deserve thanks, as they made my time at the department run smoothly. Special mentions go to Jamie Meighen-Sei, Christine Ramirez, Liza Bradulina, and Sarah Pontes, all of whom made my graduate experience much better. I also thank Petros Arakelian for his help in maintaining the vacuum chamber and pump, as well other fixes and technical assistance.

The National Science Foundation's Graduate Research Fellowship Program and the Caltech Space Solar Power Project provided financial support for this research.

My mentors at Los Alamos National Laboratory played an instrumental role in convincing me to go to grad school, and aided many of the skills needed once I got there—even the background in Thermal Desktop used in this thesis. Alessandro Cattaneo, Troy Harden, Beth Boardman, David Mascareñas, and Chuck Farrar of the Dynamics Summer School, as well as Lee Holguin, Amy Regan, and Benigno San-

doval of ISR-5, deserve my utmost thanks. I must also individually thank Jonathan Ventura and Jeremy Best, whose small political-science talk at my undergrad started that chapter of my life.

For enabling me to read Henri de Sénarmont's seminal work on orthotropic thermal conductivity in the original French, I thank my teachers Mmes. Marie O'Donnell, Jane Murdock, and Mariana Schneller, as well as Prof. James Houlihan. *Merci de tous vos efforts*—the epigraph of the second chapter is for all of you.

For partly inspiring my Three Minute Thesis talk about this research with the beautiful poem *Failing and Flying*, I thank Jack Gilbert. I also thank Dr. Niyati Desai; her incredible talk the year before gave me the courage to give one myself.

To my entire GALCIT cohort, from 2019 to 2024, whose daily support made the completion of our first year of studies so much more manageable, as well as made these last few years so enjoyable. From a masters degree to a half-marathon, you have all helped me achieve the individually impossible, even unthinkable; you all will forever hold a special place in my heart.

To Tanner and Jessica Harms, Brayden and Kate Aller, Salvador and Heather Gomez, and Tinashe Handina, whose thought-provoking discussions and companionship have been highlights of these past two years; for you all I am indescribably grateful.

To my dearest 진은 (眞恩, "genuine grace"): our happiness together has been a true blessing. Your invaluable encouragement, as well as your passion for scientific work and elsewhere, have been among my greatest inspirations. There isn't a day that goes by without you adding yet another beautiful Impressionist stroke to the painting of our lives together; my heartfelt thanks and love belong to you.

To my loving parents and sister, whose support and positive example have been with me every day of my life, and filled it with inexpressible joy; your unwavering encouragement and love are the reason I've made it this far. I cannot express my love and gratitude in words, and therefore let the life you gave me be my witness.

To the force responsible for the ocean of mathematical beauty and scientific wonder all around us, of which this entire work takes joy in explaining but the tiniest drop, I owe a profound gratitude.

To all those I have forgotten to mention: you are the giants whose shoulders I cannot see, merely because I'm standing on them. No information is ever truly destroyed, and neither are the marks you have made on my life and this work.

ABSTRACT

As space structures become larger, lighter, and deployable, thermal deflections induced by sunlight become a significant source of structural inaccuracy and even spacecraft vibration. Studying these deflections is notoriously difficult: analytical solutions rapidly become intractable, experiments under vacuum and cooling are low-visibility and expensive, and multiphysics finite-element simulations are computationally demanding and usually don't account for coupled thermo-structural analyses and/or changing radiation view factors.

This work demonstrates key improvements in experimental methods and thermo-structural simulation of these thermal deflections. First, simultaneous full-field measurements of structural temperatures and deflections are achieved by constructing and using a custom vacuum chamber and heating setup; significant thermal gradients and repeatable thermal deformations are measured and analyzed, forming a ground truth for succeeding simulations. Second, multiphysics models of the experimental chamber are created in COMSOL Multiphysics and characterized, even accounting for residual convection, and used to inform prototype improvements and more advanced simulations. Third, based off such predictions, the unit structure prototype composite is improved by adding a layer of graphitized polymer film, with further experimentation showing a dramatic reduction in deflections.

Finally, the accumulated knowledge is used to simulate a satellite slew maneuver with realistic orbital heating; a custom technique to couple thermal (Thermal Desktop) and structural (Abaqus) finite-element software via a MATLAB script allows for the recalculation of radiation view factors during simulations, a feat necessary for accurate heating calculations on deployable structures. These results have immediate applicability in predicting structural temperatures and deflections during the satellite maneuvers proposed for the Caltech Space Solar Power Project, as well as suggesting critical improvements to ensure reliability and mission success.

PUBLISHED CONTENT AND CONTRIBUTIONS

[1] JM Pederson and S Pellegrino. "Thermal Deformation of Ultrathin Composite Structures in a Vacuum Environment." In: *AIAA SCITECH 2024 Forum* (2024). DOI: 10.2514/6.2024-0412.
J.M.P. participated in the conception of the project, performed the experiments and numerical simulations, analyzed the results, and participated in the writing of the manuscript.

[2] JM Pederson, A Haraszti, and S Pellegrino. "Thermal Deformation of Ultrathin Composite Structures in a Vacuum Environment." In: *AIAA SCITECH 2023 Forum* (2023). DOI: 10.2514/6.2023-1506.
J.M.P. participated in the conception of the project, performed the experiments and numerical simulations, analyzed the results, and participated in the writing of the manuscript.

TABLE OF CONTENTS

LIST OF ILLUSTRATIONS

LIST OF TABLES

Chapter 1

INTRODUCTION

"I've never been certain whether the moral of the Icarus story should only be...'don't try to fly too high,' or...'forget the wax and feathers, and do a better job on the wings.'"

Stanley Kubrick

To explore space, study the wonders of the cosmos, and better understand the processes of our own planet, structures that support such endeavors in space (trusses, solar arrays, antennae, etc.) are growing in size. As such missions push ever harder on the payload mass and volume constraints of the rockets used to take them to orbit, deployable structures have emerged as a promising field, efficiently packaging large lightweight structures into spaces too small for their rigid equivalents.

The ability to compactly coil and fold for the trip into space, as well as the ability to elastically unfurl and deploy once in orbit, generates high bending stresses, requiring the use of extremely thin, yet strong, materials that must also be lightweight. While metals such as steel and Elgiloy have been the standard (albeit non-lightweight) historic choices, the entire combination of desired properties is best met by carbon-fiber and glass-fiber composite laminates. The incredibly high tensile strength of carbon fiber allows for incredibly thin material thicknesses—the plies in this work, for example, do not exceed 30 μm—while the toughness of even thinner plain-weaves of glass fibers, as well as that of the thermoset epoxy matrix that binds them together, allows for robust and repeated handling. Having successfully flown and deployed on several recent missions, composite deployable space structures are therefore the architecture considered in this work.

1.1 Thermal Effects in the Space Environment

However, the thermal environment of Earth orbit and beyond proves a particularly punishing one for large thin structures. In the total absence of convection, conductive and radiative heat transfer dominate, meaning that sunlight and the cold background of space can induce extreme temperatures across structures; such heat loads can

even rapidly fluctuate during orbital maneuvers or planetary eclipses. The resulting structural temperature changes and gradients cause unbalanced thermal expansions and contractions, which in turn cause significant local and global deformations, and even vibrations if the heating profile changes with the structure's local orientation [41]. Structural geometric inaccuracy, spacecraft pointing difficulty, and even cyclic material fatigue are all undesirable side effects of these phenomena if left unchecked.

Thus, long after the legendary flight of Icarus, whose wax-and-feathered wings were no match for the intense rays of the sun, thermal effects on large spacecraft "wings" (structures) still remain undefeated. Harmful effects of thermal imbalances have unfortunately plagued space missions for the last sixty years and counting; at least two dozen recorded spacecraft have encountered problems ranging from unexpected nutation to thermoelastic vibrations on long panels and booms [47]. The most high-profile example of such mission-critical performance issues would be that of the Hubble Space Telescope, specifically its original large deployable solar arrays shown in Figure 1.1. Each time the telescope exited the shadow of the Earth on orbit, the sudden heating of one side of the arrays created thermal expansions, bending and torsional deflections, and even thermally induced oscillations [16]. Such unpredicted interference exceeded the ability of the pointing system's reaction wheels to compensate, jeopardizing Hubble's ability to hold sufficient pointing control to perform cutting-edge Deep Field measurements [9]. Most notably, the problem was not ultimately solved by more advanced deployable arrays—though redesigned ones were outfitted and tried—but by replacing them a second time with rigid photovoltaic panels [31].

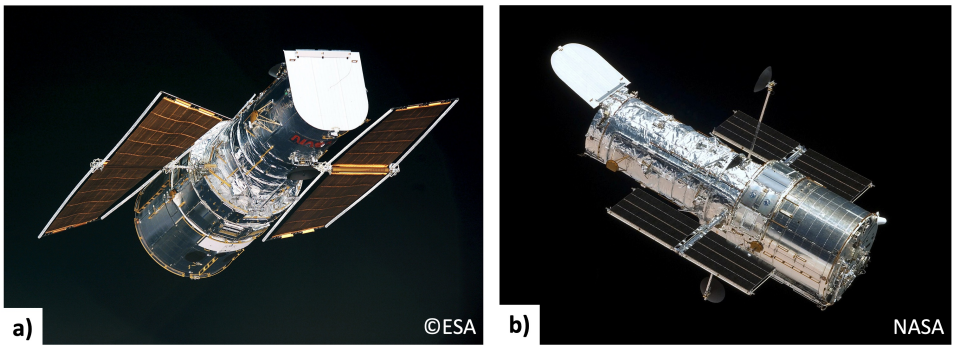

Figure 1.1: a) The Hubble Space Telescope with its second set of deployable solar arrays, and b) with its final rigid solar panels. a) copyright ESA.

One putative solution to these thermal control issues would be to construct the structures of material with better thermal properties; composite laminates appear to

have a decisive advantage in this area, since carbon fibers are known to have lower coefficients of thermal expansion than most metals [18], and when constructed with specific combinations of laminae, ultralow CTE's are theoretically possible to achieve [27]. However, the full laminates often have higher CTE's due to the presence of glass fibers and matrix [14, 19]; in addition, the thermal conductivities of carbon-fiber thermoset composite laminates are much lower than most metals, often by over two orders of magnitude [50]. In addition, manufacturing defects and imperfections are ever present; these three properties together mean that if heated, many composite booms may actually experience thermal deflections similar to or greater than metallic booms, a result of the increased thermal gradients overriding other considerations [38].

1.2 Thermal Deflection Prediction

To reduce or eliminate thermally induced deflections, designers and engineers must first understand their causes and contributing factors; in this vein of inquiry, accurate predictions and modeling are paramount. The main avenues of correctly predicting structural temperatures and deflections are laboratory experiments, analytical models, and finite-element simulations; each of these have advantages and drawbacks as discussed below.

Analytical Methods

Analytical models are a good starting point for understanding the temperature fields of structures, especially those of simple geometries like booms of regular cross-section. Many analytical calculations regarding spacecraft can be found in the influential *Thermal Structures for Aerospace Applications* by Earl Thornton; examples include derivations of steady-state and transient temperature fields for single illuminated booms, as well as quasi-static and dynamic deflections of the same [47]. Analysis can even be extended to dynamic analyses of the Hubble Space Telescope's blanket arrays, which were able to predict observed global torsional buckling [29], as well as closed-loop dynamics of thermal shocks on large structural beams [3].

Explicit energy balances involving conduction and radiation allow for an exact comparison of the relative contribution of each term, yielding much intuition into which factors are most significant. However, when the effects of material orthotropy, heat conduction in two or three dimensions, or internal boom radiation are considered, much less any complicated structural geometry, the equations become intractable

enough to require numerical solutions. However, some workarounds to this intractability are possible: for example, singular value decomposition of thermal systems offers a means to simplify transient temperature fields, reducing the required number of differential equations to be solved [52].

Finite-Element Models

Finite-element modeling (FEM) is able to continue where analytical calculations leave off; by discretizing the geometry into regular, well-characterized elements, the issues of multi-dimensional heat flow and radiation, and even complicated geometry, vanish at the expense of increased computational time. To account for temperature-induced deformations, one must use either a separate solid-mechanics finite-element solver (such as Abaqus) or a multiphysics finite-element software (such as COMSOL Multiphysics). Care must also be taken, just as with analytical models, that all relevant forms of heat transfer and material characteristics are accounted for. Such a diverse set of factors can include such things as conduction through fasteners, potting material, and unrelated components of the structural frame—factors that, if unaccounted for, lead to noticeably different model results [37].

Finite-element models have been used to great effect in analysis and prediction of real structures; such models are typically used to examine simulated structural behavior in realistic environmental conditions, or to explain observed behavior and data from actual spacecraft measurements. An example of the former would be Stohlman and Loper's simulation of steady-state deflections of Triangular Rollable and Collapsible (TRAC) booms, including those used on The Planetary Society's Lightsail-A; the effects of a vapor-deposited coating and a simulated composite with low coefficient of thermal expansion were analyzed, with recommendations made for future construction efforts [42]. As for the latter, an analysis of the Air Force Research Laboratory's Roll-Out Solar Array (ROSA), carried out by Chamberlain, Kiefer, and Banik, analyzed the array's split-cylinder composite booms to determine the deflection and vibration modes induced by sunlight exposure under orbital conditions; their analyses included explanations of structural modes and behavior based on embedded accelerometer and photogrammetric data [5].

Recalculating Radiative Heating

Simulating the coupled nature of temperature and deflection fields, however, is a road much less traveled in the field of space structures modeling, due to its inherent com-

plexity and computational demands. For long structures undergoing large enough thermally-induced deflections, the angle and location of a given finite element can change enough to invalidate the initially calculated local heating environment; for example, an initially straight rod lit by perpendicular sunlight can bend so much that sunlight is no longer perpendicular to elements far from the root, affecting their local heating rates. Similar effects can be induced by self-shadowing, i.e. when some structural elements shield others from the sun; studies on such effects show significant alterations in thermal deflection behavior and therefore must be accounted for [24][48]. In at least one of these, planar structures facing the Earth were found to be particularly at risk [49].

For maximum accuracy in modeling large deformations, therefore, the simulation must recalculate the radiative view factors for each element during the analysis. While some multiphysics software, like COMSOL Multiphysics, can perform this recalculation during a coupled thermo-structural analysis, such capabilities are limited to dynamic analyses and can fail to converge on non-trivial timescales, as shown in Section 5.1. Dedicated heat transfer simulations such as Thermal Desktop are able to recalculate view factors on demand, and therefore provide a promising ability to exploit when coupled with a dynamic deflection simulation. The details and capabilities of this approach, pursued by Stohlman in 2018 and the present work in 2024, are explained in Chapter 5.

1.3 Experimental Difficulties

Experiments offer an escape from tedious accounting for all possible contributing factors, but introduce new difficulties of their own. While offering the most direct means of measuring and observing thermo-structural effects in real-time, experiments involving significant structural deformations can be difficult to execute in a useful manner. To achieve larger deformations with a high signal-to-noise ratio, the structure must either be long (i.e. meters in scale) or the inducing temperature gradients must be high. The latter not only requires heat lamps or solar simulators, but almost always necessitates a vacuum chamber to avoid convective cooling; thin structures are especially sensitive to convection, owing to their low thermal inertia. If space-like temperatures are desired, cryogenic substances (usually liquid nitrogen) must be used to cool the vacuum chamber and/or an internal radiation shroud, increasing both the cost and complexity of experimentation.

In addition, many typical data acquisition devices such as cameras and laser distance

sensors cannot operate in vacuum and/or cryogenic temperatures, and the ones that do are often necessarily placed too close to see the entire structure. These constraints tend to make structural measurements either impossible or only available from limited angles, meaning that few studies attempting such measurements are able to obtain experimental deformations at all. For example, one such study on thermal analysis of lenticular booms used many thermocouples to provide measurements of the boom's temperature field, but owing to the limited visibility and harsh environment inside the chamber, could not measure boom deflections at all [2]. Another example used three cameras and a line of heat lamps placed in a large chamber with a four-meter boom, but only the motion of the boom tip was accurately able to be traced [43]. In fact, such behavior completely diverged from any simulation prediction, showing the unfortunately tenuous nature of relating current state-of-the-art experiments and simulations.

For comparison of experimental data to simulation results, a full deflection field, as well as a full temperature field, would therefore be an ideal unattainable by previous measurement techniques. That ideal is something the current work has accomplished, achieved by expanding certain experimental abilities and relaxing constraints.

1.4 Research Objectives and Outline

The goal of this work is simple: to provide a pathway to reduce or eliminate thermally-induced deflections on thin-shell composite space structures, and use the knowledge to model a thermally realistic satellite maneuver. But to reduce these deflections, we must first accurately predict and model them, and to accurately predict and model deflections, we must first accurately measure them in experiment. This chain of events—measuring, modeling, and reducing—is what this work provides for an example modular thin structure; these improvements are then used directly in a simulation for a larger structure in the space environment. This work therefore addresses these areas in the following chapters.

Chapter 2 shows how full-field measurements of temperatures and deflections of structures were possible to experimentally achieve in a low-vacuum environment. After an in-depth discussion of the measurement devices used, as well as the hardware required to create useful thermal boundary conditions, a testing procedure is outlined and the resulting full-field measurements analyzed.

Chapter 3 seeks to replicate these experimental results *in silico*, using COMSOL

multiphysics models to predict temperatures and deformations. A higher-fidelity 3D model predicts the contributions of the experimental rig as a whole, while a 2D cross-section model dives into the effects of residual convection in the setup. Finally, the shortcomings of these modeling approaches are countered with a second methodology of deflection prediction, one that uses non-contact temperature measurements to provide thermal loading for simulated deformations.

Chapter 4 draws on the modeling knowledge gained in Chapter 3 to reduce structural deflections by modifying the structural laminates themselves. A highly conductive graphite-polymer layer is added to the laminate during manufacture and shown to reduce simulated structural temperature gradients and deflections, effectively spread heat in a lab sample, and positively affect performance in a full structural module prototype.

Chapter 5 extends the multiphysics models of Chapter 3 to realistic structural lengths and orbital heating loads. Large-scale COMSOL simulations provide significant insight into the effects of thermal and structural material properties, making use of the advancements in Chapter 4. To address the inability of these simulations to handle radiation view-factor recalculation, a bespoke coupled thermo-mechanical simulation is presented, showing how to successfully combine the deflection analyses of Abaqus with the thermal predictions of Thermal Desktop in a single coupled computation. This technique allows for the successful simulation of one of the most challenging thermo-structural cases: a two-meter deployable structure slew maneuver requiring transient thermal and dynamic deflection analyses.

Chapter 6 concludes the work by summarizing the achievements, benefits, and drawbacks of the included research, as well as providing areas for future direction and work that would carry on the promising findings and apply them to the design of future deployable composite space structures.

Appendix A provides a summary of the method used to determine the in-plane orthotropic thermal conductivity of thin materials, including the composite laminates used in this work. Continuous laser heating of a sample is used to produce a transient and steady-state temperature field measured by a thermal camera; this field is then recreated in a multiphysics simulation of the setup via a parametric search of the laser heating characteristics and orthotropic sample conductivities.

Appendix B provides a brief inquiry into the thermal buckling demonstrated in Chapter 5, presenting a partial eigenvalue analysis of the stiffness matrices of two

structural finite-element models. Connections to existing eigenvalue buckling analyses and suggestions for future improvements are included.

Chapter 2

FULL-FIELD MEASUREMENT OF TEMPERATURE AND DISPLACEMENTS OF STRUCTURES IN LOW VACUUM

"...ce que je vois là n'est qu'une écorce.
Le plus important est invisible."
"...what I see there is only a shell.
What's most important is invisible."

Antoine de Saint-Exupéry,
Le Petit Prince

To experimentally measure the temperature and deflection fields experienced by realistic thin-shell space structures, several practical challenges must be overcome, each of which is given a section below.

The first challenge is picking a target structure that is small enough to fit in a manageable laboratory setup for controlled heating and measurements, yet large enough to exhibit behaviors representative of and able to be extrapolated to a larger structure. A module, or unit, of a structure made of repeated units would be an ideal choice, and it is the one made here: a 25-cm section of a two-meter prototype of the structural architecture proposed for the Space Solar Power Project [11], as detailed below.

A second challenge lies in the testing rig itself, pitting the conflicting requirements of full-field measurement techniques (i.e. ones requiring cameras) against those of replicating realistic heating loads of the space environment. While cold radiative boundary conditions, radiative heating, and convection-free environments are all readily achievable in dedicated thermal vacuum chambers, such apparatuses have very limited interior visibility. This often precludes the use of exterior cameras at all, much less the stereoscopic ones needed for out-of-plane measurements, while cameras mounted inside the chamber must handle extreme temperatures and vacuum. By abandoning the standard metal chamber in favor of an acrylic one, and slightly relaxing the temperature requirements, both restrictions on cameras were lifted, enabling the use of external cameras for stereoscopic deflection measurements and an internal infrared camera for thermal measurements.

Due to all of these considerations, obtaining full-field measurements of temperature and deflection requires a complete re-design of the standard thermal vacuum testing setup, the details of which are presented here.

2.1 Background and Previous Setups

The experimental rig featured in this work was the culmination of various iterations and improvements on previous setups, each of which reduced or eliminated some factor that would interfere with measurements on realistic thin-shell structures.

The first such experiments merely involved placing a steel tape measure section (a "tape spring") in front of a quartz infrared heater bulb, both mounted vertically on the lab bench. When this setup proved too sensitive to convective effects and room air currents, the setup was surrounded by protective walls; when these walls proved sufficiently airtight to heat the air and thus constantly change the room temperature boundary condition, the setup was placed inside the acrylic vacuum chamber used in this work.

Details on experiments and results achieved in this setup are fully documented in a previous work [37], but the main takeaways are as follows. With this setup, illustrated in Figures 2.1 and 2.2, full-field deflection measurements on a tape spring were able to be measured due to the perfecting of the DIC rig setup and calibration process. However, without any chamber cooling or focusing of the bare infrared bulb, the chamber was heated significantly during testing, causing a slow but steady temperature rise that made assigning thermal boundary conditions in the corresponding COMSOL model difficult. In addition, such heating made repeatable "steady-state" conditions impossible, even after several hours of consecutively testing trial after trial. This limitation is the reason why the trials in the current work are all "transient" tests, with starting temperatures and heating rates carefully controlled to be as identical as possible between runs.

Further detailed in the same paper are tests performed at the Jet Propulsion Laboratory, under the auspices of chief thermal technologist Eric Sunada. As shown in Figure 2.3, a similar rig was placed in a large steel rectangular thermal vacuum chamber, one capable of much higher vacuum than the acrylic chamber used in the present work. As such, temperatures measured on the structure were about 20°C higher than tests performed in the acrylic chamber. However, the deflection able to be measured in such a low-visibility chamber was limited to a single-point measurement of the tape spring tip, one captured by using a Keyence laser distance sensor

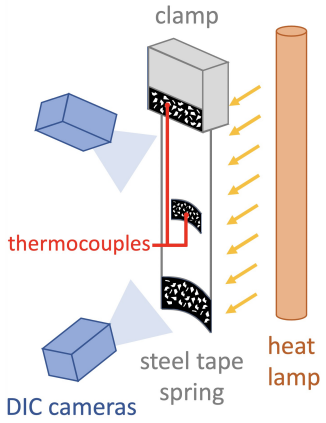

Figure 2.1: Figure from [37], showing a previous experimental setup cartooned with vertical axis not to scale. Note the placement of thermocouples on the middle of the tape spring and the clamp.

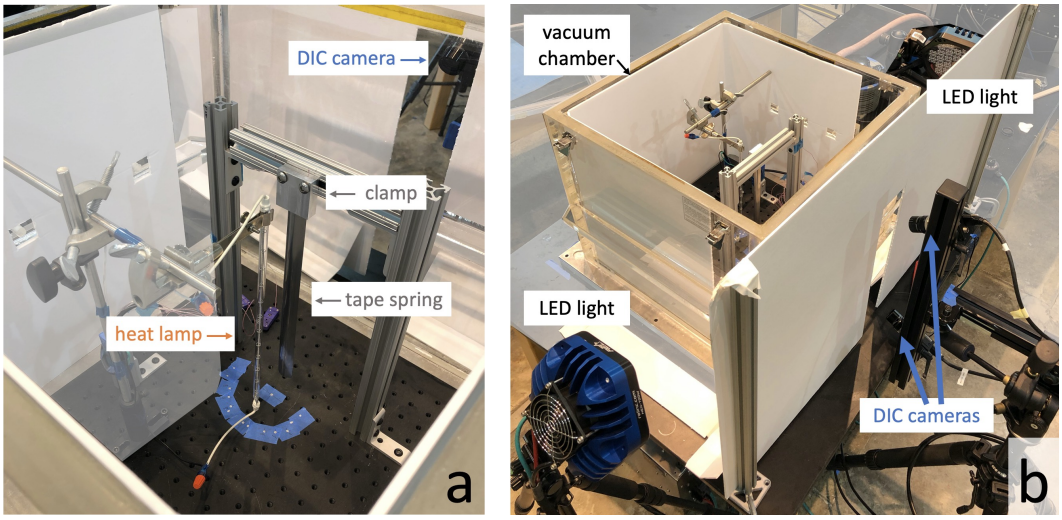

Figure 2.2: Figure from [37], showing a) a previous experimental setup in the acrylic vacuum chamber (note the heat lamp and a tape spring hanging vertically), and b) the LED lights and DIC cameras aimed through slits in the lightbox. Both views are missing the acrylic chamber lid and top lightbox panel for clarity.

that "shot" through a 2" optical feedthrough window. While such measurements were extremely inconsistent, probably due to the epoxy holding the tape spring being strongly affected by the high tape temperatures encountered—an effect entirely eliminated for the current work—even consistent measurements would regardless have been of extremely limited use, since they cannot offer much insight into the thermoelastic deflections over the entire structure. The same logic goes for the temperature measurement obtained from the single thermocouple present on the tape

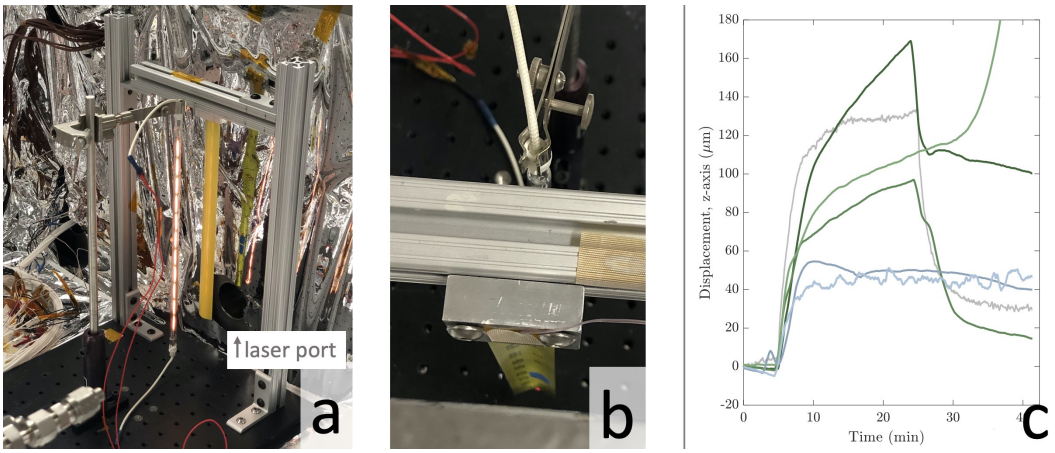

Figure 2.3: (a) Figure from [37], showing another previous experimental setup, performed at JPL. A Keyence laser distance sensor "shoots" through the feedthrough window hole behind the tape tip. (b) The same tape from above, showing the glint of the laser dot pointed at the tip. (c) The deflection readings from various tests, showing wide variation in magnitude thought to be from potting epoxy overheating and potentially delaminating.

spring; it is of much less use than the full-field temperature measurements sought after and obtained in the present work.

2.2 Experimental Setup

For the current work, the sample representative unit structure, or module, was subjected to radiant heating and cooling conditions in a near-vacuum environmental chamber, and its resultant deflections measured by a stereoscopic camera apparatus via Digital Image Correlation (DIC). To achieve maximum thermal gradients and resulting deflections, the structure was heated with radiant energy from a quartz-infrared heater (QIH) bulb (Ushio #1001287), reflected by a two-part reflector into a collimated flux, and a cold plate was mounted behind the structure on the opposite side from that illuminated by the heat lamp. The entire setup is modeled and photographed in Figure 2.4.

The purpose of the environmental chamber was not to simulate the high vacuum of space, but rather to reduce the level of convection below an acceptable threshold; hence, "vacuum" was only achieved to the degree of 95 kPa below ambient pressure, or around 4-5% atmosphere. The ramifications of this residual atmosphere are fully discussed in Section 3.2.

The equipment used to produce the heating conditions on the unit structure were

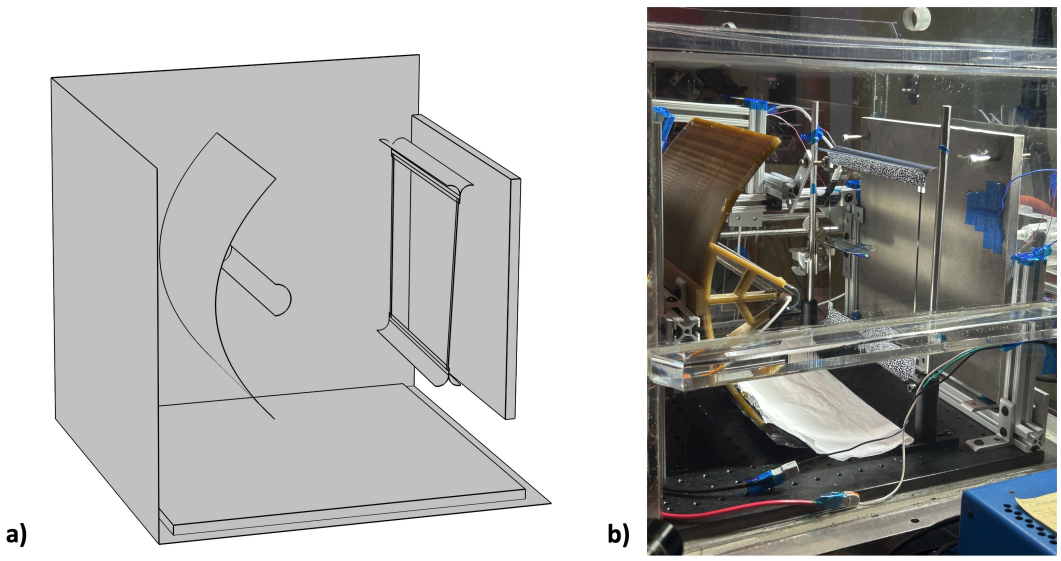

Figure 2.4: a) The experimental chamber modeled in COMSOL and b) as photographed in the laboratory.

custom manufactured for these tests, and are hence described here for clarity.

Structure Selection and Fabrication

A section of a much larger structure was chosen as a structural unit – namely, a two-meter prototype of the structural architecture proposed for the Space Solar Power Project [11]. The DOLCE portion of the SSPD-1 mission was designed with the express purpose of demonstrating the structure's ability to coil, stow for launch, uncoil, and dynamically deploy in Earth orbit; to accomplish this, the trapezoidal "strips" of the architecture can fold on top of themselves accordion-fashion, then coil around a central hub like a tape measure for storage and launch. Figure 2.5 illustrates how the section/unit chosen for this study comprises these trapezoidal strips; two Triangular Rollable and Collapsible (TRAC) longerons are connected via multiple carbon-fiber battens, forming a ladder-like structure. For the SSPD-1 prototype, the spacing between the TRAC longerons is 20 cm, while the batten spacing is alllowed to vary depending on the total strip length and position.

The unit structure studied in this work is a 25 cm by 25 cm section of the trapezoidal strip, comprised of two TRAC longerons connected by two battens spaced 20 cm apart – see Figure 2.5. Despite its small size, this simplest basic unit of the architecture still allows for a realistic representation of how the strip as a whole behaves; its full-size longerons and battens, manufactured and bonded using identical techniques to the real prototype, conduct heat and transmit force identically to the flight model.

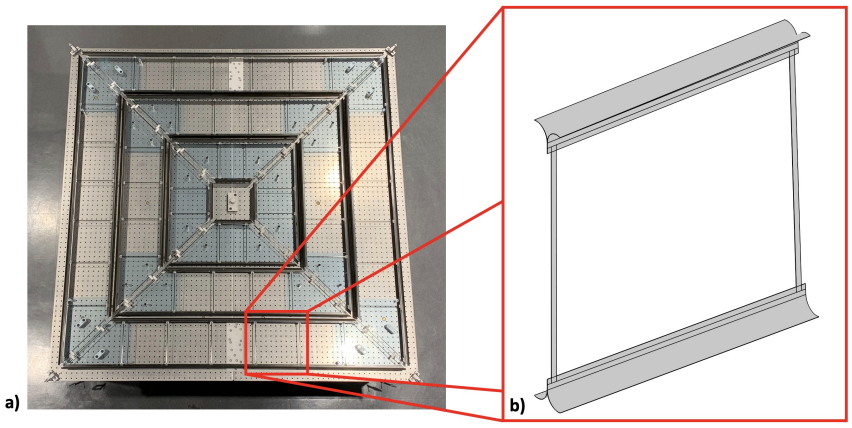

Figure 2.5: a) The SSPD-1 structural framework, made of trapezoidal "strips"; b) COMSOL model of a representative unit of the larger strip.

The ultrathin composite materials used in the strip's construction are of particular interest, owing to their unique thermal and structural properties. While the battens are simply off-the-shelf pultruded carbon-fiber rods of rectangular cross-section [46], as detailed by the SSPD-1 team [11], 25-gsm glass-fiber plain-weave prepreg and 30-gsm unidirectional carbon-fiber prepreg sheets were combined to manufacture the TRAC longerons; the curved longeron flanges are a three-ply laminate of the form [±45 GFPW / 0 UDCF/ ±45 GFPW], while the "web" connecting them is a seven-ply laminate of the form [±45 GFPW / 0 UDCF / ±45 GFPW 3 / 0 UDCF / ±45 GFPW]. Effectively, the web is formed of the two flanges bonded together edgewise with an additional GFPW lamina in between. The structural properties of the constituent laminae are detailed in Table 2.1.

The unit structure sample for the present study was fabricated in-house using the same techniques and procedures required for the SSPD-1 DOLCE flight model; the 7-ply laminates comprising the longerons were constructed of prepregs cured in an autoclave around aluminum molds, then trimmed to the final flange angle and longeron length [11]. The battens were then secured to both longerons using single-ply glass-fiber plain-weave tapes, the corners of which are visible in the final product shown in Figure 2.6.

Deflection Measurement via Digital Image Correlation

Digital Image Correlation (DIC) was employed to measure the deflections of the structure before, during, and after heating. A stereoscopic two-camera rig allowed for out-of-plane deflections—i.e. the key direction of interest—to be resolved within a

Table 2.1: Lamina/laminate material properties. Most structural properties are provided separately for each lamina, while starred structural properties and all thermal properties were determined via testing on the cured laminate.

Glass-Fiber Plain-Weave		**Unidirectional Carbon Fiber**	
E_1, E_2, E_3	23.8 GPa	E_1, E_2, E_3	128, 6.5, 6.5 GPa
$\nu_{12}, \nu_{13}, \nu_{23}$	0.17	$\nu_{12}, \nu_{13}, \nu_{23}$	0.35, 0.0178, 0.0178
ρ	1770* $\frac{kg}{m^3}$	ρ	1770* $\frac{kg}{m^3}$
t	25 μm	t	30 μm
[±45 GF/0 CF/±45 GF] Laminate			
	k	0.66 $\frac{W}{m \cdot K}$	
	$CTE_{12,13,23}$	25.9, 19, 19 $\times 10^{-6}$ $\frac{1}{K}$	
	ϵ	0.89	
	c_p	461 $\frac{J}{kg \cdot K}$	

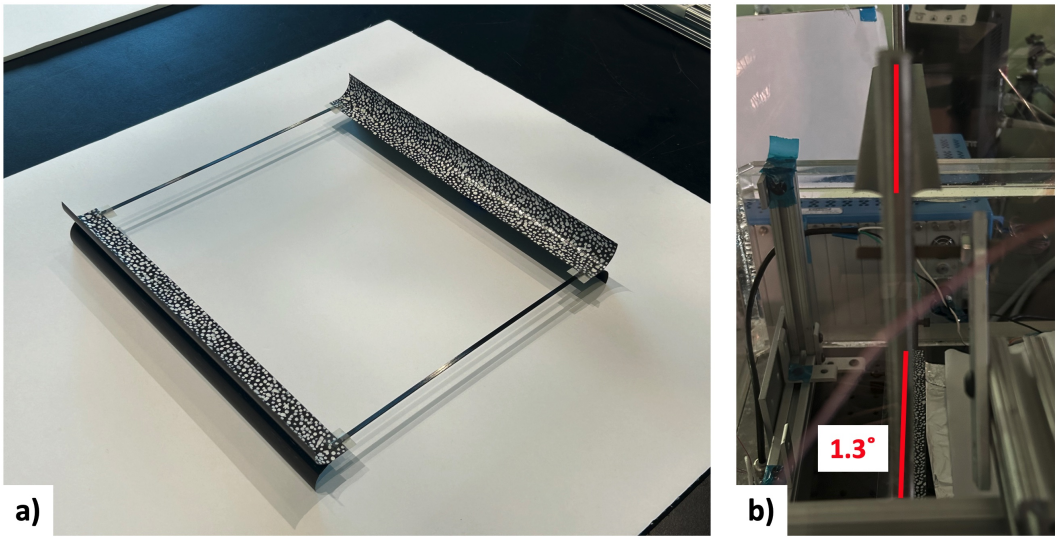

Figure 2.6: a) Sample unit structure as fabricated; b) as mounted inside the chamber. Web lines superimposed in red, illustrating a 1.3° twist manufacturing defect.

margin of under 10 μm; the rig is detailed in Figure 2.7. Two Point Grey Grasshopper cameras (GRAS-51S4M-C), each with a resolution of 2448 × 2048, 3.45 μm pixel size, and a gain range of 0 dB to 48 dB, were fitted with 12 mm lenses with an exposure time of around 6 ms. To provide the required high-contrast uniform illumination required to keep projection and other errors low, two large LED arrays (REL, Inc., WS3 7.5" visible spectrum model) were mounted outside the chamber pointing at the lamp reflector. Reflecting the LED light off the metallic surface off-axis in this way was an effective means of diffusing the light over the sample, while

also avoiding the reflections off the acrylic exterior encountered when pointing the lights toward the speckled side of the structure.

Deflection results are only as good as the calibration used to obtain them; therefore, the large refractive effects produced by the thick acrylic walls of the vacuum chamber made the calibration process nontrival. Furthermore, the chamber walls actually bow inwards while supporting a vacuum, causing a distortion that could not be calibrated out while the chamber was open. Much effort was spent developing a corrective procedure, the details of which are similar to those described in [37]; after calibrating with a large rigid grid in the standard way, a Variable Ray Origin (VRO) solver was applied to account for the large refractive interface between the cameras and the calibration grid. The structure at rest was then carefully recorded for several minutes before and after applying a vacuum, before the lamp apparatus ever applies a heat load; this allowed a baseline amount of erroneous deflection to be obtained, which was then subtracted from all future results to obtain the final deflection results.

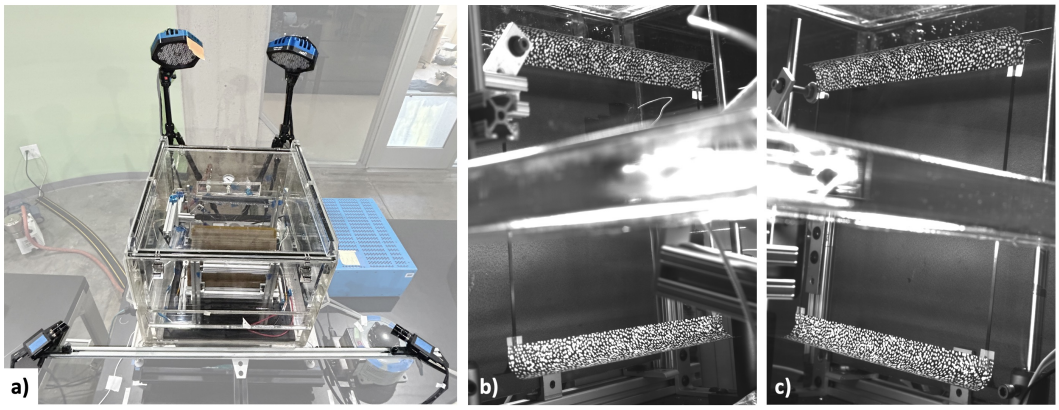

Figure 2.7: a) The stereoscopic DIC rig, cameras at bottom, LED lights at top; b) left camera view; c) right camera view. Note large translucent chamber rib in both views.

Temperature Measurement via Infrared Camera

A compact portable wide-angle infrared (IR) camera (Hikmicro Mini2 W) was mounted inside the chamber to optically measure temperature fields on the structure. Operated via smartphone and designed for ambient conditions, the camera was selected for the best chance of surviving the low pressures of the vacuum chamber; its lack of internal battery, as well as its low power consumption (0.36W), avoided two major electronic risks in vacuum—bursting and overheating in a convection-

less environment. Non-uniformity corrections and calibrations are automatically performed by the camera every 30 seconds, with the emissivity set to the structure's laminate's experimentally determined value of 0.89.

For each trial, an image was captured and a 2-minute video recorded every 135 seconds, ensuring that the turning on and turning off of the lamp were recorded on video. Measurement tooltips were placed on the points of the top and bottom longeron that were expected to be hottest from prior simulation (i.e. at the inner edge of each flange), as well as on the thermocouple recording the cold plate's temperature, making a total of three temperatures visible in real-time during testing.

The resulting images were processed using Hikmicro Analyzer; since videos cannot be analyzed in this software, the videos were processed using a custom MATLAB script to read the tooltips using optical character recognition; this enabled the plotting of the three temperatures of interest over time, as shown in Figure 2.14.

Collimated Radiative Heating via Lamp Reflector

The QIH heat lamp and its accompanying reflector mimic the effect of sunlight on the structure by producing a infrared/visible-wavelength heat flux in a collimated areal beam. The intensity of the QIH heat lamp was adjusted via a variac (variable AC transformer); while the wavelength profile slightly changes with a change in input power, the amount was deemed irrelevant for these tests.

Lamp Reflector Design

The reflector consists of two reflecting surfaces mounted with their foci along the lamp axis. The larger reflector is a parabola of width 12" and depth 3", with the focus in the plane of the parabola tips; this profile was chosen to make proper focal alignment visually straightforward. This larger reflector was additively manufactured from PEKK polymer; the material was chosen for its high temperature resistance and low outgassing, both of which are critical for high-temperature operation in a vacuum chamber.

The smaller reflector is a polished aluminum pipe, the inside surface of which forms a cylindrical reflector. Its purpose is to direct all lamp energy emanating in the forward direction backward towards the larger reflector, ensuring that all lamp radiation reaching the structure has been collimated: see Figure 2.8 for illustration. The drawback of this solution is a "dead band" of no radiant energy produced directly in the shadow of the smaller reflector; however, the only portions of the structure

affected by this shadow are two short sections of the battens, whose stiffness prevents any significant thermoelastic response regardless.

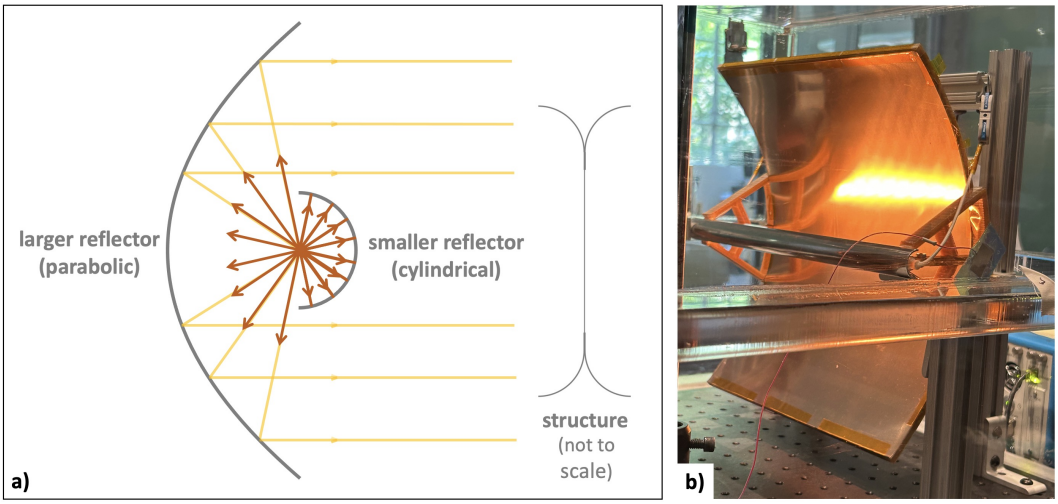

Figure 2.8: a) 2D ray diagram of the two-part heat lamp reflector; b) as-built reflector.

Experimental Verification of Lamp Profile

After being assembled, the as-built heating profile of the lamp was ascertained in the experimental chamber under near-vacuum. The acrylic walls of the chamber completely block infrared light, rendering traditional infrared camera techniques useless. Instead, a thermochromic film was suspended in front of the lamp in the same manner as the plane simulated previously; this polyester film was coated with a liquid crystal calibrated to change from black to red to green to blue to black as it passed from 45°C to 50°C, as seen in Figure 2.9. While the non-zero conductivity of the film renders the temperature profile on its surface a combination of radiative heating and conduction through the film itself, the latter's undesired contribution was mitigated by the polyester's low thermal conductivity (an order of magnitude lower than the composites comprising the unit structure). Results of testing show that the lamp flux was less uniform than desired, as shown by the uneven bands of color appearing on the film; however, the blue bands visible at top and bottom of the film were aimed precisely to match the two longerons of the structure, enabling the hottest regions of the lamp output to be focused on the sample itself. Such focusing allowed for the lamp power to be used more efficiently for the ensuing experiments.

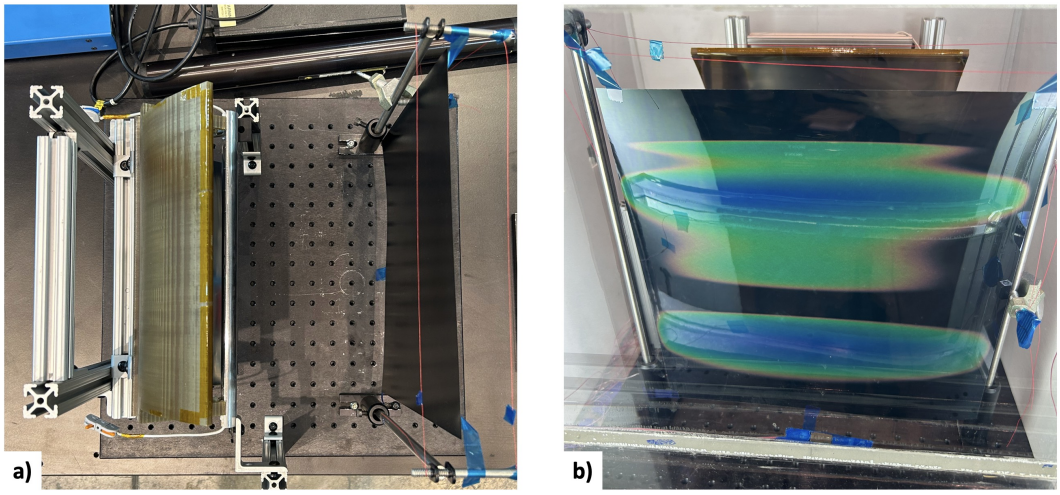

Figure 2.9: a) Thermochromic film mounted in front of reflector; b) the resulting visualization of the in-chamber temperature field.

Cold Boundary Condition

Chilled shrouds are regular features in many contemporary thermal vacuum chambers, as they offer an unmatched ability to control thermal environments. They provide a means of removing heat from the heating devices and components being tested, as well as maintain a constant radiative boundary temperature that simplifies predictions and multiphysics modeling of the experiment; they accomplish this through highly-emissive surfaces cooled via water or liquid nitrogen pipes on their back surfaces. However, their operational complexity, interfacing requirements, and (in the case of liquid-nitrogen-cooled shrouds) use of consumables adds significant time and cost to any experiment using them, as well as further complicating the experimental rig.

In the case of our study, which relies on thermal gradients to produce deflections, such a shroud was predicted to greatly improve the magnitude and amount of such deflections by driving down the low end of the temperatures reached on the structure. Such cool temperatures are reached on the back, unheated side of the structure – specifically the longerons' back flanges, as they are perfectly shadowed by the front flanges. See Figure 2.15 for an illustration of this spatial temperature differential.

To avoid the costs associated with a fully cooled shroud—as well as the requirement of a piped feedthrough—but still achieve higher thermal gradients, a large cooled thermal mass was placed directly behind the structure during testing; its temperature was monitored in real-time by a thermocouple, simplifying experimental procedures

and allowing for precise modeling in simulations afterwards. The thermal mass used in this case was a 1/2" steel plate, cooled in a composites prepreg freezer to below -20°C; preliminary calculations showed that such a thickness would allow it to absorb the heat of the chamber lamp without changing temperature too rapidly. Indeed, during experiments, its high mass and specific heat made it warm very slowly in the evacuated chamber, as well as remain below freezing for over half an hour despite the lamp heating it along with the structure. Figure 2.10 shows the steel plate in situ, as well as the "frost lines" that formed on the steel after heating longer than normal tests. (Such preliminary trials used a hanging boundary condition for the structure, which was replaced by a clamped one in the current study.) These frost lines indicate the highly directional nature of the lamp flux, since sharp lines separate the region shielded by the structure, as well as the edge of the lamp beam itself.

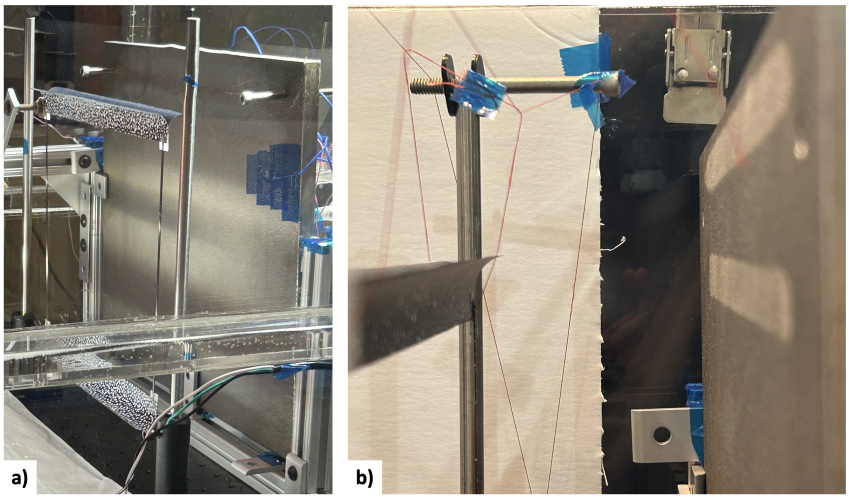

Figure 2.10: a) The cold plate during testing; thermocouple at right center under tape; b) lines of frost behind structure and outside lamp beam.

In addition, the chamber's aluminum baseplate (on which the entire apparatus rested) was cooled from beneath using a recirculating water chiller (Coherent, T255p solid-state) designed for laser cooling; the 10°C water cooled the baseplate to 14°C throughout testing.

Testing Procedure

All experimental trials adhered to the same sequence of events. For each sample's set of runs, the DIC rig was recalibrated before testing began. For each trial, the upper-left web of the sample was first rigidly clamped to the test fixture using PEEK

hardware; the chamber baseplate was then cooled to 14°C, taking approximately 1.5 hours. The LED lights required for DIC were switched on, and 300 DIC images were taken at a rate of 1 Hz as a displacement baseline. The cold plate was then taken from the <-20°C freezer and placed inside the chamber behind the sample, immediately followed by sealing the chamber and pulling a vacuum. After five minutes, when the pressure inside the chamber reached -95 kPa of vacuum (i.e. 95 kPa below ambient pressure), the IR lamp was switched on with a power of approximately 180 W for ten minutes; during this time, the DIC cameras continually took images at 1 Hz, and the IR camera manually recorded video and images every 135 seconds. The IR lamp was then powered off, and further DIC and IR images were taken for an additional five minutes as the structure cooled to room temperature.

Chamber pressures were maintained throughout the test by keeping the vacuum pump on for the full duration; the vacuum accordingly increased by roughly 0.5 kPa over the course of a five to ten-minute test. Three identical samples were tested under these conditions four times each, for a total of twelve nominal trials.

2.3 Experimental Results

Deflection Results

A typical DIC frame taken during the experiment, before and after post-processing, is shown in Figure 2.11 (red lines have been superimposed for visual clarity). Despite multiple manual calibrations of the cross-correlation algorithm to improve cross-camera matching, the large camera angles and large refraction correction meant that not all portions of the structure's flanges could be resolved in the displacement analysis. However, almost the entire top and bottom webs were resolved, meaning that the displacement of each longeron individually, as well as their twisting in relation to each other, could be precisely measured.

Lines were drawn across the longerons where the web and flanges met; these lines are superimposed in red in Figure 2.11 b). The out-of-plane deflections along these lines were then plotted for various critical timestamps: 1) just before the IR lamp turned on (the initial state before heating), 2) just before the lamp turned off (the fully heated state), and 3) just before the vacuum was released (the final state after cooling). Plots of these out-of-plane displacements, added to the undeformed structure's z-coordinates, are shown in Figure 2.12. (This addition explains why the "lamp on" initial state is not a flat line at $z = 0$ in both plots.)

Taking points on the right edge of the top and bottom longerons, we can visualize the

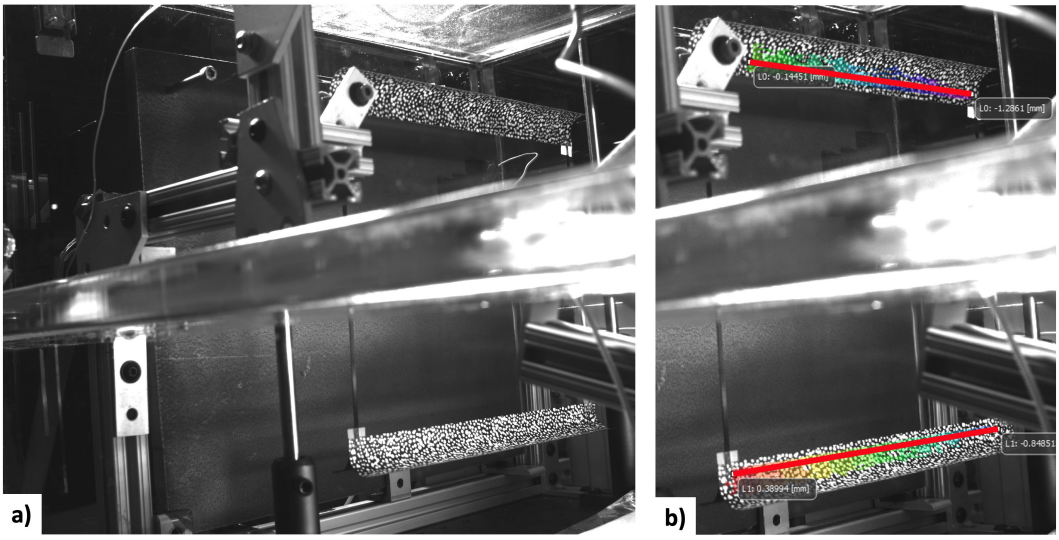

Figure 2.11: a) Left DIC camera view; b) after DIC cross-correlation with manual assistance (red analysis lines superimposed).

displacement over time of both with the plot in Figure 2.13. Table 2.2 summarizes these displacements for all trials, offering a comparison between them.

As shown in Table 2.2, the average deflections for the top and bottom longerons varied up to 27% between tests, with slightly less variation between samples. This variation can only partially be explained with the noise floor of the DIC measurements, which was found to be only 1-2 μm for most measurements and less than 5 μm anywhere on either flange for all trials.

Factors contributing to the repeatability of these experiments include the predictable nature of the clamped boundary condition used to hold the sample (chosen over other means of supporting the sample, such as hanging freely) as well as the controlled manufacturing process used to construct the constituent laminates and assemble the final structure. A main factor contributing to the deflection variation would therefore most likely be the variation in the temperature of the cold plate; depending on the exact circumstances of the freezer's opening history, the initial temperature of the plate would slightly vary, causing a difference in radiative boundary condition for the sample. (By contrast, the lamp-heating boundary condition was much more precisely controlled over all testing.)

Overall, the deflections of the top and bottom longerons did not exceed 2 mm, and were typically larger than 0.5 mm, making the scale of the deflections less than 1% of the structure's length of 250 mm. This small magnitude can be ascribed to

Table 2.2: Experimental rightmost-edge deflection results

Sample 1, trial	**12**	**14**	**15**	**16**	**average**
top deflection (mm)	1.38	1.83	1.65	1.66	**1.63**
bottom deflection (mm)	0.73	0.96	1.05	0.84	**0.90**
Sample 2, trial	**21**	**22**	**23**	**24**	**average**
top deflection (mm)	1.47	1.50	1.42	1.60	**1.50**
bottom deflection (mm)	0.84	0.82	0.86	0.92	**0.86**
Sample 3, trial	**31**	**32**	**33**	**34**	**average**
top deflection (mm)	1.39	1.37	1.45	1.19	**1.35**
bottom deflection (mm)	0.82	1.00	1.01	0.84	**0.92**

the relatively small thermal gradients able to be achieved in such an environment, even after the heating and cooling measures taken, as well as the short length of the structure increasing the stiffness of the longerons.

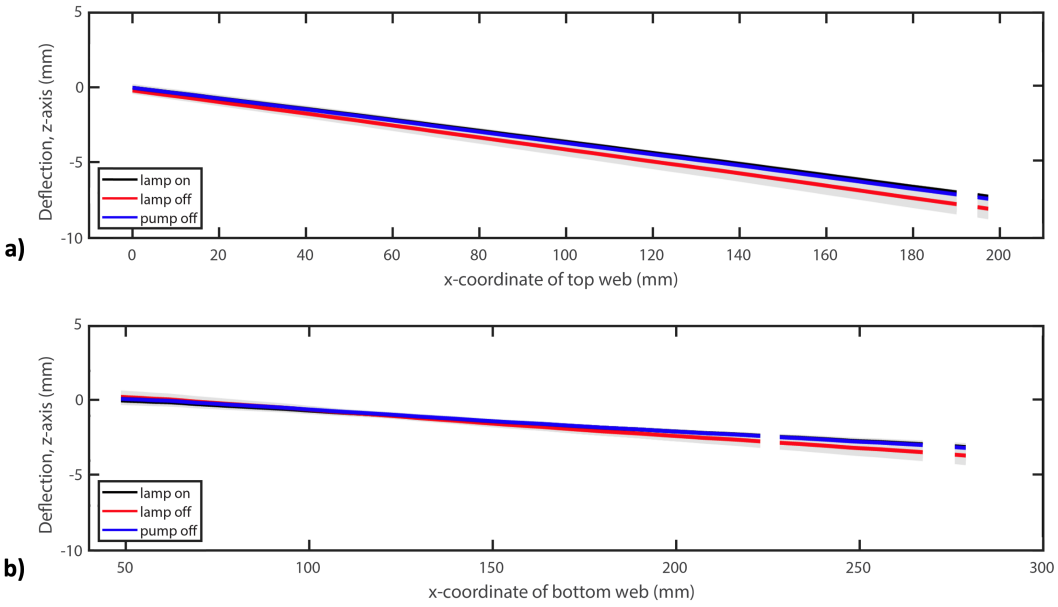

Figure 2.12: Displacement of a) top longeron and b) bottom longeron just before heating (black), just after heating (red), and just after cooling (blue).

In addition, the angle of the top and bottom longerons with respect to the plane normal to the heating direction (i.e. parallel to the back chamber wall and cold plate) can easily be calculated by taking the start and endpoint of the approximately flat flanges and taking the arc-tangent of their coordinates. In turn, these two angles, when subtracted, yield the "twist" of the structure as-manufactured (at $t = 0$) and as a function of time throughout the test. Such results are plotted for the third sample

as a function of time in Figure 2.13 b), while those of the first and second samples were similar.

Examining these results, we can see that the structure was negligibly rotated with respect to the incident lamp rays. In addition, the plots for the other two samples (not pictured) show that each sample has a non-negligible twist between 1° and 2° due to minor manufacturing defects.

As the experiment evolves, the main result is that the top and bottom flanges rotate with respect to their original configuration by around half a degree. The second is that the top and bottom flanges rotate together for the entire test, as evidenced by the negligible change in angle with respect to each other as the trial progresses (i.e. the green line remains constant). All samples behave in this manner, preserving the original rotation of each flange with respect to each other. This is an interesting result, as previous buckling studies of similar sample structures have emphasized the weakness of the structure in torsional deformations [23].

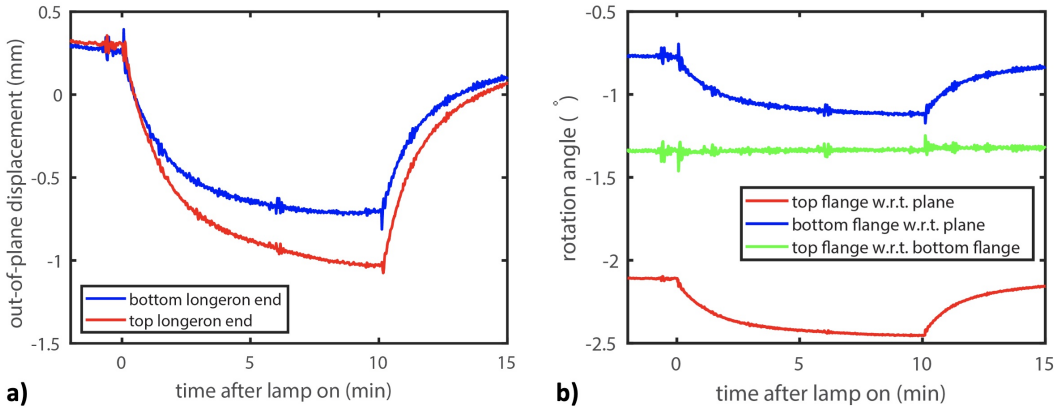

Figure 2.13: a) Displacement over time of center bottom longeron; b) rotation of top and bottom flanges over the same time period, and w.r.t each other.

Infrared Thermography Results

The IR camera images taken during each trial allowed an unprecedented glimpse into the development of thermal gradients on the radiatively heated structures in real-time. They offer many key insights into the temperature field, including how temperatures vary within a longeron flange, between the front and back flanges of a longeron, and how they correspond to the deflections induced by these thermal gradients.

General Temperature Trends

Figure 2.14 shows a sample image taken by the IR camera, with three superimposed "tooltip" temperatures: two at the approximate vertical and horizontal center of the top and bottom longeron, as well as one over the thermocouple monitoring the temperature of the cold plate.

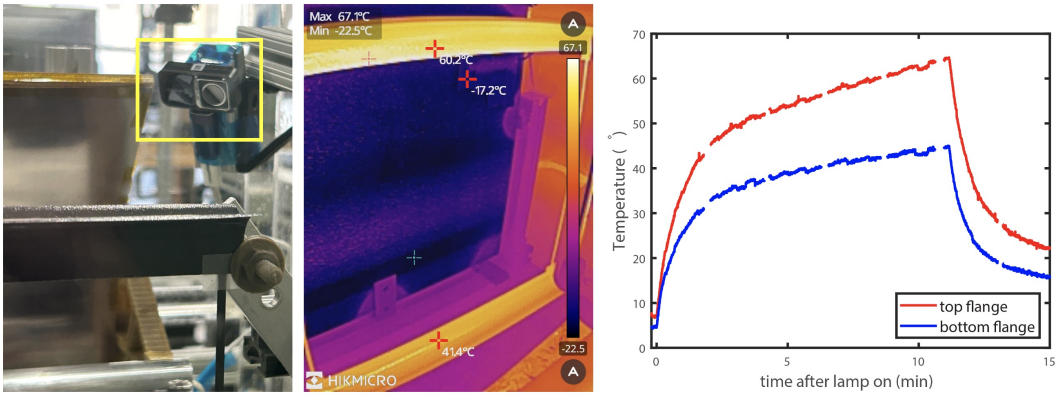

Figure 2.14: a) The IR camera mounted inside the chamber; b) IR image of peak trial temperatures, tooltip temperature readings at red crosses; c) two temperature readings over time.

As described earlier, these tooltip temperatures were compiled across video frames to produce temperature vs. time plots, also shown in Figure 2.14 c). Most prominently, the plot shows a difference in temperature between the two longerons that exceeds 20°C—despite the two being nominally heated symmetrically. Further experimental imaging showed that this primary difference was not caused by the DIC lights or asymmetric infrared reflections off the surface of each longeron; therefore, it can only be a result of nonuniform heating of the sample, both by the lamp reflector and residual convection within the chamber. Such a result informed how the companion COMSOL simulations dealt with both causes.

This temperature plot also reveals a quasi-bilinear transient behavior that differs from the usual asymptotic exponential behavior; a region of rapid temperature increase (roughly 2 minutes in duration) is followed by a region of slower, creeping increase (roughly 8 minutes in duration). The same two-phase behavior also characterized the deflections observed in every trial, as deflections rapidly sprang to near their final values within two minutes, then slowly creeped upward the rest of the way. Since the temperatures on the structure are coupled to those of the surrounding chamber via radiation and residual convection, such behavior can be explained by the large

difference in thermal mass between the sample and the surrounding chamber: in the first phase, the structure heats up rapidly due to its low thermal mass while the rest of the chamber remains nearly unaffected, and in the second phase, the latter slowly heats, making the structure slowly increase in temperature as well.

Finally, the slight difference in temperature between the top and bottom flange before the lamp turns on at $t = 0$ was confirmed to be a result of slightly uneven heating by the DIC lights; it is almost impossible to evenly illuminate the sample to prevent this, but this secondary cause of longeron temperature difference was an order of magnitude less than the previously mentioned effect of the IR lamp.

Intra- and Inter-flange Temperature Deltas

The software Hikmicro Analyzer was used to analyze the still images, spaced every 2.25 minutes, for the maximum minus minimum temperatures (i.e. temperature deltas) present across and between flanges. A resulting post-processed image and compilation of deltas is shown in Figure 2.15. Temperature deltas were measured over line segments drawn over the top web, bottom web, top flange, and bottom flange, with the web deltas not plotted.

For all three samples, temperature deltas over the top and bottom flanges, as well as between the front and back flanges of the top longeron, closely tracked the temporal evolution of the displacements; matching Figure 2.13, the deltas monotonically increased as the displacements did. The web gradients did not do so; however, this is in agreement with previous simulations of large SSPD-style structures, which predicted displacements with no web gradients at all due to perfectly symmetric heating [37]. Thus, direct measurements of the thermal gradients responsible for structural deflections were confirmed to vary monotonically together as expected.

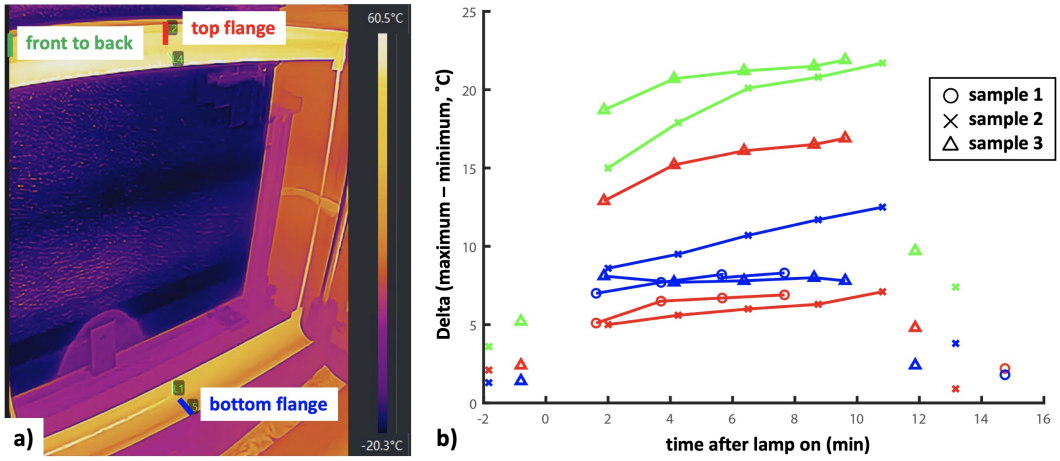

Figure 2.15: a) IR image with red, green, and blue line selections; b) temperature deltas along those selections for all samples.

Chapter 3

THERMOELASTIC SIMULATIONS OF MODULE-SCALE EXPERIMENTAL RESULTS

"Philosophy is like trying to open a safe with a combination lock: each little adjustment of the dials seems to achieve nothing, only when everything is in place does the door open."

Ludwig Wittgenstein, philosopher
and aerospace engineer

After establishing a baseline of repeatable experimental results under controlled conditions, the next step is to accurately predict these results using a high-fidelity multiphysics simulation. The entire chamber, apparatus, and sample were modeled in COMSOL Multiphysics, and a transient simulation of the first two minutes of a test—a shortened timeframe that captures the vast majority of the experimental observations—was performed, yielding predictions of temperatures and deflections across the entire structure.

Any simulation studying thermally induced deflections, due to the causational and sequential relationship between temperature and deflection, must answer two fundamental and consecutive questions:

1) Given a radiative heating environment, what temperatures evolve on the structure?

2) Given a temperature field on the structure, what deflections are induced?

If the first question cannot be sufficiently answered, deflections cannot be accurately predicted; in this case, the temperature field must be determined through experimental means, as detailed in the final section.

Fundamental to this simulation approach is capturing as many physical effects as possible in the numerical model, e.g. heat transfer, shell solid mechanics, and convection; each additional factor, however, increases the computational cost of the model. Indeed, adding convection to the 3D model turned out to be prohibitively computationally expensive. When 2D simulations of our geometry revealed a non-negligible convective cooling effect—one that could not be adequately modeled by

natural convection correlations—it necessitated the creation of two models of the experimental setup, one in 3D and one in 2D.

The 3D COMSOL model allowed a direct digital-twin-like matching of specific experimental runs to virtual runs simulated with the same parameters; it modeled the effects of thin-shell solid mechanics, heat transfer in solids and shells, and radiative heat transfer all simulated simultaneously (coupled as appropriate) to predict temperatures and deflections on the structure in a simulation as close to the original setup as possible.

The 2D COMSOL model, neglecting any deflection analysis, was designed to give insight into the temperature effects of residual convection in the 4-5% atmosphere environment; while modeling conduction as usual and radiative heat transfer with ray tracing, convective heat transfer was explicitly modeled using a full fluid-flow simulation.

As will be shown, only a combination of the effects captured by both models is able to match the experimental data accurately; this meant that neither of these models was able to predict structural deflections to the accuracy originally sought after. However, it is worth noting that the causes of the uncertainties (unpredictable convection and lamp reflector imperfection) do not exist in the space environment intended for the structures in question.

Therefore, a third model was introduced to predict structural deflections *given* the experimentally measured temperature field; infrared measurements were applied to an Abaqus model, and the resulting deflections were obtained from the subsequent Abaqus simulation. The space thermal environment lacks convection and is more easily predicted, making the concept of a precisely known temperature field but an unknown deflection field on a new structure completely plausible; thus, this last approach is able to lend credibility to all future simulations for which laboratory verification testing is impossible.

3.1 3D Chamber Simulation

Simulation Setup

To model the structural deflection response of the structure, the unit structure's geometry was reproduced in COMSOL, including the 1.3° twist present in the manufactured sample. As all parts of the structure are thin shells, shell elements and the corresponding thin-shell solid mechanics were used to model the deflection response; solid elements were only used to model the chamber baseplate and

cold plate. The Layered Materials portion of the Composite Materials Module was employed to accurately simulate the laminates present in the structure, since the structural behavior of the laminates is too complicated to be captured by an "equivalent" homogenized material model. As the mechanical properties of the constituent laminae have been previously characterized [20], their individual material properties enter into the model via this route. The exact mechanical properties used for the analysis are given in Table 2.1.

The absorption and transfer of heat through the structure was modeled using the Heat Transfer in Shells module; orthotropic heat conduction in the structural laminates is therefore able to be accurately captured by the model. While this module is capable of modeling conductive heat transfer individually through the various layers of composites, the thermal property data for our laminates was only ever characterized at the scale of the laminate, since such properties were measured via testing performed on coupons of the flange. Therefore, both materials were simply given the same laminate thermal properties, listed in Table 2.1, effectively modeling the laminate as an equivalent thermally-homogenized orthotropic material.

The thermal expansion resulting from the structure's temperature field was captured using the Solid Mechanics of Shells module's Thermal Expansion component, added under the Layered Linear Elastic material definition. This definition allowed for the modeling of the orthotropic thermal expansion of the laminates, using material properties measured from sample coupons.

Thermal Environment and Lamp Reflector

To model the radiative heat transfer and view factors among the lamp light, walls of the chamber, baseplate, structure, and frozen plate, the External Radiation Source of the Surface-to-Surface Radiation module was used. The same module also handles the reflected infrared lamp light, as described below.

To simulate the heating caused by the lamp reflector, as well as accurately capture edge effects and finite lamp size, the lamp bulb was modeled as a set of n evenly-spaced point sources at the focus of both reflectors, with each point source radiating $1/n$th of the total lamp power. Iterative simulation revealed $n = 15$ to be a large enough set of points to effectively distribute the heating along the length of the virtual lamp bulb.

The temperatures of the frozen plate, chamber walls, and baseplate were imported from experimental thermocouple measurements, enabling them to change as a func-

tion of time during the transient simulation to match experimental data.

Thermal Properties

While the structural properties of the laminae and laminate used to build the structure have been previously characterized [20] and tabulated in Table 2.1, the thermal properties needed had to be measured from coupons of the laminate; these included the specific heat, coefficient of thermal expansion, absorptivity/emissivity, and thermal conductivity. The first three properties were obtained from testing performed at the Jet Propulsion Laboratory and TA Instruments; the orthotropic thermal conductivity (along/across the carbon fiber direction) was both measured indirectly and calculated from simulation, as described in Appendix A.

3.2 2D Convection Model

Previously, the effect of convective cooling on structural temperatures was assumed to be small based on natural convection correlations [6][53]; however, the thinness of the structure, the enclosed nature of the chamber, and the presence of a hot lamp bulb and cold plate all stretch the assumptions inherent in a heated plate correlation. A full fluid flow analysis is a much more accurate method of modeling convection, but comes at a steep computational cost for 3D geometries; the long simulation time for the 3D transient model described above (12.5 hours) precluded the addition of any convective effects beyond natural convection correlations; in addition, the latter were shown to poorly match temperatures generated by the 2D fluid flow analysis regardless.

Thus, the chamber, apparatus, and structure were modeled in 2D by taking a vertical cross-section through the structure's center, parallel to the lamp beam. Note that only the structure's longerons were modeled; the battens, in addition to only being present at the structure's ends, provide so little thermal conduction as to be safely ignored.

The Heat Transfer in Solids and Fluids and Laminar Flow modules were used to model heat transfer and fluid flow in the chamber atmosphere, respectively; the Heat Transfer in Shells module modeled conduction in the structure; the Surface-to-Surface Radiation module modeled the lamp bulb (a point source in 2D) and double reflector, as well as the radiative heat exchange among the reflector, frozen plate, chamber walls, and structure.

Structural temperatures derived from vertical and tilted plate natural convection

correlations [6] were also calculated as a comparison, but were shown to be much too aggressive in their cooling predictions from both experiment and fluid flow simulation; they are therefore not presented here.

3.3 Simulation Results

3D Model

The last frame of the 3D simulation, at 120 seconds, is shown in Figure 3.1; temperatures are shown at left, and deflections at right.

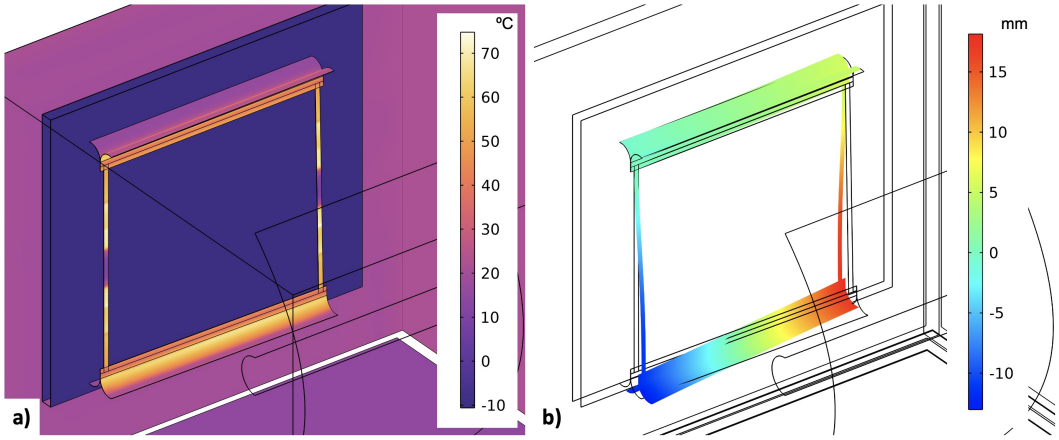

Figure 3.1: The 3D COMSOL simulation of the experimental apparatus and chamber in COMSOL; a) transient results for temperatures (°C) and b) deflections (mm) after 120 seconds.

A fuller comparison of several points across the experimental data, 3D simulation, and 2D simulation is presented in Section 3.3, but the key points are noted here. The most obvious metric is the maximum temperature reached on the top longeron's front flange; at 65.3°C, there is over a 15°C difference between the 3D simulation data and the experimental data 120 seconds into a trial. Other metrics (temperatures at the center of the top web, bottom web, and flanges) are more favorable, but this 3D simulation tends to over-predict temperatures on the top flange by 5-10°C, while under-predicting temperatures on the bottom flange by the same amount. Since the IR camera data was determined to be unaffected by reflections and/or DIC lighting to this degree, these discrepancies strongly point to the model not adequately capturing the experimental heating. As we will see, this uneven heat flux can almost completely be explained by convective heating via residual air remaining in the chamber, as well as by lamp bulb–reflector misalignment causing the lamp lighting to be non-uniform.

Deflections of the structure are also over-predicted, albeit to a much higher de-

gree; maximum deflections on the top and bottom flange are 5.8 mm and 17.7 mm respectively, which are 3 to 19 times greater than the experimental results discussed in Section 2.3. This is consistent with the temperature predictions, since an over-prediction in temperatures and gradients should cause an over-prediction in deflections—and evidently much more so, since the latter is nonlinearly caused by the former (e.g. due to structural geometry).

2D Model

The temperature discrepancies revealed in the 3D model motivated the creation and simulation of the 2D model. A snapshot of the laminar convection flow predicted by the simulation is shown in Figure 3.2 at left, while the resulting temperature field is shown at right.

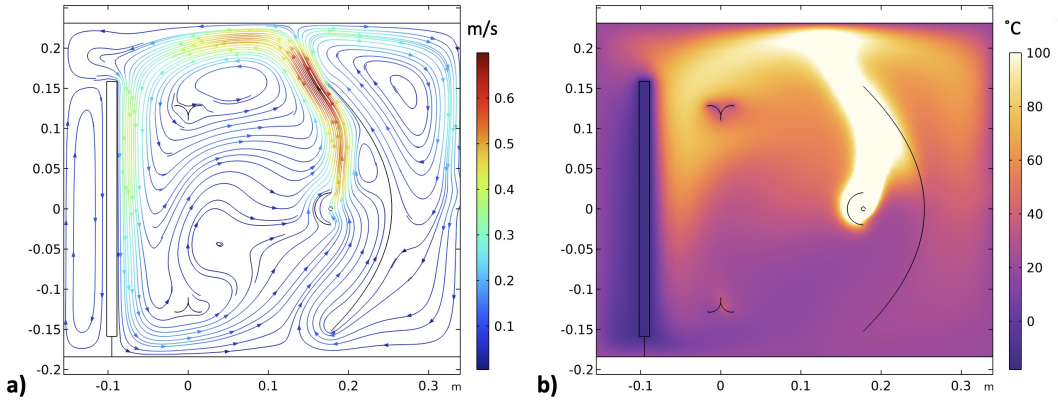

Figure 3.2: The 2D COMSOL model of the experimental apparatus and chamber, showing a) convection field generated in 4-5% atmosphere, and b) temperatures (°C) reached after 120 seconds.

The two most glaring features of the simulation are 1) the strong thermal plume rising from the lamp bulb, and 2) the downward cold current created by the frozen plate directly behind the structure. The two effects combine to create a non-negligible convection cell that cools the top and bottom flange unevenly; such a temperature effect is shown in Figure 3.3, where the temperatures across the top and bottom longerons are plotted. There is now only a 4°C difference in the maximum temperatures on each longeron, and the temperatures at various measured points agree much more closely; any compared point on the simulated structure temperatures and experimental data differs by less than 5°C.

To determine whether this remaining discrepancy could be accounted for by non-uniform lamp heating, further simulations were run with the point source represent-

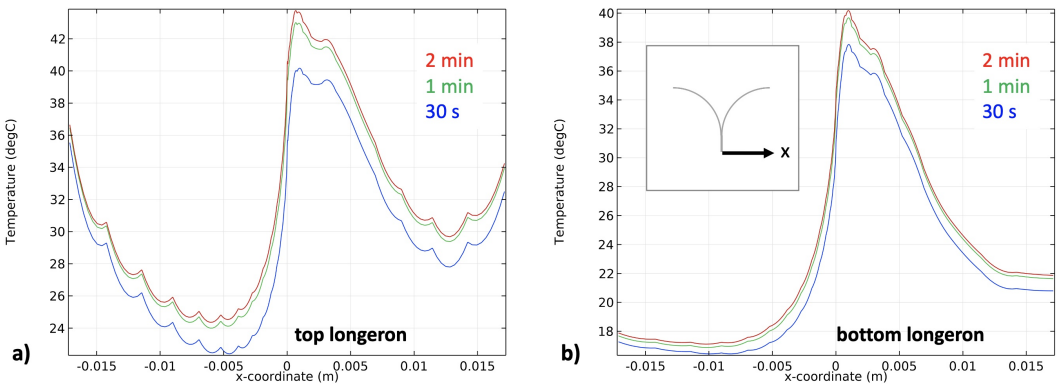

Figure 3.3: Flange temperatures of the 2D simulation across a) top longeron and b) bottom longeron after 120 seconds.

ing the lamp slightly offset from the focus of the reflector, both in the horizontal and vertical directions; this simulated a lamp bulb alignment issue that would have been difficult to see in the actual experiment, since only a few millimeters of misalignment were necessary to produce noticeably different temperature results. A misalignment of four millimeters, for example, comes within less than two degrees of the experimentally observed maximum flange temperature and center bottom flange temperature.

From this 2D simulation then, the combined effect of residual convection and lamp bulb misalignment has been shown to be sufficient to explain the observed discrepancies between simulated and experimental temperatures.

Comparisons to Experimental Results

A table summarizing the temperatures obtained from all the COMSOL models at several key locations on the structure, compared with experimental data, is shown in Table 3.1. While no one simulation is able to perfectly predict the experimental temperatures, a combination of factors (residual convection, lamp bulb misalignment) would lie within the uncertainty of the models' predictive ability.

It was discovered that mesh refinement on the 2D study actually *decreased* the temperature estimates even further, showing that the convective effects in question heavily depend on the scales of the fluid flow. When combined with the complications of the actual experimental setup (i.e. the flow moving around all parts of the experimental rig), the 2D temperatures can really only be compared to reality with a large "error" bar, to the tune of 10-20°C.

Table 3.1: Key structural temperatures across experiment and COMSOL models; compare bolded simulation results to experiment.

Location (°)	Experiment	COMSOL 3D
maximum flange temp.	**48**	65.3
top web	**42-43**	41-52
bottom web	**28-30**	39-52
top flange tip	**38**	24
bottom flange tip	**20**	25
	COMSOL 2D (no lamp offset)	**COMSOL 2D (4 mm lamp offset)**
maximum flange temp.	44*	**46***
top web	**41***	47-49*
bottom web	34.5*	**31-32***
top flange tip	**34***	28-32*
bottom flange tip	**22***	**20***

*value varies by ±10°C depending on mesh size

3.4 Deflection Simulation Using Infrared Measurements

Two main concerns arise with the non-negligible and difficult-to-account-for effects of convection in the thermal analysis—the first being that the model's accuracy is heavily confounded by a factor (convection) totally absent from the actual space environment it seeks to eventually model.

The second is that, with heating loads and boundary conditions not translating into accurate temperatures, the rest of the thermal deflection "chain of causation" (i.e. temperatures becoming thermal strains becoming deflections) is unable to be evaluated for accuracy. To fully characterize and verify the model, determining how well it predicts deflections given a known temperature field is necessary.

Leveraging our unique experimental data gives us precisely this ability: by directly measuring the temperature fields present on the unit structure during the experiment, applying them to the structural model, and comparing the predicted deflections with the measured experimental deflections, we can isolate how well the model predicts structural deflections from a given temperature field. See Figure 3.4 for a schematic of how experimental thermal measurements enter into the thermal deflection "chain". The details of this approach follow.

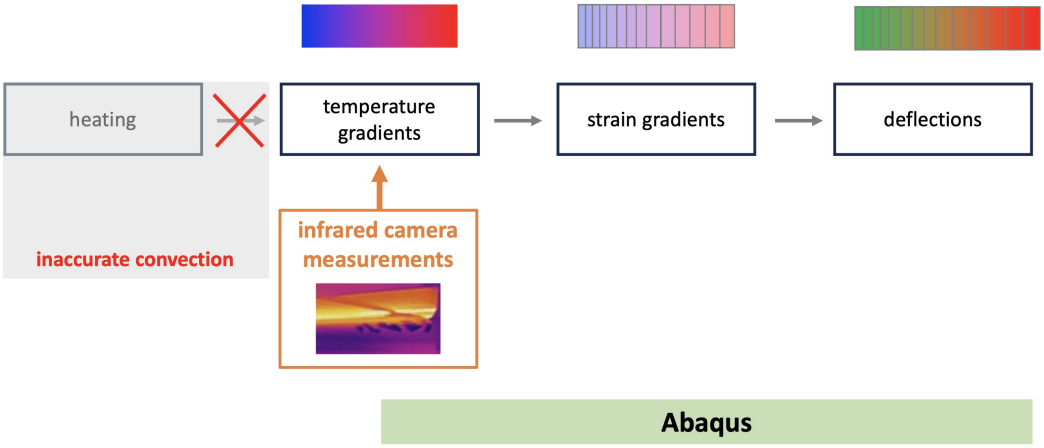

Figure 3.4: Schematic of how infrared temperature measurement replaces the "heating" portion of the thermal deflection causation chain.

Methodology

For an accurately-predicted full deflection field, it is necessary to have a corresponding full temperature field. Luckily, the unit structures tested in this work are thin enough to lack through-thickness temperature gradients[1], meaning that the temperature measured from any side accurately captures the temperature of any particular "element" (ignoring any confounding effects of specular light reflections). However, since the longeron geometry partially overlaps itself—i.e. it is impossible for one camera angle to capture all elements of a longeron's front flange, back flange, and web simultaneously—multiple infrared cameras are required to capture the full temperature field of a structure at a moment in time during a trial.

Rather than incurring the expense and logistical complexity of coordinating multiple infrared cameras, this work used a more practical approach; by aiming the infrared camera at the bottom longeron during one trial, at the top longeron during a second, and at the entire front of the structure during a third, while ensuring that the temperatures and deflections between the three trials were almost identical, a nearly full temperature field could be compiled using a single camera. See Figure 3.5 for top, bottom, and front infrared camera views from such a set of compatible trials.

Two such sets of trials were successfully conducted, offering valuable insight into the

[1]This assumption was verified for our thin composite laminates both theoretically and experimentally; a back-of-the-envelope calculation showed that the thickest (web) laminate would have at most a 0.7ºC temperature difference between front and back faces under lamp heating, while infrared imaging of laser heating similar to that described in Appendix A showed identical temperature responses on both faces.

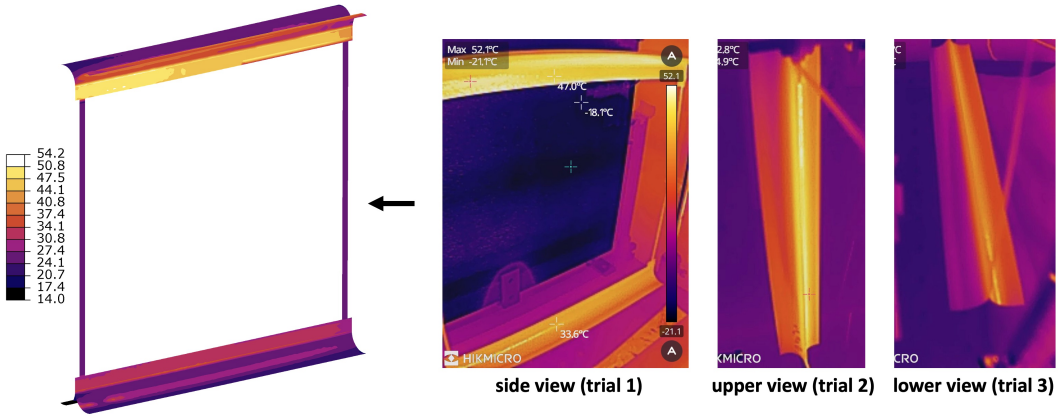

Figure 3.5: The Abaqus model incorporating the temperature fields measured by the infrared views of the front of the structure, top longeron, and bottom longeron.

model's predictive capability under different temperature and structural conditions.

For more rapid comparison with previous transient simulations, thermal camera images were captured at exactly two minutes after the heat lamp was turned on during each trial.

Mapping

Applying temperature fields to a structural deflection model is more easily accomplished in Abaqus (Simulia, Dassault Systèmes) rather than COMSOL, and was chosen from familiarity; further details of similar temperature field importing can be found in Chapter 5. However, the creation of the software "pipeline" necessary to convert infrared camera image data into such temperature fields was nontrivial, and is documented here. Snapshots of the various "pipeline" stages are shown in Figure 3.6.

Thermal camera image data is by definition planar and taken from a perspective, so the first step is to warp and crop the image into a rectilinear form readily projected onto the known unit structure geometry. The infrared camera has a slight fisheye distortion. Since the optical resolution was insufficient for normal MATLAB fisheye-removal algorithms to function properly, care was taken to put as much longeron as possible in the less-distorted center of the frame: a simpler six-point affine transformation was then used to warp the image into an approximation of how the longeron would appear from above/below. This warping worked for the top and bottom longeron temperature fields.

However, un-warping the more distorted front camera view proved more challeng-

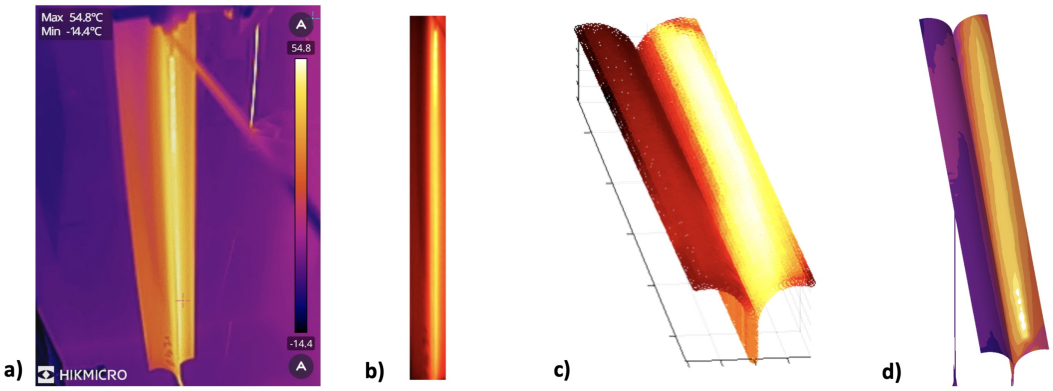

Figure 3.6: Stages of the infrared measurement to model "pipeline": a) original infrared camera data, b) after perspective-warping and cropping, c) interpolated onto nodes of Abaqus mesh, and d) applied to Abaqus model as a predefined temperature field. Color maps vary slightly between programs.

ing, as the top and bottom webs are unavoidably affected by the camera fisheye. Standard MATLAB algorithms proved unable to remove this fisheye due to the camera's limited pixel resolution of calibration targets; in addition, manual polynomial perspective warping also failed to remove the curvature. The final technique involved fitting a fourth-order polynomial to the visible inner edge of the webs, and translating it a fixed distance upward to section off the curved "quadrilateral" shape of the webs; this was then sectioned into 16 approximate rhomboid shapes. A mesh of the undeformed web was created and sectioned into 16 equal rectangles; the temperature at each point of each rectangle of this web mesh was then set to the temperature value of the corresponding point in the corresponding rhomboid of the curved web data. Sectioning off the web into rhomboids allowed for a locally linear approximation, meaning that only shearing and rotating were required to match the data locally with the undeformed mesh. See Figure 3.7 for an illustration.

After cropping out any background data, a MATLAB script was used to interpolate the infrared data onto the nodes of an Abaqus model of the structure; this model was carefully constructed to have the same longeron twisting as the actual structure tested.

With each node having been assigned a corresponding temperature, a text file recording these pairs was then exported for use by the *TEMPERATURE keyword in an Abaqus input file; a file of each node at room temperature was also exported for use as an initial condition by the same. A Static, General simulation was then performed, using the material properties of the laminate as specified in Table 2.1.

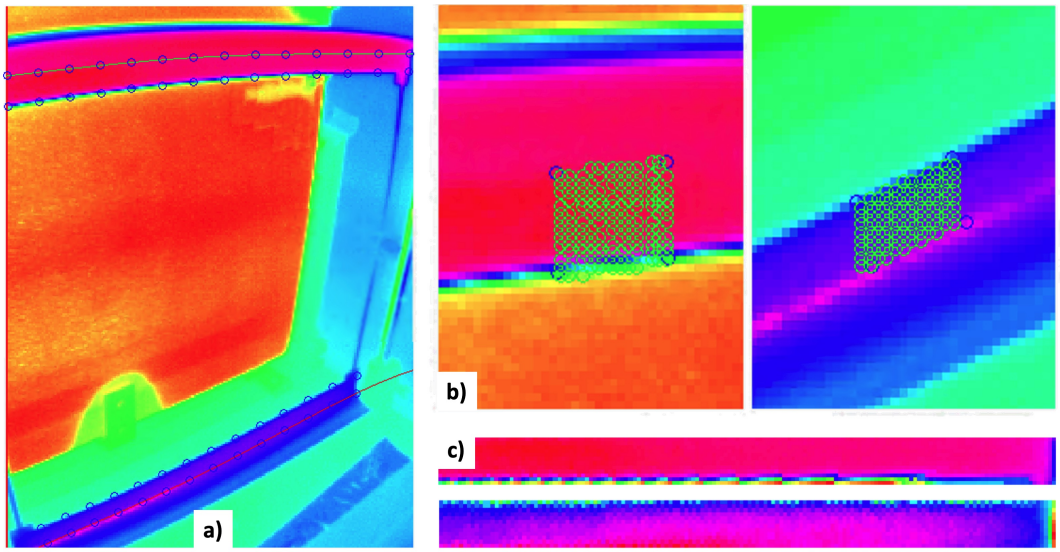

Figure 3.7: Removing fisheye distortion from longeron web temperature data: a) original infrared camera data, with superimposed web edge curve fits and mesh grid points; b) projection of undeformed mesh points onto a rhomboidal section of the top and bottom web, showing the corresponding interrogated data points; c) final undeformed temperature mesh of top and bottom webs.

Deflection Results

Two sets of deflection results were obtained, corresponding to the two pairs of compatible trials described above. These are shown in Figure 3.8; the difference in deflection magnitude is due to differing temperature fields, with the first pair of compatible trials having lower temperature gradients on average. For these two sets, the web temperature data was not collected, and therefore was not used for these results.

The first set of results overpredicts the deflections measured two minutes into its trials by a factor of 4-5; the second set overpredicts its trials by a factor of 3-4. While not perfect, these results represent an improvement over previous deflection estimates from multiphysics models, and consistently predict the correct direction of deflections on both top and bottom. (This directionality was something shown to be nontrivial in previous simulation work [38].)

While the temperatures do vary slightly between the two sets of trials, the main difference between the two is the rotation of the structure by 180°. The sample structure was geometrically symmetric, and possessed visually identical twist (1.3°) in either orientation, so such a rotation shouldn't have affected the measured deflections; however, the rotation changed the measured deflections by almost a factor of two.

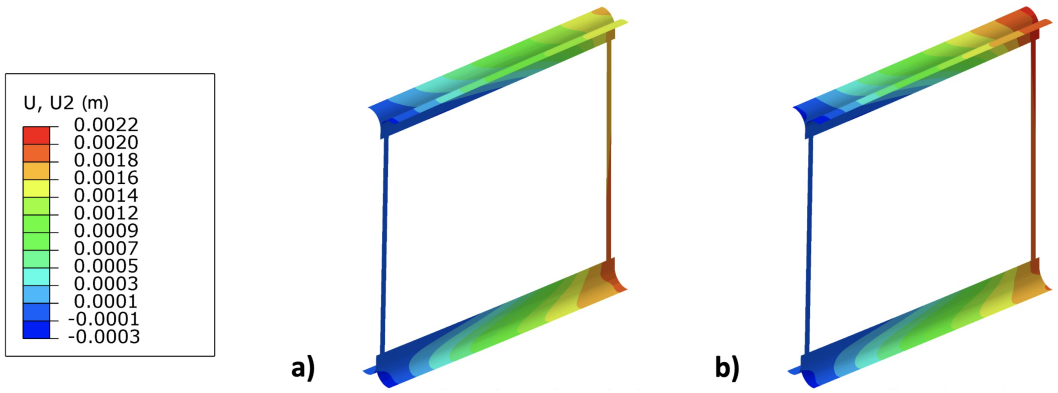

Figure 3.8: Predicted out-of-plane deflection fields for a) the first pair of compatible trials (lower temperature) and b) the second set of compatible trials (higher temperature).

Taken together, these results suggests not only an uncertainty in structural/geometric temperature response, but potentially an uncertainty in laminate response as well, since that is the only way to explain such a discrepancy with a nominally and visually identical symmetry in structural geometry.

Adding Web Temperatures

When web temperatures were added to the second trial above, estimates of deflections significantly worsened (8-10x experimental data) due to the presence of high temperature gradients between the web and the flange; these gradients were the result of incomplete thermal camera data, as well as the mapping algorithm assigning cooler flange temperatures too far down due to the camera perspective; see Figure 3.5. Better camera angles would of course ameliorate this issue.

However, the insight into how large thermal gradients at the web-flange interface cause much larger deflections is valuable. In the previous set of results that did not include web temperature data, the temperature-mapping algorithm simply smeared the flange temperatures onto the web, causing much smaller thermal gradients in the web-flange interface region and thus improving the deflection estimates, even with temperature data that was much colder than reality.

3.5 Conclusions

The 3D COMSOL model of the chamber was able to reproduce experimental results only qualitatively; the 2D COMSOL model was able to reproduce experimental temperature fields quantitatively, within the convective margin of error; the Abaqus

model was able to predict structural deflections more accurately than either of the previous two. This means that, when combined, the COMSOL models used were able to accurately account for all major physics of the problem in question.

Even more importantly, however, the strengths of these models (and later versions of them) directly led to improvements on the prototype unit structure described in Chapter 4, and their weaknesses informed the coupled simulation mechanics of Chapter 5, thereby demonstrating the models' utility.

Chapter 4

EXPERIMENTS ON THERMALLY CONDUCTIVE LAMINATES AND STRUCTURES

"Diamond, for all its great beauty, is not nearly as interesting as the hexagonal plane of graphite."

Richard Smalley, discoverer of buckminsterfullerene

Much has been learned from the multiphysics simulations performed in the preceding chapters, but two points especially show an interesting way forward toward desirable structural properties—namely, the property of higher laminate thermal conductivity.

First, previous parametric studies on various structural lengths performed in COMSOL indicated that higher values of k_2, or the thermal conductivity of the laminate transverse to the carbon fibers, noticeably reduced structural deflections when increased at least two orders of magnitude, with further reductions possible at even higher conductivities [38].

Second, during the slew simulations recounted in Section 5.3, it will be shown that for structural lengths of two meters (and presumably higher), the existing carbon-fiber laminate layup would buckle at an incident sun (α) angle of 45°—see Figure 5.29; this instability caused a visible buckle to form in the longeron flange, causing linear quasi-static analyses to not converge and nonlinear analyses to report negative eigenvalues. Proceeding with the slew simulations required a material definition swap to a higher conductivity material, the subject of this chapter.

Both points suggest that significant increases in thermal conductivity would reduce structural temperatures and gradients, and therefore reduce buckling and excessive deflections. The question, though, is how to do so given the razor-thin mass margins (and materials) used for deployable structures destined for space solar power applications.

The answer presented here lies in a historic material in a modern form: graphite, in the form of an ultrathin graphitized polymer film. The incredible heat conduction

capabilities of many carbon allotropes are shared by thin graphite layers, meaning that such a layer would drastically increase the conductivity of any laminate incorporating it. Such layers have been used previously for thermal reasons in deployable antennae, as discussed below.

Therefore, a composite laminate incorporating a graphite layer was constructed and characterized; this being successful, a duplicate structure of the type used in the experiment of Chapter 2 was constructed and tested in the same manner. The graphite film selected for this purpose, manufactured by HPMS Graphite, was 12 μm in thickness; its thermal conductivity, 1800 W/m^2, was nearly four orders of magnitude higher than the composite laminates used in the experiments of Chapter 2 [13]. A comparison of experimental results between previous composite laminates and graphite-composite laminates was thus obtained, showing a dramatic reduction in deflections and therefore the promising role such additions could have in future space structures.

In this chapter, results of preliminary COMSOL simulations are first shown and discussed, illustrating both the promising nature of incorporating graphite layers and where best to put them given our structural geometry. Next, the method of incorporating the graphite into our composite laminates is described for both a coupon of material and a full structural module. A partial characterization of thermal properties follows, showing the laminates demonstrable ability to spread radiative heat energy. Finally, the graphite-laminate structure is experimentally tested and analyzed, providing empirical evidence that such thermal control measures are highly effective in composite space structures.

4.1 Background and Prior Use

While graphite layers are commonly used in consumer electronics as heat-spreading components, their lightweight nature and preservation of thermal conduction at minuscule thicknesses makes them an attractive component for space structures. Indeed, such a thermal solution was deployed to great effect by a team of researchers at the Tokyo Institute of Technology, who constructed a 64×64 element Ka-band active phased array antenna from woven carbon-fiber and graphite sheet laminates [28]. Despite the constituent circuit boards generating a total of 256 W of heat, the inclusion of two layers of 130-μm graphite sheet was enough to dramatically reduce surface antennae temperatures; the finite-element model of the worst-hot case in orbit dropped from a peak temperature of 184° to 86° on the hottest component surfaces

[28], while further thermal tests showed similar heat reductions [44]. Another group of researchers was similarly able to achieve excellent thermal control on a micro satellite by implementing a flexible radiator fin using 35-μm graphite film [34]; a third team was able to use similar graphite-film-covered radiator fins with hinges to vary radiator efficiency by 35% [32].

Despite the bending ability of such thin graphite sheets, one potential concern is their potential to form micro-cracks under repeated localized folding, as shown by experimental testing by the same team; however, a backing layer of 50-μm polyimide tape on the crease lines was sufficient to significantly reduce this effect [44]. This means that bonding the graphite sheet to a flexible support would eliminate concerns of decreased thermal conductivity due to micro-cracking. In addition, the bending radii involved in such folding tests were much smaller than any use case relevant to the structures described in this thesis.

Competing Solutions

Other similar thin carbon-based layers exist that could potentially be used in space structures, such as chemical-vapor-deposited diamond layers [22] and carbon nanotube (CNT) paper [30]. However, CVD diamond films, while having the same thermal conductivity as graphite, are much more prone to fracture when bending, making them practical only for rigid structures of tightly-controlled surface tolerances [22]. CNT paper, while of similar thinness and fragility to unsupported graphite film, only possesses a thermal conductivity on the order of 1-10 W/m•K, and therefore has a higher cost/benefit ratio [17].

As an aside, non-carbon thermal coatings (e.g. paints) or surface finishes can also be used to achieve heat reduction on space structures, and have a long historical legacy [12]. However, such coatings merely reduce the amount of solar heating for surfaces, and therefore only indirectly affect temperature gradients; in addition, the apparatus required to deposit ultrathin layers of paint (appropriate for our 80-μm-thick laminate flanges) was prohibitively unavailable. In addition, the proposed use case for our structures—solar power satellites deliberately exposed to the sun at almost all times—would degrade many legacy coatings with bombardment by UV radiation, charged particles (especially in MEO and GEO), and to a lesser extent atomic oxygen [15] [33].

Based on these considerations, graphite sheet was chosen as the material most likely to successfully incorporate into our current composite laminates and exhibit desired

thermal properties.

4.2 Coupon Fabrication and Laser-Heating Verification

To verify the feasibility of incorporating graphite sheet into our existing laminates, a coupon of graphitized-polymer-composite laminate was manufactured using a technique similar to the construction of the flange laminates discussed in Chapter 2; the stacking sequence, shown in Figure 4.1 was [±45 GFPW / 0 UDCF/ ±45 GFPW / GRST], where GFPW is 25 μm plain-weave glass fiber prepreg, UDCF is 30 μm unidirectional carbon fiber, and GRST is 12-μm graphitized polymer film.

The graphitized polymer film is mostly flakeable graphite, and therefore needs a bonding layer to make it adhere to the composite substrate; the previous publications mentioned used a 20-μm adhesive layer as an interface [44]. However, our composite layup is constructed of prepregs which bleed resin during the curing process; therefore, simply placing the graphite sheet as the first or last layer in the laminate allows a portion of the bleed resin to strongly adhere the graphite layer.

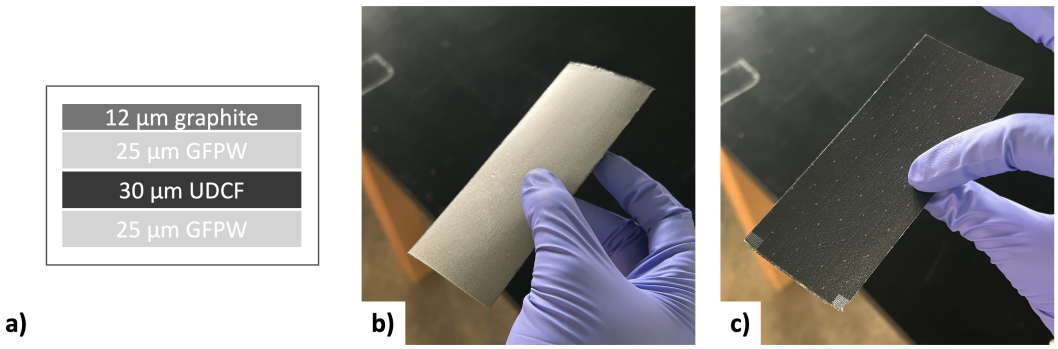

Figure 4.1: a) Layup diagram of composite laminate with graphite layer. Manufactured test coupon, b) front and c) back.

To verify the increased thermal conductivity of this laminate, a simple laser heating experiment was performed. The graphitized-polymer-composite sample, as well as a control sample of ordinary composite laminate, were heated with a laser dot for several seconds until approximate thermal equilibrium was reached; a thermal camera observed the transient temperature rise at the center. The diagram of the setup and results are shown in Figure 4.2; note that both samples were mounted behind a 20-mm square paper window for camera calibration.

The difference in thermal response between the two laminates—which differ by only a single layer of 12-μm graphite—is dramatic. In Figure 4.2 b), while a visible hotspot appears on the original sample, only a small temperature rise over the entire

square of visible graphite makes the heating visible at all. But Figure c) 4.2 shows the largest difference: instead of an 18° temperature rise over room temperature, the graphite laminate rises only 0.1°—a full two orders of magnitude less. This behavior is the result of the graphite sample spreading the heat so quickly over the surface of the sample, and so efficiently to the surrounding air, that the temperature rise is almost invisible.

This promising result demonstrated that a graphitized-polymer-composite laminate could be both successfully constructed and effectively dissipate incident thermal radiation, paving the way for further analysis of structural inclusion.

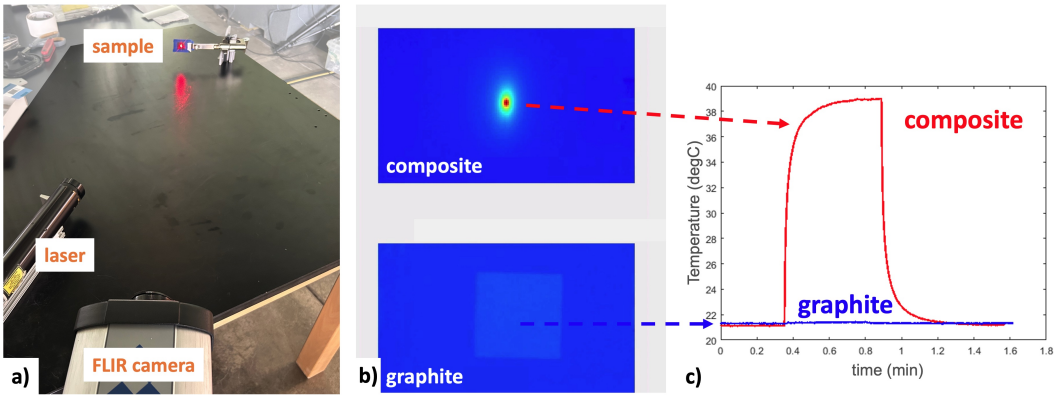

Figure 4.2: a) The experimental rig used to heat graphitized-polymer-composite and control samples. b) IR camera image at approximate steady-state after several seconds of heating. c) Comparison of ordinary composite vs graphitized-polymer-composite temperatures.

4.3 COMSOL Simulations of Graphite-Composite Structural Module

As high-fidelity post-deformation view factors are not necessary for a small-deflection temperature analysis, COMSOL was used to model the effects of altering the current composite laminates to include such a highly thermally conductive layer. To examine the temperature field, which is almost completely uniform in the length direction, a 25-cm structure model was used; to magnify the effects on structural deflections, a 5-m structure model (constructed of multiple joined structural units, as shown in Chapter 5) was used.

While adding a layer to the established composite laminate definition is straightforward, the choice remains as to which side of the material to put the graphite layer—i.e. the convex or concave side of the flanges. While putting the layer on the convex side would alter the surface properties of the composite structure less, it

would also interfere with the flange-to-flange bonding needed to form the web if not trimmed to only cover the flanges; this is because if the graphite material is bonded to laminae on both sides, it simply flakes and delaminates.

Regardless, both situations were simulated, and the concave graphite placement was predicted to have lower temperatures and deflections; these results are shown in Figure 4.3. The difference in web and flange temperatures between the two structures is noticeable, with the graphite bringing down structural temperatures by around 30°. However, the difference in 5-m structural deformations is dramatic: graphite reduces deflections by *over an order of magnitude*. Such an extremely promising result motivated a full structural integration as described below.

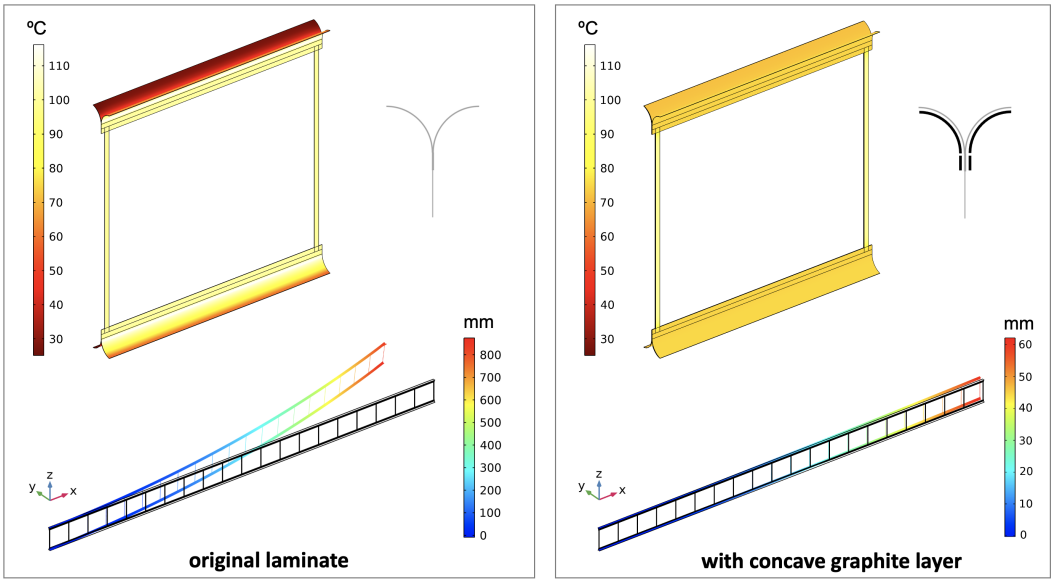

Figure 4.3: Simulated temperature and deflection fields of modules constructed from a) original carbon-fiber laminate, and b) graphite-composite laminate, with the graphite layer place on the concave side of the flange and web.

4.4 Structural Module Fabrication

Therefore, a structural module was manufactured that incorporates a graphite sheet on each concave side of the flanges. The technique for doing so was identical to the construction discussed in Chapter 2; since the concave side of the flange is shaped by the convex surface of the semi-circular mold, the graphite sheet had to survive direct contact with the outside of the vacuum bag. Figure 4.4 shows the finished graphite-composite structure after subsequent paint speckling for DIC. Of interest is the visibly increased surface reflectivity due to the graphite layer.

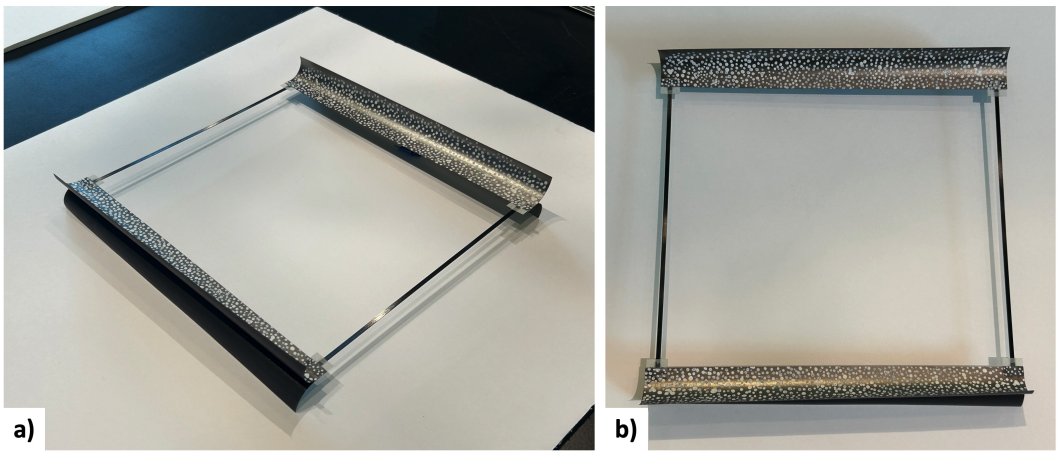

Figure 4.4: a) Fabricated graphite-composite structure after DIC speckling. b) Front view showing increased surface reflectivity.

When bonding the battens to the completed longerons with glue, flaking and delamination of the graphite was observed to foul and un-secure the structural joint. This was remedied by carefully removing the layer of graphite that would be underneath the glass tapes and glue, then bonding the battens to the longerons. The minute local removal of material was not expected to affect the global thermal properties in any noticeable manner, and ensured that the joint stiffness between graphite-composite and ordinary composite structural modules was identical.

4.5 Structural Experimental Results

The structure was then placed in the acrylic vacuum chamber, and trials measuring its deflection and temperature profile over time were conducted in an identical manner and procedure as the tests of Chapter 2.

Due to the slightly increased surface reflectivity of the exposed graphite surface, the DIC measurements were slightly affected, while the thermal measurements had to be significantly modified.

For DIC measurement image quality, it was difficult to illuminate the structure sufficiently without some undesired reflections washing out portions of the speckle pattern; therefore, the amount of reflection was carefully minimized, leaving a portion of the bottom left longeron deliberately washed out in the process. The loss of data is insignificant and still allows for ready comparison of the right side of both longerons with previous structural trials.

For the former, care was taken to place the transient "tooltip" temperature readouts

on points of the flange that appeared to not reflect the glint of the DIC lights or infrared lamp; such glints effectively spoofed erroneously high temperature values, and had to be carefully avoided. Despite these precautions, accurate temperature values were unable to be obtained for the graphite sample; therefore, to achieve temperature measurements, two thermocouples were placed on the top and bottom flanges in the same locations for a single trial, with the deflection left unrecorded.

Infrared Thermography Results

Figure 4.5 a) shows an infrared image of the graphite structure near the end of a trial (i.e. at its hottest); this is purely a qualitative image, as the temperatures were shown to be erroneous by subsequent thermocouple measurements. Figure 4.5 b) offers a "tooltip" temperature vs time plot of this representative trial using thermocouple data, with dashed lines comparing the original composite structure's transient temperature curve.

Readily visible is the significant reduction in heating-induced temperature change for both graphite longerons. The noticeable difference in temperature between the two flanges, even before the lamp was turned on, could have been a result of the residual heating caused by the DIC lights. Regardless, the temperature fields and gradients are still much lower than those of the original composite structures.

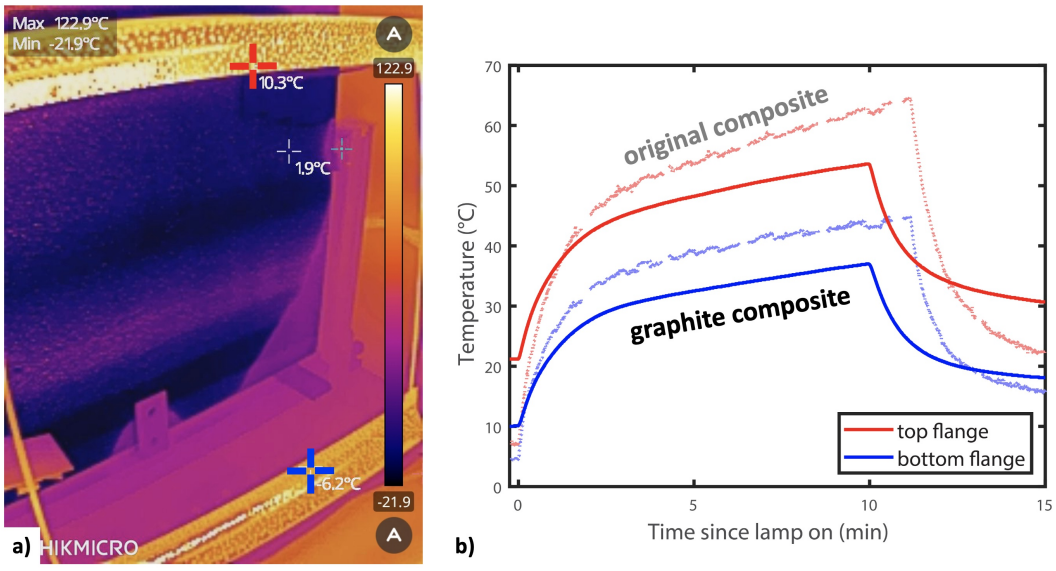

Figure 4.5: a) IR image of peak graphite composite trial temperatures, with tooltip temperature readings at red and blue crosses; b) the graphite composite thermocouple readings compared with those for the original composite structure.

Deflection Results, Compared to Current Single Structural Modules

Calculating the deflections of the graphite structures involved a slight nuance, since the deflections measured were small enough to push the limits of the DIC measurement technique.

Figure 4.6 shows the measured z-coordinates, and therefore deflections, of points on a straight line along the web-flange boundaries during a representative graphite structure trial. If one measures the maximum displacement of the structure between the "lamp on" and "lamp off" states, the right side of the top longeron moves 0.23 mm, but the left side (measured 10% of the longeron length from the clamp) moves 0.141 mm. However, the left side of the top longeron is clamped; this means that either the clamp moved (and thereby moved the entire structure with a rigid-body motion), or the noise of the DIC algorithm erroneously ascribed deflection to that part of the structure. Since that amount of deflection is within the noise floor of the DIC measurement (as determined by previous testing), the latter is the more likely scenario.

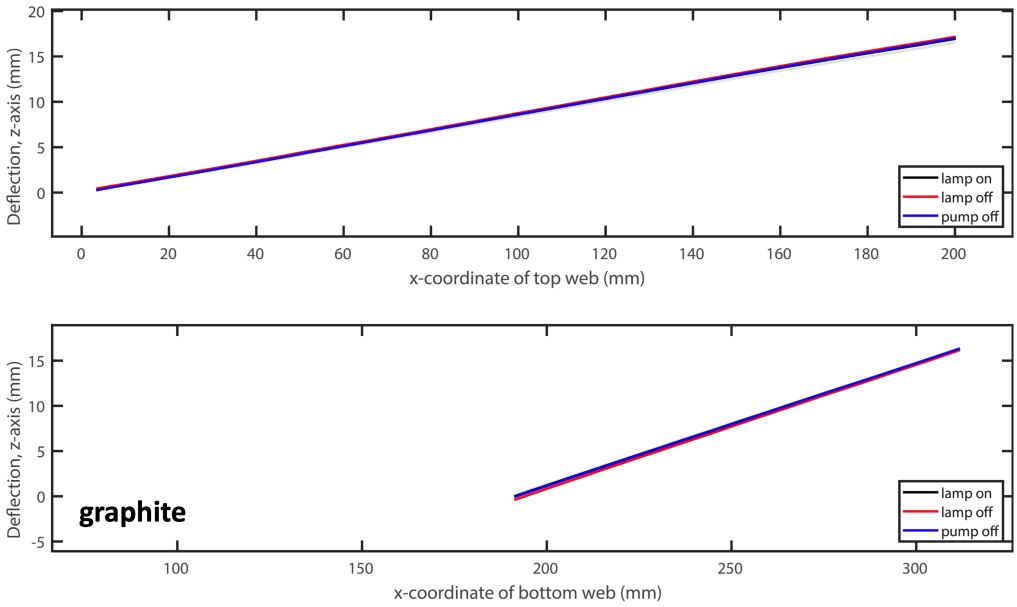

Figure 4.6: Deflections of a) top longeron and b) bottom longeron of the graphite sample just before heating (black), just after heating (red), and just after cooling (blue).

To subtract out the effect of the erroneous clamp "deflection", one must determine how much of the left side's deflection could be ascribed to it. Since the DIC camera angles did not allow for a simultaneous view of the clamp, one must instead make use of the closest point to it, which was 10% of the longeron length away. This

Table 4.1: Experimental upper-bound rightmost deflection results for graphite

Graphite Sample, trial	**13**	**14**	**15**	**average**
top deflection (mm)	0.12	0.083	0.025	**0.076**
bottom deflection (mm)	0.26	0.34	0.30	**0.30**

leftmost deflection measurement consists of an erroneous deflection (assumed to apply equally to all parts of the structure) and a real deflection caused by the thermal gradients.

If one assumes that the structure nonlinearly bends, a conservative assumption for this real thermally-induced deflection of the leftmost measured point would be 10% of the rightmost deflection; this is equivalent to drawing a straight line from the clamp to the rightmost longeron tip and taking the value 10% of the way in. The actual value of the thermal deflection must of course be smaller than this, but it can be no greater. Subtracting this from the measured deflection at that point gives us a lower-bound estimate of the erroneous deflection of the structure; subtracting this value from the rightmost deflection measurement, then, gives an upper bound on the rightmost deflection.

These *upper bound* estimates are presented in Table 4.1 and in Figure 4.7—and they are all much lower than those of the original composite structures shown in Table 2.2; the deflections on the bottom longeron are nearly 3 times less, while the deflections of the top longeron are over 17 times less! This stark difference confirms the profound difference that adding graphite to the composite structures makes, and advocates for its proposed use in reducing thermal deflections of space structures.

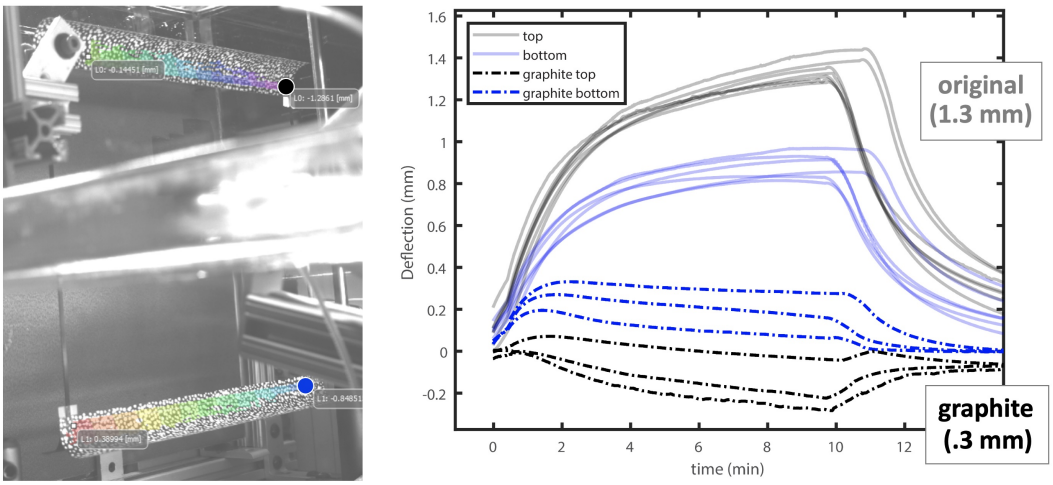

Figure 4.7: Comparison of the deflections of the original laminate and graphite-layer laminate structural deflections at the rightmost longeron edges.

Chapter 5

COUPLED SIMULATIONS OF FULL-SCALE STRUCTURES WITH VARYING RADIATION VIEW FACTORS

...comprendre c'est avant tout unifier.
...to understand is, above all, to unify.

Albert Camus, *Le Mythe de Sisyphe*

Parts of the first section were modified from the following publication:

[1] JM Pederson and S Pellegrino. "Thermal Deformation of Ultrathin Composite Structures in a Vacuum Environment." In: *AIAA SCITECH 2024 Forum* (2024). DOI: 10.2514/6.2024-0412.

With simulations of module-scale structures complete, the groundwork has been laid to model beyond the laboratory, as it were—to examine thermally induced deflections of realistically sized structures. For the purposes of this thesis, and in the interest of keeping simulation times manageable, these sizes range from one meter (i.e. four 25-centimeter modules) to five to ten meters in extreme cases.

For the most complex thermal and dynamic transient simulations, a structure length of two meters was the maximum length able to be simulated in a reasonable amount of time. This length corresponds with both a threshold in dynamic fundamental mode frequency (detailed herein) and the actual size of the SSPD-1 DOLCE prototype [11], making it a convenient size to study in depth.

Detailed in the first section of this chapter, the first foray into these more realistic simulations is a simple extension of the previous simulations of the experiment; starting with the same model of the sample, extending its longitudinal dimension modularly, but then removing the chamber walls and lamp and replacing them with sunlight and a room-temperature radiative background. These simulation conditions, while not representative of the space environment, yield temperatures and deflections that are more readily comparable to experimental and simulation observations. These models also provide a virtual, reasonably scaled testbed to examine the effects of material and structural parameter variation on temperatures and deflections—the

results of which, presented here, proved both enlightening and a potential means of improving future structures.

However, a major goal in simulating these larger structures was to model and observe the nonlinear, coupled effect of deflection on the temperature field; when the structure deforms enough to invalidate the radiative view factors initially calculated, the simulation should recalculate the radiative view factors to update the heating load experienced by the deformed structure. For multiple reasons, these initial COMSOL simulations were unable to do so, marking the limit of their predictive power.

To progress, it was therefore decided to combine two existing finite-element-analysis softwares (Thermal Desktop and Abaqus) into a fully coupled thermo-mechanical simulation by means of MATLAB scripting, in the manner of Dr. Olive Stohlman's work with structural booms [41]. This work extends such analysis to full-scale structural assemblies, as well as to both quasi-static and thermal/dynamic transient analyses, depending on the use-case requirements. By recalculating the radiative view factors after every time step, this Abaqus-Thermal Desktop (ATD) fully coupled simulation allows for unprecedented accuracy in predicting deflections caused by changing heating conditions. A full outline of the procedure and comparisons with similar COMSOL simulations is the subject of the second section.

In the third section, this custom simulation technique was applied to a use-case very relevant to a space-solar-power-project structure: a rapid rotation maneuver by the large spacecraft to maximize power generation and transmission. The flexible dynamics of such a slew maneuver, as well as the time necessary to accomplish them safely, have been studied in depth by Dr. Michael Marshall [25], revealing that a rotation of 90 degrees over a period of ten minutes is expected in medium Earth orbit. Focusing on a single strip structure, the dynamic deflection response of the structure from thermal effects alone is examined, as the rapidly changing view factors and structural self-shadowing rapidly change the temperatures thereon. Such a simulation would be impossible to accomplish without view factor recalculation, and as such represents the high-water mark of the simulations of the present work.

5.1 Large Structural Simulations in COMSOL Multiphysics

First, a series of simulations of the sample structure, in its original length as well as extended to 1-meter, 2-meter, and 5-meter variants, were performed using the finite-element software COMSOL Multiphysics®. These predicted the temperature fields and thermal deflections for the structures under radiant heating from one side,

i.e. sunlight.

An important note: these simulations were conducted using a geometry almost identical to the previously described DOLCE section, minus that the longeron flanges have a subtended angle of 80°. This geometry was chosen at the time primarily to compare with equally dimensioned contemporaneous experiments, and is not used in any other simulation outside of this section.

Simulation Setup

In order to model the thermal-structural effects from radiant heating, as well as coupling among these effects, several COMSOL modules were effectively chained together. Note that the entire strip geometry is constructed of thin shells – thus, only the shell heat transfer modules, shell mechanics, and shell elements of COMSOL were used. To model the transfer and spreading of heat among the shells of the strip, the Heat Transfer in Shells module was used, and was coupled to the Surface-to-Surface Radiation module by means of the Heat Transfer with Surface-to-Surface Radiation multiphysics module. To model the thermal expansion of the shells, as well as to capture the clamped root boundary condition of the longeron, the Shell solid mechanics module was used, with a Thermal Expansion component added under the Layered Linear Elastic material definition.

The composite materials were modeled using the Layered Materials of the Composite Materials Module, the layers being the orthotropic glass-fiber plain-weave and unidirectional carbon-fiber laminates specified in Section 2.2. The mechanical properties of both laminae presented in Table 2.1 were used directly, while both laminae were given the same laminate thermal properties as in previous simulations.

The radiation boundary condition in all cases modeled sunlight shining on the structure; therefore, parallel rays of light at a flux of 1361 W/m^2 were specified as an External Radiation Source, part of the Surface-to-Surface Radiation module. The initial temperatures, as well as the background radiation temperature, were set to 293.15 K, i.e. room temperature.

Single Strip Unit

The geometry of the basic unit was replicated in COMSOL using various geometries. The two longerons were formed from the union of three parametric surfaces: two cylindrical sections corresponding to the curved flanges, and one thicker rectangle joining them at one end corresponding to the web. The battens are rectangular

prisms. In reality, the two longerons are joined to the battens using small rectangles of single-ply glass-fiber plain-weave composite; this attachment was modeled by means of the rectangles intersecting the battens and web, then forming a union of all three—see Figure 5.1. The separate components maintain their respective material properties, which were specified individually.

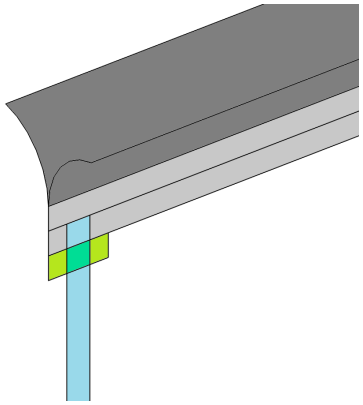

Figure 5.1: A detail of the geometrical connection between the longeron web (light gray), batten (light blue), and glass-fiber plain-weave connecting tape (light green), with the overlap between the last two (green). The horizontal line splitting the web lengthwise is a non-physical internal boundary for better mapped meshing.

As the simplest possible base case, the structure was modeled with nominal dimensions and no manufacturing defects; this ensures that the structure is symmetrically illuminated, which should in turn create a symmetric temperature field.

The results of running a stationary (i.e. steady-state) linear coupled analysis are shown in Figure 5.2, which shows temperature at left and y-deflection at right. Several things are immediately apparent – the first of which is the large thermally induced deflection effectively twisting the structure. The resulting y-deflection is over 13% of the structure's length in magnitude, suggesting that an analysis of this structure assuming small deflections is likely to be inaccurate. While the thermal loads are partially coupled to the structural loads—i.e. the temperature field causes a thermal deflection field—the resulting geometrical nonlinearity must still be accounted for by recalculating the radiation field, as discussed earlier. This is attempted in Section 5.1 with limited success.

A detail of the temperature map, plotted on the undeformed structure for clarity, is shown in Figure 5.3 for a solar heat flux incident from the left. The effect of geometry and conduction on the temperature distribution is quite visible, and worth noting – the tip of the left flange, being parallel to the incoming heat flux, remains much

cooler than the rest of the flange, only heating via conduction from the heated portion; in addition, the right flange remains much colder, only heating due to conduction through the web. The uniformity of the temperature field along the length of the longeron demonstrates the lack of accounting for large deflections.

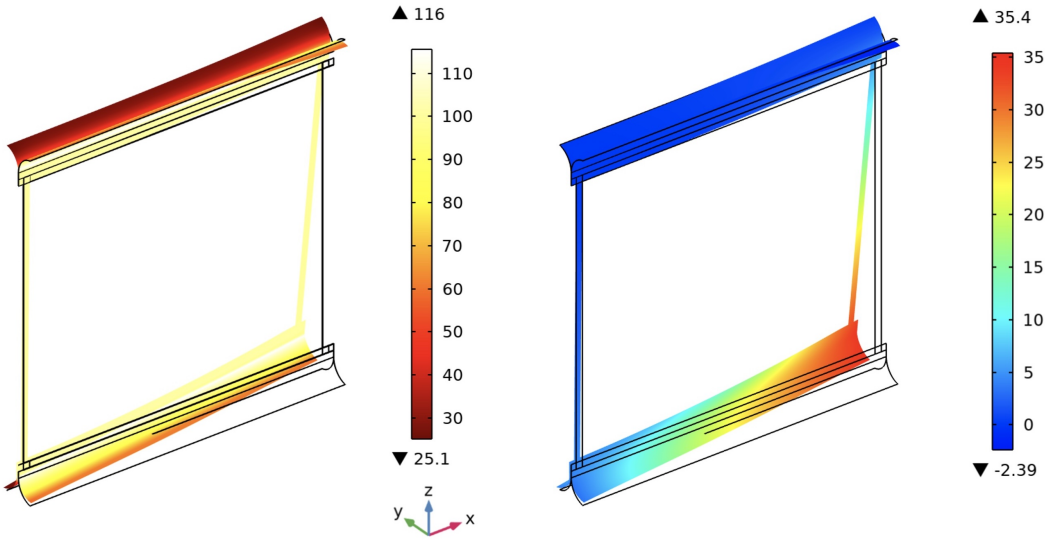

Figure 5.2: Temperature (left, °C) and y-deflection (right, mm) results for the 25-cm strip unit. The structure is rigidly clamped at the upper left corner and free at all other points; solar heat flux shines on the sample in the $+y$ direction. Black outline indicates the original unheated shape of the strip.

Structures with Multiple Units

The strip geometry was then extended to lengths more representative of realistic space applications; the two longerons were extended to nominal lengths of 1 m, 2 m, and 5 m, with the number of battens correspondingly increased. In order to keep the same inter-batten distance of 241 mm, the longeron lengths were slightly adjusted to maintain an integer number of structural units and the same strip edge finishes; for example, the nominally 1-m strip is in fact 0.977 m long to be an exact multiple of four strip units. See Figure 5.4 for a more detailed view of the 1-m strip as an example.

Stationary, coupled, geometrically linear simulations were run on all three lengths to obtain the y-displacement fields shown in Figure 5.5. The temperature fields of all three lengths are again uniform and lengthwise identical to the 25-cm model, due to the simulation not taking into account the large deflections and calculating the temperature field based on the undeflected structure. This fact means that such

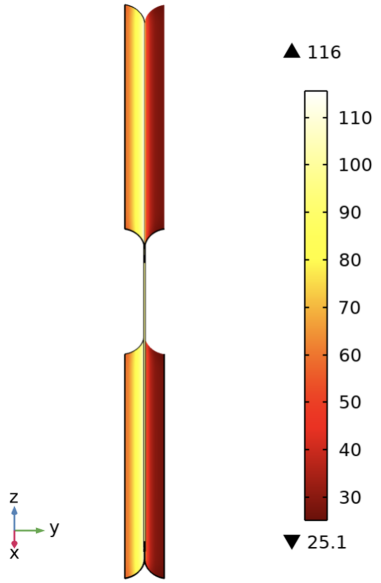

Figure 5.3: Temperature (°C) map as plotted on the *undeformed* 25-cm structure depicted in Figure 5.2 at left. Solar heat flux is incident from the left. The effects of both geometry and conduction on surface temperature are present.

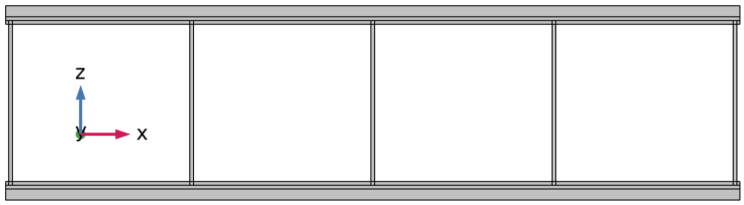

Figure 5.4: Detail of the 1-m structure; the extended geometry preserves the distance between battens (.241 m). Glass-fiber tapes on batten ends not modeled, as they do not have a significant effect on structural deflection.

deflections may be of limited accuracy, but serve as a baseline case to compare the effects of in-plane conductivity, twisting, etc. without the confounding effect of nonlinear deformation affecting the heating and temperature profiles.

The length of the 5-m structure, however, renders it somewhat less useful for this baseline case, since a small change in deflection anywhere along the structure can affect the deflection field for the entire remaining length of the structure. While a local deflection change can affect the global deflection for several meters in the 5 m case, the same change can only affect the global deflection for tens of centimeters in the 1 m and 2 m case. Therefore, only the 25-cm, 1-m, and 2-m structures are shown for the remainder of these geometrically linear studies, with the 5-m structure only referenced as an extreme case.

The above initial simulations have a thermally insulated root boundary condition—i.e. no heat is allowed to flow into the root support of the structure. This may be an unrealistic assumption: a clamped boundary condition can only be achieved with direct physical contact, so a well-clamped boundary condition will also have good thermal contact. If the effect of root conduction is included, it may also offer a means of varying the temperature field along the structure, which would cause a corresponding variation of the thermal gradients leading to the final deflection field.

Fixing the clamp temperature at 20°C allows for heat to be conducted into the root. (By contrast, a clamp temperature that tracks the structure's root temperature, for example, would be identical to a thermally insulated clamp.) All subsequent simulations were run with this "conductive root" boundary condition.

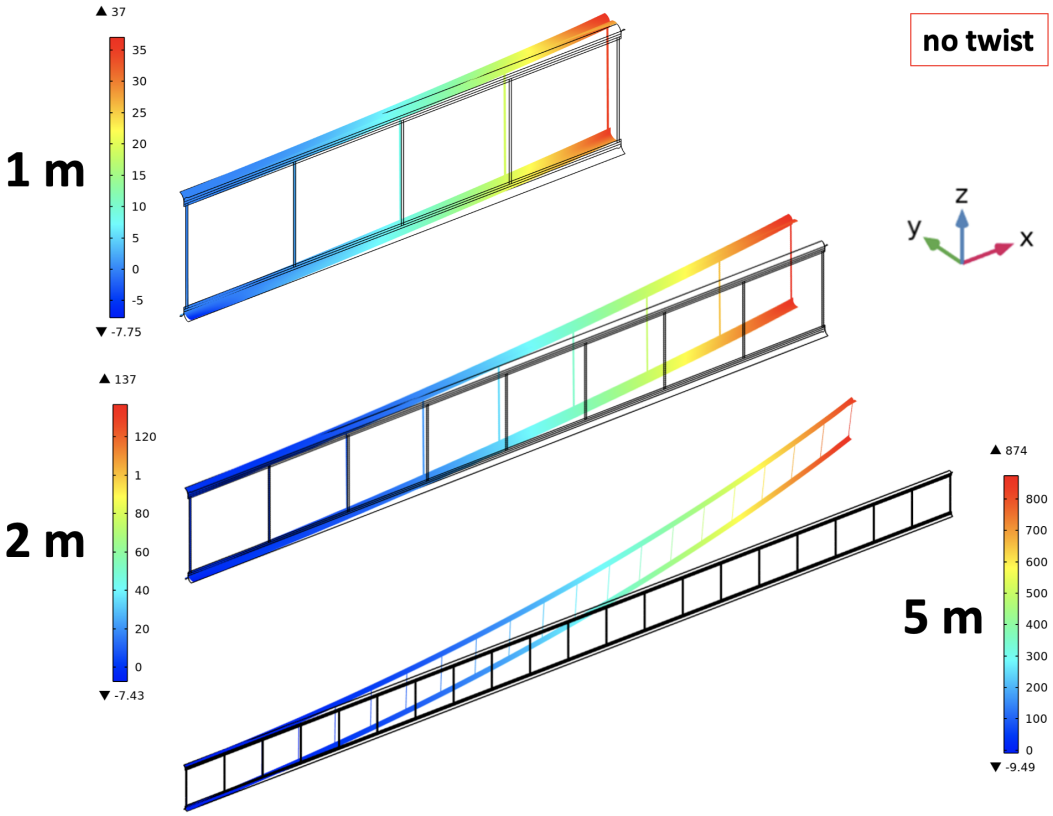

Figure 5.5: Deflection (mm) profiles of the 1-m, 2-m, and 5-m strips clamped at the upper-right corner, without modeling geometric nonlinearity. (This is a base case only, since the deflections are large compared to the structure and the temperature field has not been recalculated for the deformed geometry.)

Effects of Structural Properties

Having established working, deterministic multiphysics models of realistically-sized structures, we can now examine how varying critical material properties affects temperature and deflection fields in a controlled environment. The material properties of interest are 1) in-plane thermal conductivity of the laminate along the fiber direction and 2) transverse to the fibers, 3) laminate fiber misalignment, and 4) initial structural twisting. The first two are inherent in the orthotropic nature of carbon-fiber laminates, while the latter two are near-unavoidable manufacturing defects; examining the effects of each characteristic in turn yields much insight.

Effect of k_1

The thermal conductivity *along* the fiber direction, i.e. along the axis of the structure, might impact the steady-state temperatures and heat flow along the length of the structure, especially when heat is allowed to flow into the root clamp. However, the simulation reveals that the nominal thermal conductivity of our laminates along the fiber direction ($\sim 0.99 \frac{W}{m^2 K}$) is small enough that the cooling effect of the root quickly dissipates within a few millimeters of the structure's end; see Figure 5.6 for a closer view of the heat-affected zone. As such, the effect of heat conduction into the clamped root is negligible for our laminate values of k_1. Even values of k_1 two orders of magnitude higher, while penetrating a few centimeters into the longeron, still barely affect the global deflection of the structure; the maximum displacement of a 5 m structure is only affected by 12.8 mm, or about 1% of the total deflection.

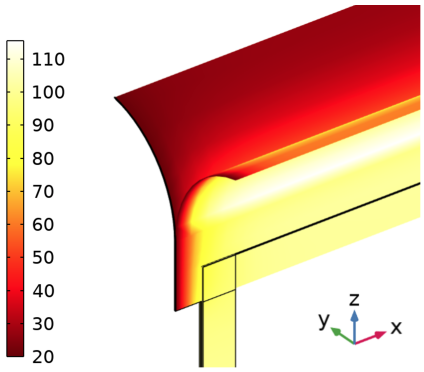

Figure 5.6: Detail of the heat-affected zone of the structure at the clamped root when heat is allowed to flow into the root, for a k_1 of 0.99 $\frac{W}{m^2 K}$, temperatures in °C. The region of reduced temperature only penetrates a few millimeters into the longeron.

Despite this, k_1 may remain an important factor in the deflection of long structures. Under sunlight, when large deflections cause significant variation in local heating

angle, the temperature field along the structure will also significantly vary; how well heat travels along the structure between such differently heated regions is entirely a function of k_1. However, if the magnitude of k_1 is small enough, such local variations may be unable to spread enough to make a difference in the overall deflection.

Effect of k_2

The thermal conductivity transverse to the fiber direction, i.e. across the flanges and web of the structure, has a more direct impact on the steady-state temperatures along the length of the structure, regardless of whether heat flows into the root clamp. In turn, since the thermal gradients (and expansions) along the flanges perpendicular to the fiber direction are the dominant cause of deflections therein, we would expect a variation in k_2 to have a much larger impact on the structure's deflection.

For our composite laminates, k_2 is roughly one-fourth of k_1 for the same laminate ($\sim 0.27 \frac{W}{m^2 K}$). Upon simulating this value of k_2 for the 5-m structure, when compared with $k_2 = 0.001 \frac{W}{m^2 K}$ (i.e. ~0) as a baseline value, the temperature field was affected by less than 0.01°C, while the deflection field was affected by a maximum of 1.9 mm. Even the upper bound on experimentally determined k_2, $0.66 \frac{W}{m^2 K}$, only affected the maximum deflection by 3.5 mm; in fact, non-negligible effects on these two metrics were not found until the value of k_2 was two orders of magnitude higher, at which point the effects became very significant (~38% less deflection). However, since our measured values of k_2 are much lower, these results imply that k_2 for our laminates and structures can be considered to be approximately zero.

These are two interesting points from the perspective of thin composite thermal property measurement and modeling: 1) transverse thermal conductivity is indeed the dominant cause of thermal gradients and deflections, and 2) the small thermal conductivity across the carbon fibers of the laminates used can be approximated as zero with almost no loss of accuracy.

Effect of Fiber Misalignment

A common defect in composite laminates is fiber misalignment – namely, the orientation of the constituent fibers differing slightly from the nominal direction of a unidirectional lamina. Such defects can result in waviness of the fibers themselves as well as overall fiber misalignments (i.e. every fiber of the lamina parallel but pointing in a direction other than the nominal one) [51]. Due to the complexity of modeling the former, we will instead model the latter; we simply adjust the laminate

model by rotating one of the constituent laminae a certain number of degrees, as shown in Figure 5.7. Fiber misalignment angles of up to 2° have been commonly observed experimentally [51], and this is the value used in this analysis. The modified laminate is then applied to both webs and two flanges, as shown in Figure 5.7 at left, and the same simulation performed again. This particular configuration of misaligned plies is the one that was found to result in the greatest amount of deflection difference.

The temperature field results, owing to the small-deflection assumption, are identical to the pristine laminate case; the deflection results are shown in Figure 5.7 at right and Figure 5.8 — only a small difference from the perfect laminate is detectable. Indeed, even at larger structural scales (2 m), the effect is negligible – Figure 5.8 shows a maximum of 2 mm greater deflection than the perfect laminate case, a difference of only 1.4%.

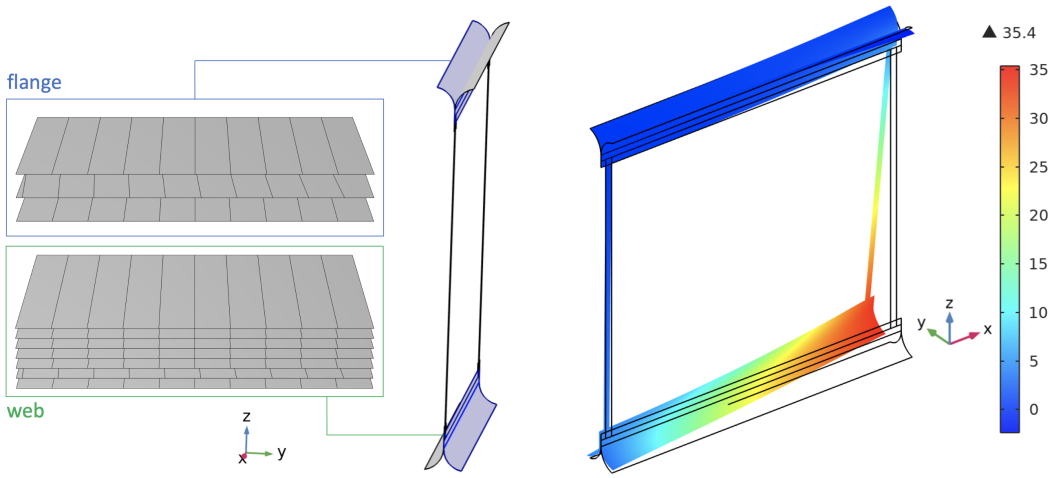

Figure 5.7: (left) Location of the two flanges and two webs with (left inset) laminates altered by rotating one of the carbon fiber plies 2°, with (right) the resulting y-displacement field (mm), almost identical to the pristine laminate case above.

Effect of Realistic Initial Twist

A common manufacturing defect in carbon-fiber strip structures is the presence of twist, both in the longerons themselves and in the structure formed by the two longerons; in addition, the lack of torsional stiffness in the basic unit magnifies any existing twist present in the longerons or battens. Unintentional twisting from any of these causes during the manufacturing process manifests itself in the twisting of the

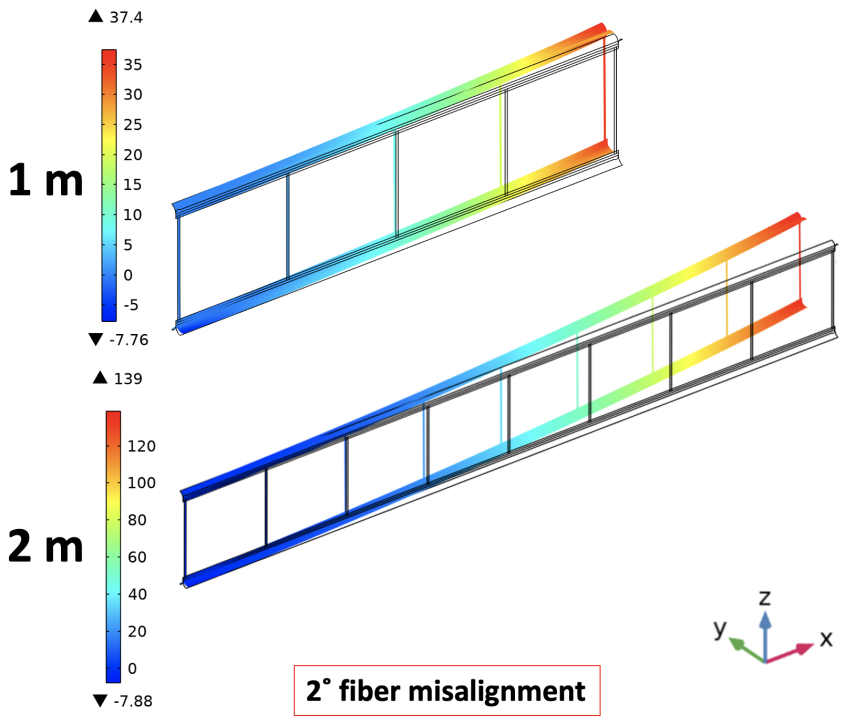

Figure 5.8: Deflection (mm) profiles of 1 m and 2 m strips clamped at the upper-right corner with fiber misalignment in the same laminate configuration as the 25 cm case presented above.

entire structure about the longitudinal axis unless twisting is prevented by boundary conditions.

The effect is introduced here by modifying the structural geometry such that it forms a helical ladder shape. No residual stresses are induced by such a definition; this matches the negligible stresses that appear to be present in a nearly perfect sample allowed to twist. Experimentally, a fraction of a sample ultralight structure's self-weight is sufficient to completely straighten it, showing the small size of the residual internal forces.

The value of the longitudinal twist, chosen to be 4.8° per structural unit, was taken from measurements of previous units tested with this geometry; though it was improved to 1.3° for the structures used in the experiments presented in Chapter 2, it is still a very common defect magnitude despite careful manufacturing. The twist amount is also assumed to add for each structural unit added; therefore, a four-unit structure would have a twist of 19.2°. Additionally, assuming this twisting chirality to be random, both 4.8° and -4.8° of twist were simulated – positive twist being counterclockwise as viewed looking down the structure to the root, and negative

being clockwise.

Results for +4.8° twisting angles are presented in Figure 5.9, and for -4.8° twisting angles in Figure 5.10. When compared with the results for untwisted structures under identical heating in Figure 5.5, the difference is dramatic: even for the smallest structure, less than five degrees of structural twist causes deflections 50% of the magnitude, but *in the opposite direction* of the untwisted structures' deflections. This sensitivity indicates how much the temperature field and gradients are affected by structural deflections; even a small change in structural geometry has an outsized effect on the final deflection result.

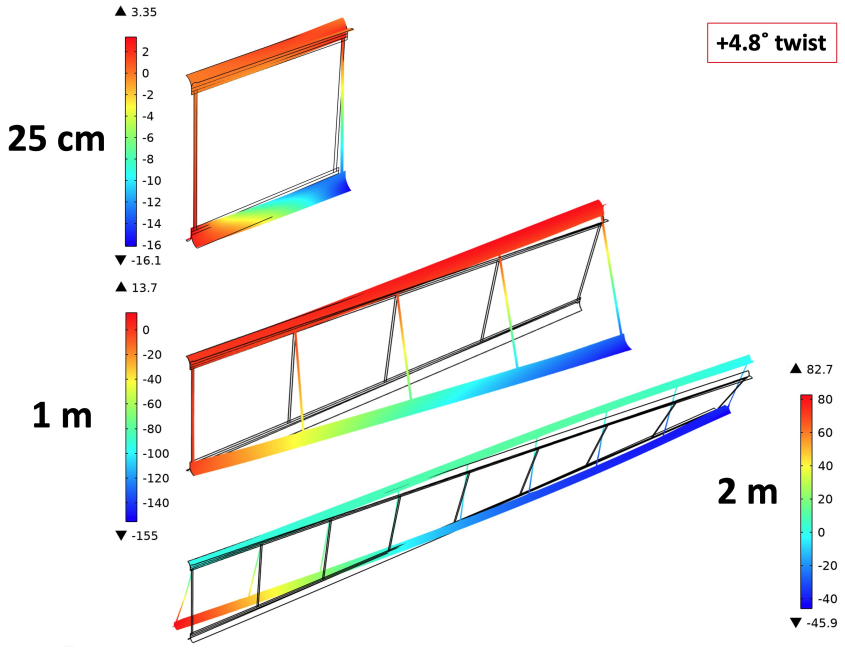

Figure 5.9: Deflection (mm) profiles of 25 cm, 1 m, and 2 m strips clamped at the upper-right corner with realistic initial twist, +4.8° (i.e. counterclockwise looking down toward the clamped root).

Effect of k_1 with Twist

Since structural twist produces a spatially varying temperature field, one might think the effect of k_1 would become noticeable – but upon examination of both twist angles (±4.8°) for the 25 cm, 1 m, and 2 m models, no difference in deflection greater than 0.1 mm was observed for any case, even for values of k_1 two orders of magnitude higher than that of our material samples.

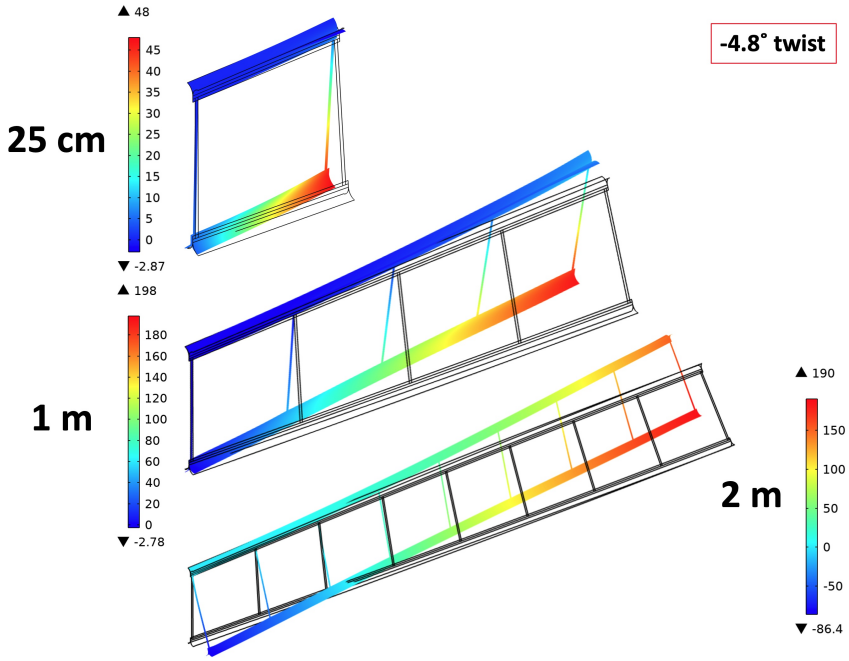

Figure 5.10: Deflection (mm) profiles of 25 cm, 1 m, and 2m strips clamped at the upper-right corner with realistic initial twist, -4.8° (i.e. clockwise looking down toward the clamped root).

Geometrically Nonlinear Simulations

Finally, stationary, coupled, geometrically nonlinear simulations were performed on the untwisted 25 cm, 1 m, and 2 m structural models. In these simulations, the final heating load is achieved by slowly ramping up the heat load, calculating deflections along the way while taking into account any buckling behavior that may occur. Long before the nominal value of the solar flux was reached, however, highly nonlinear buckling effects were encountered for all structure lengths. As the heat flux was ramped from 0 to the nominal solar constant of $1354\frac{W}{m^2}$, buckling was observed relatively early on in the ramping process, severely limiting the ability of the solver to approach the final nominal value in later cases. The longer the structure became, the earlier the solver failed to converge in the ramp. Figure 5.11 shows the nonlinear deflection results at the maximum flux for which each structure was successfully able to converge, while Figure 5.12 compares the linear and nonlinear deflection predictions for the 25-cm and 1-m structures recalculated at their maximum fluxes.

Unfortunately, COMSOL is unable to recalculate the radiative view factors in any simulation other than a geometrically nonlinear and time-dependent analysis. Even though this recalculation is critical to obtaining a radiation and subsequently a

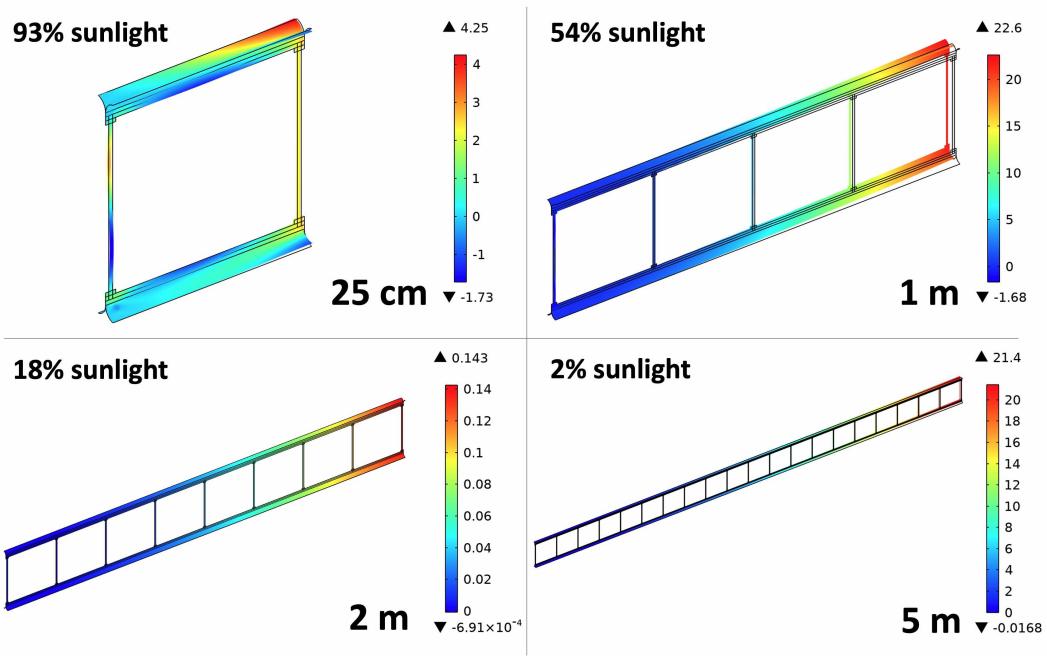

Figure 5.11: Deflection (mm) profiles of 25 cm, 1 m, 2 m, and 5 m strips clamped at the upper-right corner with geometric *nonlinearity* simulated, each at the maximum heat flux that successfully converged. Buckles have formed in a few battens, e.g. the leftmost batten of the 25 cm structure –see Figure 5.12 for a closer view.

temperature field that is different from the small-deflection case, the significant nonlinear buckling behavior of the structures in a steady-state analysis rendered them almost totally unable to be modeled in a transient analysis.

Since this nonlinear analysis meant that the structure is not modeled linearly, the solver must in fact be able to handle changes in the stiffness matrix, including those that may make it have negative eigenvalues—indicating buckle formation such as those seen in the results of Figure 5.12. The longest time duration for which a solution converged at the nominal solar heat flux was 0.0039 seconds, and even attempting to update the radiation view factors every 0.0009 seconds failed to reproduce the desired change in local irradiation across the structures. Therefore, for untwisted structures, obtaining deflection results that truly couple to the radiative field varying along the length, which in turn results in a temperature field varying along the length, still proves elusive for COMSOL simulations, and would appear to be best pursued with other software such as Abaqus and/or Thermal Desktop.

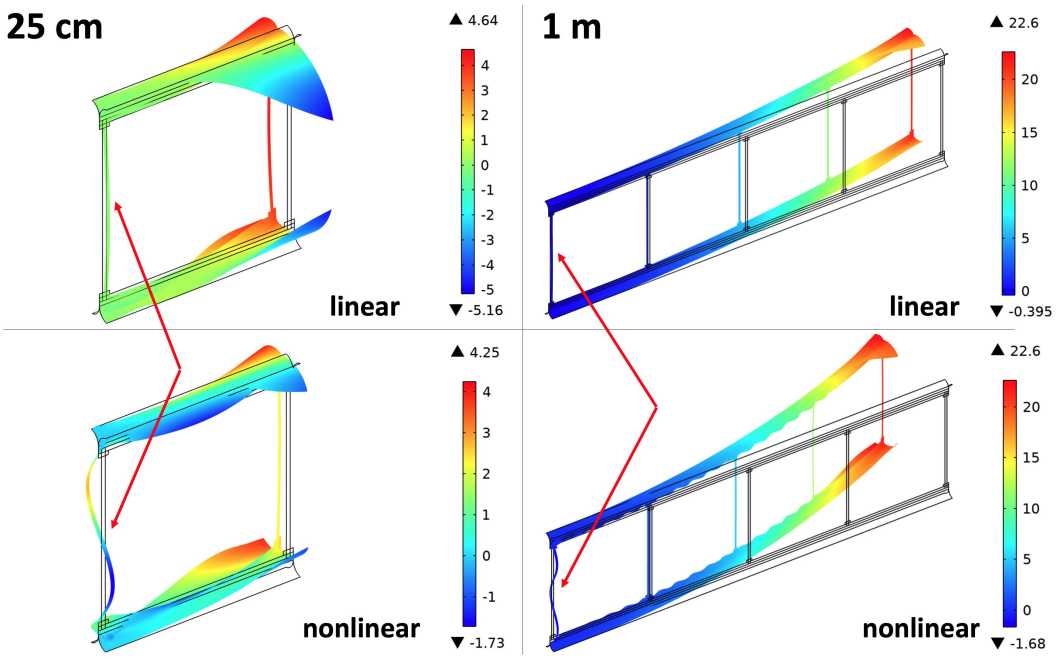

Figure 5.12: Exaggerated deflection (mm) profiles of 25-cm and 1-m strips with geometrically linear and nonlinear simulations compared, each at the maximum heat flux that successfully converged (deflection exaggerated by a factor of 10). Note the buckles on the leftmost battens.

5.2 Abaqus / Thermal Desktop Coupled Simulation

To address this inability of COMSOL to perform sufficient radiative view factor updates for our structures, two industry-standard finite-element-analysis softwares were coordinated to do so via a custom MATLAB code.

Abaqus, used extensively in the field of thin-shell structures to model deformations and even nonlinear buckling, was used to predict quasi-static and dynamic deflection fields given temperature fields. Unless otherwise noted, our structures did not buckle during these simulations, meaning that linear deflection analyses were sufficient. (This linearity in deflection response is different than the nonlinear effect caused by displacement-heating coupling.)

Thermal Desktop, able to robustly model radiative environments of arbitrary complexity, was used to calculate structural temperatures; its ability to calculate radiative view factors for both ambient radiation loads and on-orbit environmental conditions (for example, earthshine) made realistic analyses of orbital deflections possible.

In this section, the initialization of the models used in this technique, followed by a step-by-step account of the procedure involved, is detailed; a comparison with the

COMSOL model of Section 5.1 follows.

Prior Work

The particular approach to coupling these two software was first accomplished by Stohlman in 2018; working from an analytical coupling analysis of Prof. Joseph Blandino, Stohlman performed a dynamic analysis of a boom of circular cross-section heated by a step load of sunlight [4, 41]. Models of the boom were created in both Abaqus and Thermal Desktop, both having identical meshes. After a sufficiently small step size (0.2 s) was chosen, an Abaqus dynamic simulation was performed for this step length; the displacements from this analysis were passed to and incorporated in the Thermal Desktop model, which was then simulated to obtain the temperature field experienced by the deformed configuration. These temperatures were then exported and applied as a temperature field to the Abaqus simulation, which was then restarted to run for another step length [41]. The resulting increase in accuracy made a non-negligible difference in the deflection results predicted, and as such gave confidence to the prospect that such a coupling could dramatically improve accuracy in more advanced models, such as those presented here.

Model and Script Preparation

The basic premise of this Abaqus-Thermal Desktop coupling is largely identical to Stohlman's method, but expanded to handle more complicated structures, as well as perform various types of quasi-static and dynamic analyses.

Abaqus Model

The modeling process started in Abaqus, where a model of the structure was generated similar to previous COMSOL ones, but with a few differences due to differing software characteristics. As Abaqus does not have the "union" feature of COMSOL to make the geometry one continuously connected object, the longerons and battens were created as individual parts joined by tie constraints. More specifically, the flanges and web of each longeron were drawn as one single cross-section that was then extruded into the desired nominal length (e.g. 0.254 m for the nominally 25-centimeter structure) to create each longeron; each batten was merely a 2D rectangle, comprised of shell elements whose thickness was modeled as a material property. The plain-weave glass-fiber tapes connecting the battens to the longerons were not modeled, as they were found to have negligible impact on simulated structural deflections.

Once these parts were made, a mapped mesh of shell elements approximately 2 mm square was created on each part; this allowed for the top two elements of each batten to be selected and attached to the longeron webs by means of a tie constraint.

The material properties assigned to the longerons were composite laminate shell sections made up of individually defined glass-fiber and carbon-fiber layers (and later, graphite-polymer layers), taking care to ensure their orientations were such that the carbon-fiber direction ran parallel to the longeron. For modeling the original composite layup, these lamina properties are identical to the ones used in all other simulations, listed in Table 2.1. When a graphite layer was introduced to the simulated laminate, as will be seen, the 12-μm lamina had the structural properties E = 40 MPa and ν = .17, as well as the thermal properties of an in-plane CTE of $28{\cdot}10^{-6}$, a through-thickness CTE of 0, an in-plane thermal conductivity of 1800 W/m·K, a through-thickness thermal conductivity of 5 W/m·K, and a specific heat of 850 J/kg·K. Separate laminates were assigned to the flange and web regions of the longeron according to the real-life laminates used for each region. The pultruded carbon-fiber battens were assigned orthotropic properties known from manufacturing specifications and prior lab testing.

Simply-supported boundary conditions were applied to the Abaqus model, chosen for their insensitivity to end web deflections relative to a clamped boundary condition at one end. This was implemented by fixing all three degrees of translational freedom at the top left web corner, fixing the x- and z- degrees of translational freedom at the bottom left web corner, and fixing the z-degree of translational freedom (i.e. out-of-plane) of the right two corners. See Figure 5.13 for an illustration.

A predefined temperature field of 20°C was applied to all models in the Initial step; this represents the (room) temperature of the structure as manufactured (and therefore stress-free and undeformed), and defines the reference temperature to which all subsequent temperatures are compared when calculating thermal expansions.

A single simulation step was defined for all simulations, steady-state and transient alike; the former used a Static, General step, and the latter a Dynamic, Implicit step. Both types of steps were run and restarted by the MATLAB code described later.

Thermal Desktop

The Thermal Desktop model geometry was constructed by importing the Abaqus geometry as an exported NASTRAN .bdf mesh file; this means that both software

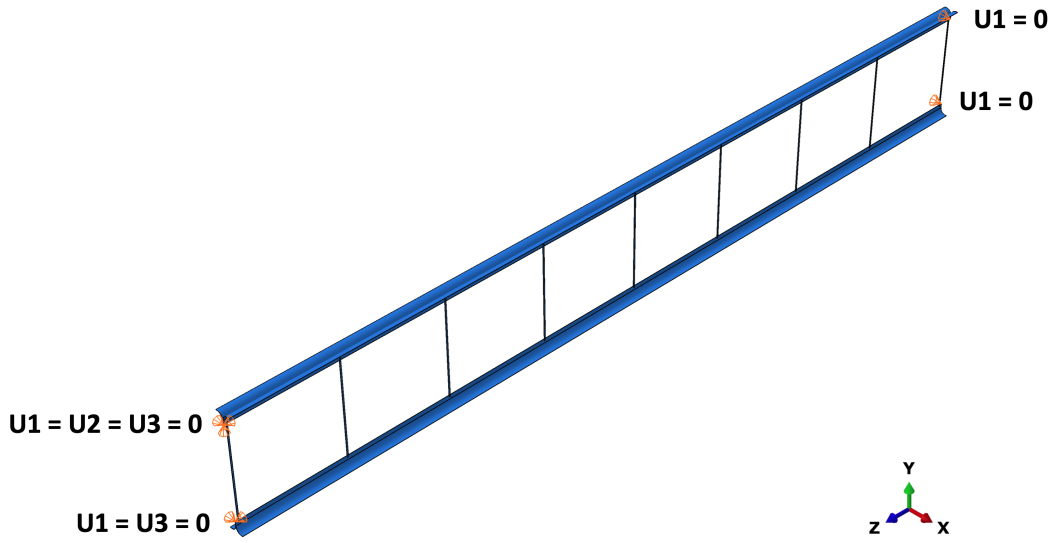

Figure 5.13: The simply-supported boundary conditions used for the slew maneuver simulations. (U1 = x-displacement, etc.)

models had an identical node numbering system. Note that the thermal model did not require any physical boundary conditions or constraints.

Thermal material properties were defined for each group of elements representing the webs, flanges, and battens; the properties used were the same as those of all other simulations, those of Table 2.1, with the properties of unidirectional carbon fiber being used for the pultruded carbon fiber battens due to near-identical composition.

Optical material properties, including solar absorptivity and infrared emissivity, were specified as 0.90 and 0.88, respectively, according to testing performed by TA Instruments on laminate coupons.

Two thermal constraints were placed on the model: a radiative boundary condition and a heat load. The first was an adjustable "space" temperature, referring to the radiative heat sink of unchanging temperature that defines a node-based temperature analysis. This background temperature was set to either room temperature (20°C) or "space" temperature (0 K), depending on the simulation performed, by adjusting the nonphysical space node temperature.

The second is the radiative heating applied to the structure model. In Thermal Desktop, sunlight heat loads are applied in terms of orbital parameters, meaning that an orbital height and spacecraft orientation must be selected. The parameters used to model basic sunlight were chosen to be the same as those detailed in the slew maneuver in Section 5.3: middle Earth orbit, β angle of 0°, position angle -90°,

with the structural x-axis pointed at the nadir. See Figure 5.14 for an illustration.

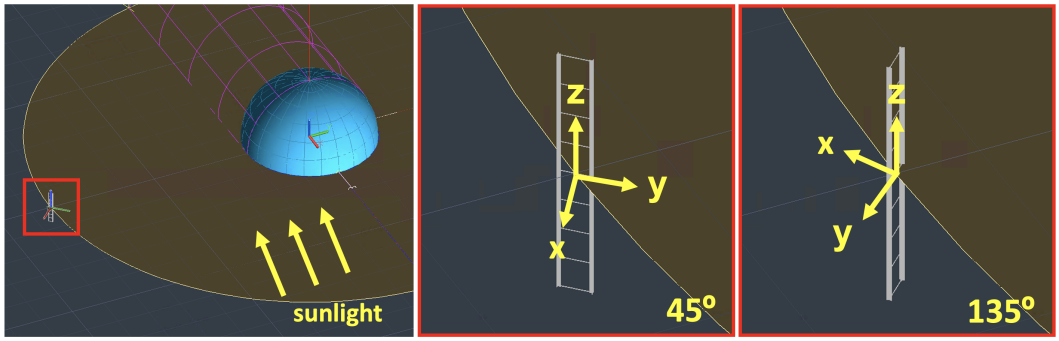

Figure 5.14: The simulated orbit orientation of the structure in the 45° and 135° positions.

Two types of simulation cases were used in the course of these simulations: steady-state and transient. Both cases used heating rates and view factors calculated from the radiative heating orbit; depending on whether orbital conditions were being simulated or not, the heat contributions from planetshine and albedo were checked or unchecked, respectively.

MATLAB and OpenTD

A MATLAB script was used to operate and coordinate both finite-element programs. To control the Abaqus runs, the script wrote or modified Abaqus input files (.inp) to start or restart analyses; it then ran these files from the command line.

To control Thermal Desktop, the API OpenTD was used. This C# library, used here inside a MATLAB wrapper, allowed for the modification of various model parameters and automated running of thermal cases.

Looping Procedure

Once the models and script are prepared, the iterative looping commences: Figure 5.15 provides a schematic overview of the entire looping process.

After creating the Abaqus and Thermal Desktop models as described previously, the MATLAB code is ran to begin the looping process.

The code looping starts by running the first Thermal Desktop analysis for the chosen step length (or until convergence for a quasi-static analysis) using the appropriate OpenTD command. Once the case has converged, the temperature data for each node is exported to an output file, which is then converted by the MATLAB script

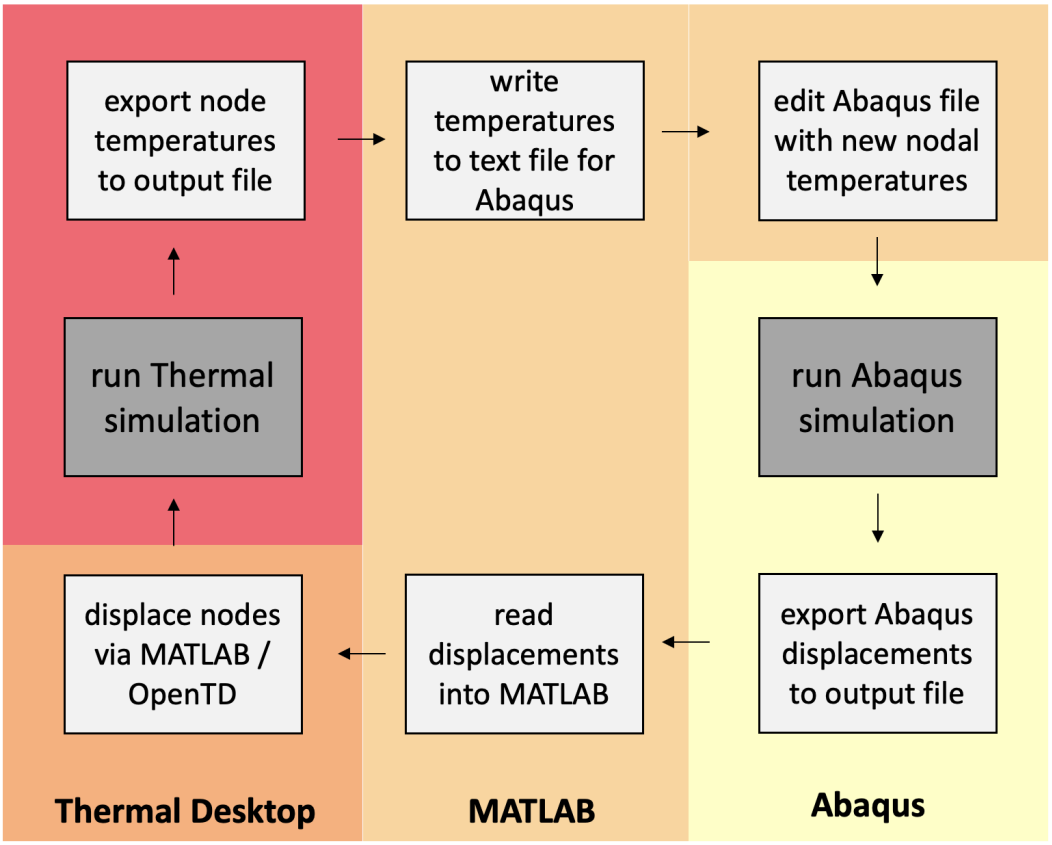

Figure 5.15: The workflow loop for the Abaqus-Thermal Desktop coupled simulations.

into a text file that can be read as an input by an Abaqus input file under the *TEMPERATURE keyword.

The MATLAB script then edits the original Abaqus input file such that the *TEMPERATURE keyword for the loading step (i.e. the Static, General or Dynamic, Implicit Abaqus step) refers to the node temperature file just created. It also generates an initial node temperature file, which for these simulations represents the temperature at which the structure was manufactured and is therefore unstressed; this file therefore consists of every node set to a room temperature of 20°C.

The MATLAB script then runs the Abaqus simulation by running this modified input file from the command line. Once finished, the node displacements are parsed from the Abaqus output file by the MATLAB script and are stored as internal variables.

Using OpenTD commands, the script then displaces the nodes of the Thermal Desktop model according to these most recent Abaqus deflections in memory. The thermal simulation is then ready to be run again, completing the loop.

This script-mediated looping will continue until one of two conditions are met: either when all of the displacements have converged to below a certain threshold (in the case of quasi-static convergence), or when a certain number of loops have elapsed (in the case of slew maneuvers of fixed duration).

Comparison with COMSOL

To ensure that this custom-built code was functioning accurately, the results of a quasi-static analysis were compared against a COMSOL model similar to the ones presented in Section 5.1. For both models, a sunlight heating condition illuminated a 25-cm structure, and the model radiated to a room temperature ambient heat sink. The simulated structure has a 80° flange opening angle instead of the 105° one used in the experiments and all other simulations.

The results of the analyses are shown in Figures 5.16 and 5.17. The temperature field is qualitatively similar between both models, most noticeably showing that the hottest areas are at the base of the front flanges. A quantitative comparison between various points on the battens, webs, and front and back flanges, as shown in Figure 5.17, supports this: the average difference between models is less than 5%, with the exception of the 17.4% outlier of the back flanges 1/4 of the way up. While the reason for this specific difference is unclear, the general differences are likely due to Thermal Desktop using a more advanced radiation-view-factor calculation scheme than COMSOL does (ray-tracing vs hemicube algorithm).

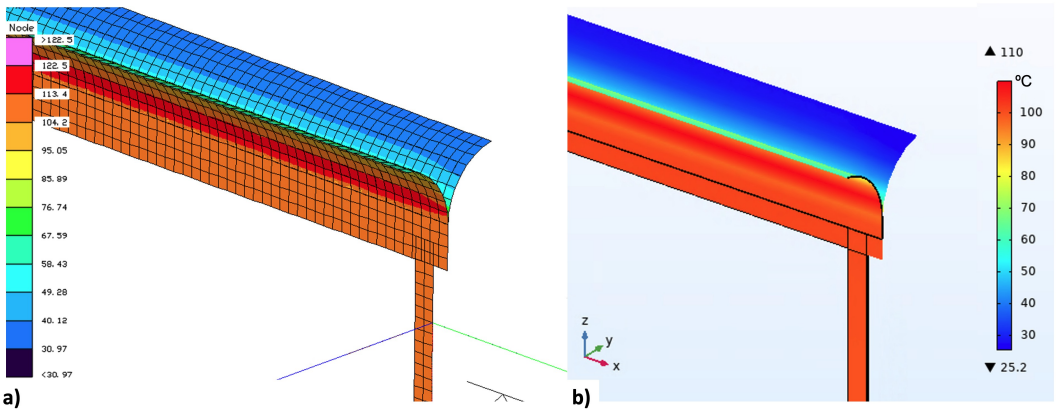

Figure 5.16: Comparison of identical models simulated by a) Abaqus-Thermal Desktop coupled analysis after the first loop, and b) the COMSOL models of Section 5.1.

A key advantage of the Abaqus-Thermal Desktop algorithm lies in its ability to simulate the effects of more complicated deflections than COMSOL via iteration,

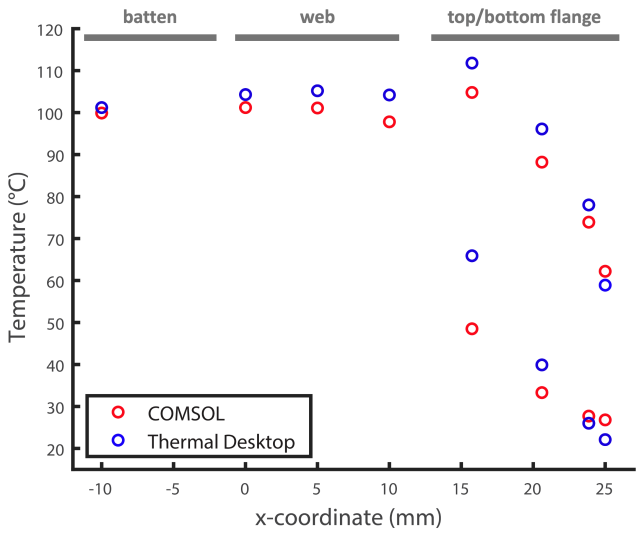

Figure 5.17: Comparison of the temperatures of the COMSOL and Thermal Desktop models of Figure 5.16 at various structural points.

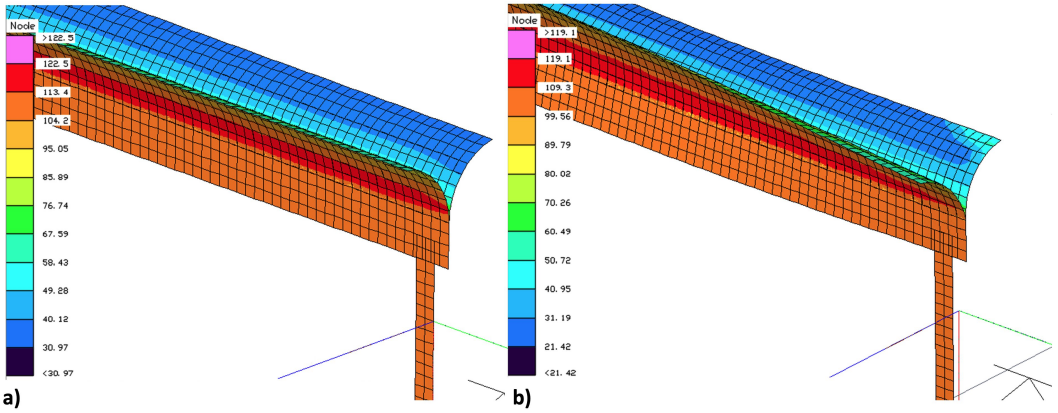

Figure 5.18: Comparison of the Abaqus-Thermal Desktop coupled analysis after the a) first loop and b) fifth loop.

as shown in Figure 5.18. Looking closely at Figure 5.18 b), the (hotter) front flange actually flattened slightly from thermal expansion and bending—an effect that is only accounted for in the thermal calculations on and after the second loop. This flattening rotates the front flange elements to face the sunlight more directly, increasing the impinging heat flux and therefore raising their temperatures. Indeed, experimental DIC images have shown similar flattening on a smaller scale at a lower solar flux, thereby proving the algorithm's ability to simulate a real phenomenon.

Abaqus has a proven track record of accurately simulating similar buckling of thin-shell structures in previous lab investigations [20][51]; all of this evidence makes it

the perfect candidate for accurately predicting thermally induced deflections.

5.3 Slew Simulations

Having demonstrated the reliability and superior ability of the Abaqus-Thermal Desktop process, we can now apply the method to simulate a spacecraft maneuver involving thermal and dynamic transients: a slew maneuver of the type projected to be used by space solar power satellites.

Motivation

To understand the characteristics of and rationale behind such a maneuver, a brief background is necessary.

Caltech's Space Solar Power Project (SSPP), a collaboration between three research groups, has the ambitious goal of developing and scaling the technologies necessary to generate solar power in-orbit and beam it to the ground. Such a technology would provide almost uninterrupted solar power day and night, adding an entirely new profile to the mix of renewable energies needed to combat global warming [45]. (Power generation for future Moon and Mars missions are additional applications.)

The current envisioned "unit" of such a solar power system is a large satellite covered in solar photovoltaics on one side and electronically steerable phased-array transmitters on the other, providing for power generation and transmission respectively. To provide power on the order of 1 MW, constellations of satellites would be coordinated, with the proposed size of the individual satellites being 60 meters square. Such large satellite dimensions demand both lightweight and deployable structures to meet the mass and volume requirements of current and projected launch vehicles. Therefore, ultralight and ultrathin solar cells, transmitters, and supporting structures are all necessary; these innovations are currently being investigated by the research groups of Profs. Harry Atwater, Ali Hajimiri, and Sergio Pellegrino, respectively [45]. In 2023, a prototype platform successfully demonstrated the feasibility of all three technologies in-orbit [11].

To ensure steady power transmission to the ground station and reduce the effects of Earth occulting the sun, SSPP satellites would reside in medium Earth orbit (MEO) or geostationary orbit (GEO). To maximize power generation (i.e. to keep the sun shining on the photovoltaic side of the satellite, and keep the transmitter side pointing in the general direction of Earth) the satellite must rotate continuously during its orbit, as found by Michael Marshall and Ashish Goel [26]. The rate of

these rotations can either be slow enough to be considered quasi-static (e.g. rotating 90° over ten hours), or rapid enough that dynamic effects may need to be considered (e.g. rotating 90° over ten minutes); this latter case is called a "slew maneuver" in this work.

Even the stiffest utralight and ultrathin deployable structures, when extended to 60 meters across, undergo a decrease in rigidity from geometrical factors alone; this means that such structures cannot be modeled as rigid during sufficiently fast maneuvers, which has been the standard modeling technique of almost all spacecraft missions to date. In response, Dr. Michael Marshall dedicated his thesis to investigating and modeling such large flexible spacecraft dynamics during slew maneuvers; finding that current guidelines for the maximum slew rate of flexible spacecraft were exceedingly conservative, he validated the feasibility of the proposed slew maneuvers [25].

The result of all these considerations is this: even ignoring the flexible dynamic response caused by the maneuver itself, proposed slew maneuvers for space solar power satellites involve rapid changes in incident sunlight and resulting thermally induced deflections. To ensure the reliability of such satellites during these maneuvers, the transient thermal fields and loadings must be simulated, and the resulting contribution to the deflection response must be accurately predicted.

This means that, for tractability, the flexible-body dynamics of the slew maneuver are ignored for this thermal-structural analysis. An equivalent situation to the simulation exhibited would be as if the structure were fixed in space and the sun were rotated around the structure; the structure would react with transient temperature fields and dynamic deflection responses, but would not experience the inertial effects of a real satellite maneuver.

This section details how such a slew maneuver simulation was achieved. First, the effects of varying incident angles of sunlight under quasi-static conditions were simulated, offering a more nuanced understanding of the effects of self-shadowing and structural orientation in our particular architecture. Second, the necessity of the three defining characteristics of these slew simulations—thermal transient analyses, dynamic deflection analyses, and selection of two-meter structures—is justified with preliminary simulations. Third, the modifications to the Abaqus-Thermal Desktop code that were required to couple the transient thermal and dynamic simulations needed, as well as ensure that loading remained smooth despite larger step sizes, are explained. Finally, the results of such simulations are examined.

The orbital parameters used throughout this section are as follows. In Thermal Desktop, structures were placed at an orbital height of 20,184 km (i.e. MEO) and an orbital "position" of -90 degrees, with the longerons aligned with Polaris and the battens aligned with the nadir; this created a heating situation with the sun, Earth, and space radiative background at right angles, anticipated to have the most aggressive thermal gradients. Solar flux was 1,354 W/m^2, while Planetshine and Albedo were both enabled in every analysis; background space radiative temperature was the Thermal Desktop default of 0 K.

Snapshots of Temperature Fields Under Varying Incident Angle

First, to get an intuition for the temperature fields present on the rotating spacecraft as a function of the sun angle, steady-state simulations were conducted for a variety of relative sun angles; these represent the temperature and deflection fields that would be present on the spacecraft when allowed to reach a steady state for at least 60 seconds, as shown in Section 5.3. Indeed, this is the heating case for the solar power satellite at every time *other* than during the slew maneuver, as the satellite rotates between ±45° relative to the sun over an 11-hour 50-minute period [26].

Therefore, this section's results characterize the portion of the SSPP satellite's orbit other than the slew maneuver, allowing for snapshots of temperature and deflection throughout the entire orbit. These simulations were carried out with the original composite laminates used in Chapters 2 and 3; for reasons described later, the remaining (dynamic) simulations were carried out with the graphite composite laminates described in Chapter 4.

Because SSPP satellite prototypes, including DOLCE, are constructed of strips at right angles to each other (see Figure 2.5), a rotation of the satellite about an axis parallel to one of them would result in two different types of strip rotation relative to the sun. For clarity, we will denote these relative sun rotations as "α" and "β" angles: strips whose longerons are aligned with the axis of satellite rotation would experience a changing α angle, while strips whose battens are aligned with the rotation axis would experience a change in β angle. See Figure 5.19 for an illustration. Both types of relative sun rotation exhibit different temperature field trends, and so are examined individually.

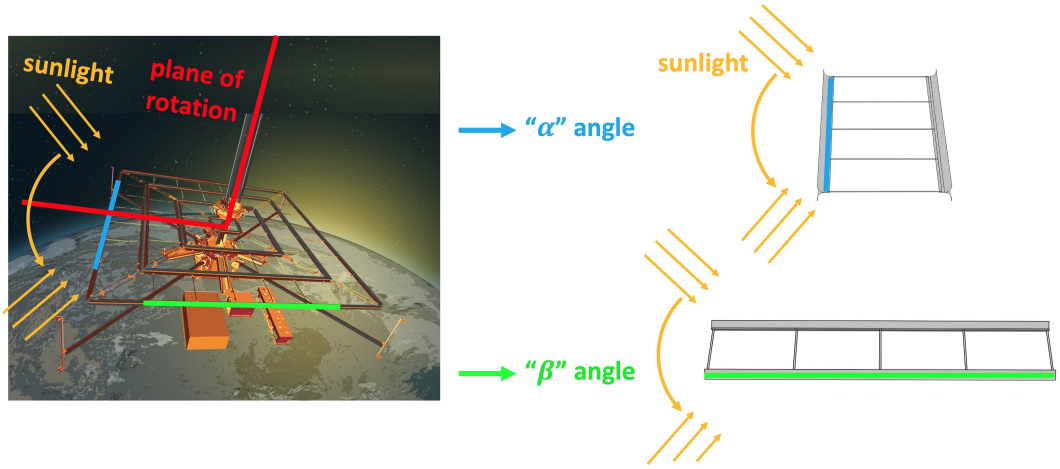

Figure 5.19: Definition of "α" and "β" sun angles during a satellite slew maneuver.

α Angle

A changing α angle results in solar heating that changes both in magnitude and distribution due to the longeron geometry. In addition, since the longeron cross-section is non-convex, some part of the longeron is always being shadowed by another part regardless of the value of the α angle; this "self-shadowing" causes sharp differences in heating across the longeron surface, which (as simulation results show) can cause abrupt deflection behaviors.

Figure 5.20 exhibits the structure under several steady-state α angle heating conditions; sunlight impinges on the structure from the right at the α angle specified from the horizontal. Note that the temperature plots are shown on the undeformed structures for easier comparison; the temperature fields themselves were calculated on the deformed structures as per the coupling looping outlined above. The plots are shown in a perspective view, looking down along the longerons for a more compact presentation.

Readily visible indicators of the changing heating are the temperatures of either the bottom longeron's right or top longeron's left flange tip; as the sun angle increases, the tip steadily heats, with the exception of the last frame. At an α angle of 90°, the bottom longeron is entirely shadowed by the top, causing a sudden plunge in temperature. This effect can be seen to initiate at an α angle of 87°, as shown by the extreme temperature gradients (>90°C) on the bottom longeron's left flange.

For some of these angles, a steady-state was difficult to converge upon or inconsistent; for example, the case for an α angle of 45°, during the first set of steady-state runs,

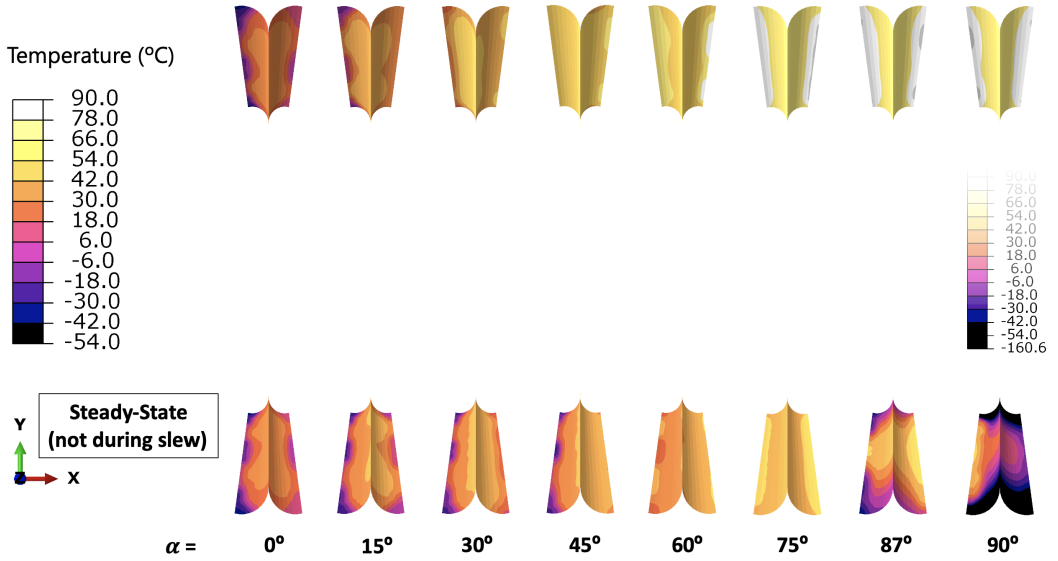

Figure 5.20: Steady-state temperature fields for a changing "α" sun angle, as viewed looking down the structure. The 90° case has the same temperature scale but with a lower minimum.

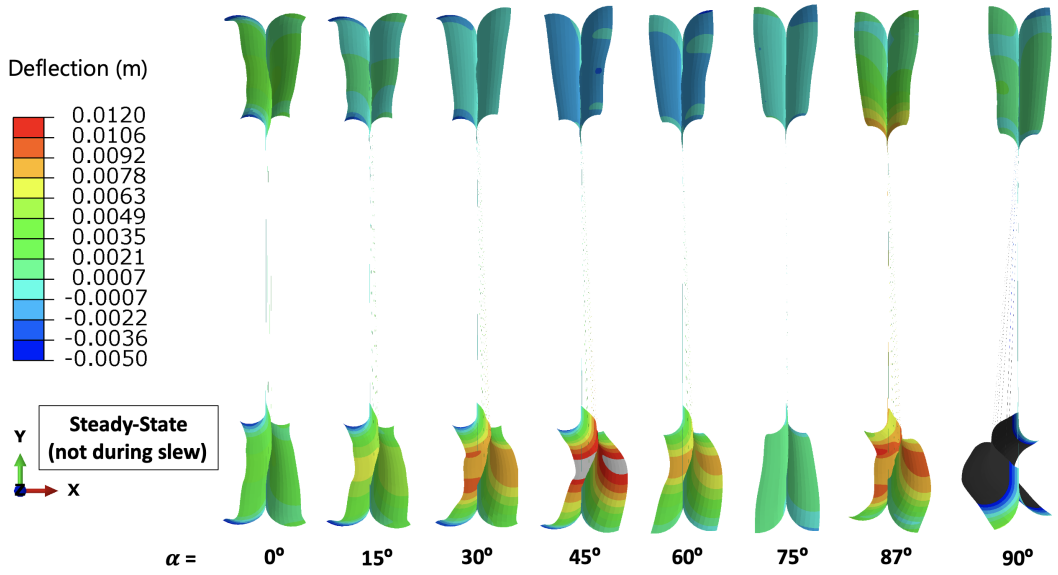

Figure 5.21: Steady-state out-of-plane deflection fields for a changing "α" sun angle, as viewed looking down the structure.

ended after several loops on the heavily-deformed but unbuckled configuration shown in Figure 5.21; however, when the same model was re-ran to provide an initial steady-state configuration for the later dynamic analyses, the model converged on the buckling configuration shown in Figures 5.29 and 5.30.

In addition, a true steady-state was difficult to find with 87°, since the heating of the flange edge would cause strong enough thermal expansions to flatten the flange; this then would take the flange edge into the shadowed region and cool it off, which in turn would un-flatten the flange and make part of it enter the heated region again on the next step. A similar situation occurred near the onset of self-shadowing at α = 82.2°; when the shadow first fell on the edge of the bottom flange (with the rest of the longeron still being sunlit), the cooling of those elements would cause a sideways contraction that would bend the flange edge out of the shadow. On the next timestep, the flange edge would warm from the sunlight, causing it to expand and bend back into the self-shadow. See Figure 5.22 for an illustration.

These situations can be considered points of thermal instability, with the solar load and step "inertia" driving an unstable response. The instability unfortunately implies that an accurate resolution of the thermal field on the "fluttering" flange would have to involve a timestep shorter than the vibration period, i.e. tenths of a second or less. Adaptive timestepping would therefore be necessary at this scale, since maintaining such a small timestep for the entire slew maneuver would take orders of magnitude longer to compute.

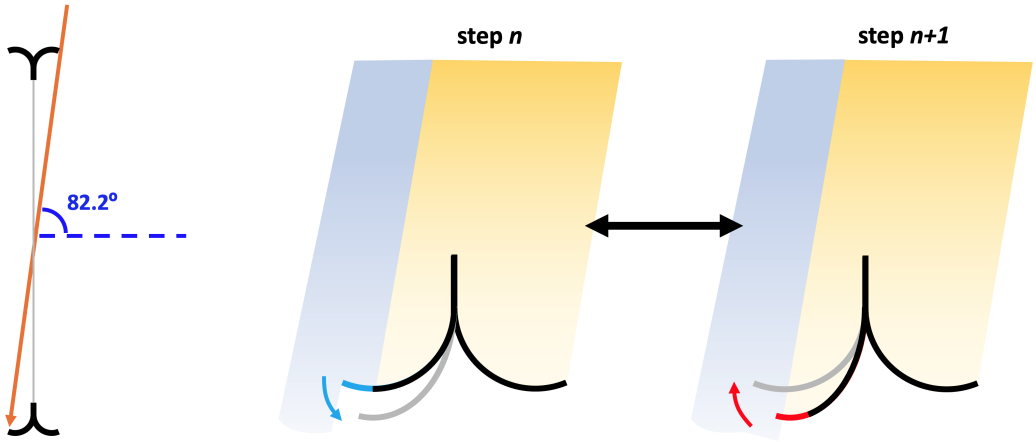

Figure 5.22: A diagram showing the difficulty of resolving self-shadowing effects with timesteps on the order of several seconds.

Looking at the displacements, the structural deflections for the same angles tell a similar story, as shown in Figure 5.21. These deformed snapshots for the same heating conditions show the largest amount of deflection for 45° and 90° of α angle. Both maxima reflect large differences in temperature gradients: the 45° case appears to have the largest differences diagonally between top and bottom flanges, while the

90° case simply has an enormous absolute difference between the top and bottom longerons as a whole. In addition, the rapid shift in deflection direction between 87° and 90° is notable: the structure encounters two extreme deflections in different directions in the span of only 8°. The effect of this swing on dynamic deflection is in fact observed in the dynamic analyses presented later.

β Angle

Changing the β angle, as shown in Figure 5.23, has much more gentle consequences. As the structure rotates about a batten axis, self-shadowing changes very little, and is almost negligible to begin with: only the very edge of the flanges are shadowed, and the flange ends are the only places where such shadowing changes with rotation. As such, the net effect of a changing β angle is to uniformly reduce the heating across the entire structure, with the magnitude scaling as the cosine of β.

This analysis explains two main takeaways from Figure 5.23. First, the visible heating profile across all β angles remains symmetric, almost unchanged except in magnitude; second, this magnitude decreases slowly before 45° and quickly afterwards, matching the behavior of a cosine.

The deflections of the β angle sweep tell the same story, as shown in Figure 5.24: a similar-looking deflection field is slowly scaled to zero deflection in the manner of a cosine.

Justifications for Critical Simulation Choices

The three main factors making these slew simulations unique (and unprecedented in scope) require three justifications: 1) why the thermal simulations must be transient, 2) why the deflection simulations must be dynamic, and 3) why 2-m structures are an adequate test case to study the behavior of larger structures.

Thermal Transients

As seen in the previous section, self-shadowing effects are significant in our structures due to the unavoidable geometric overlapping of concave flanges. Since the structures are made of webs and flanges of finite size, these shadows abruptly start and stop as the incident solar angle (i.e. α) changes, effectively causing highly nonlinear step heat loads on the shadowed/unshadowed elements.

The response of the structure to an applied step heat load can be determined by suddenly changing the incident solar angle and examining how the transient temperature

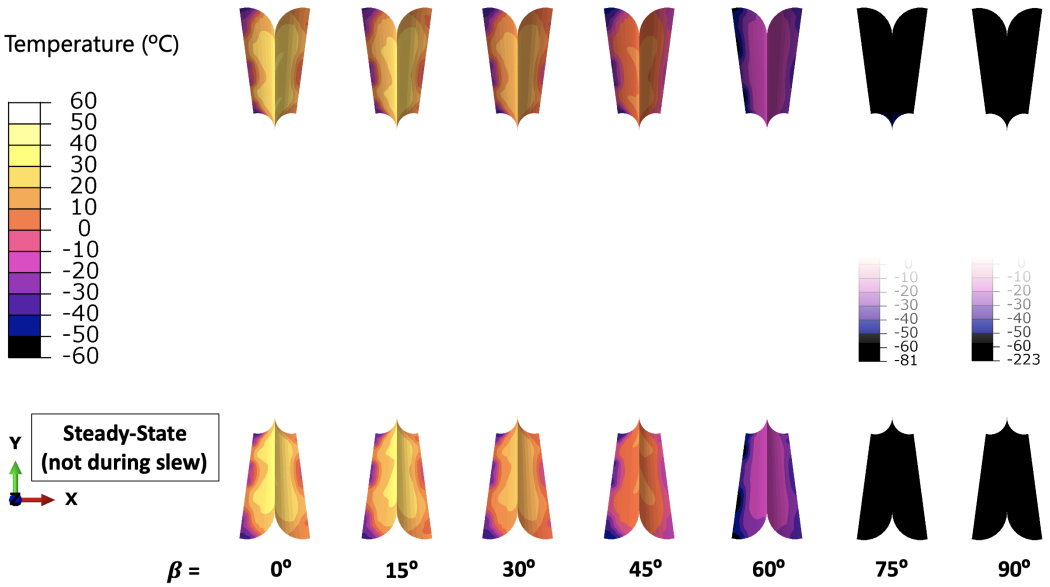

Figure 5.23: Steady-state temperature fields for a changing "β" sun angle, as viewed looking down the structure.

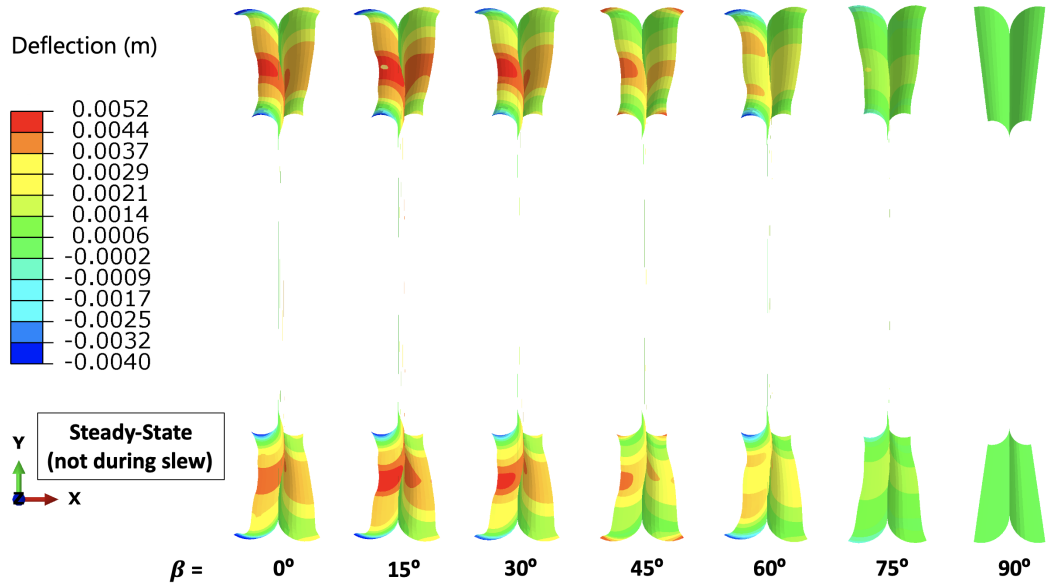

Figure 5.24: Steady-state out-of-plane deflection fields for a changing "β" sun angle, as viewed looking down the structure. 75° and 90° cases have an expanded scale.

fields evolve. A simulation was therefore designed to accomplish this step-loading transient response; it has two main steps. The first is a quasi-static initial step (Abaqus "Static, General") which brings the structure from an unstressed room temperature state to the equilibrium deflected state at an incident sun angle of $\alpha = 0°$, achieved

by applying the Thermal Desktop steady-state temperature field for $\alpha = 0°$ as a predefined temperature field. The second is a dynamic (Abaqus "Dynamic, Implicit") step, with the predefined temperature loading abruptly switched to the Thermal Desktop steady-state temperature field for $\alpha = 30°$. β is set to $0°$ in both cases for simplicity.

The resulting transient temperature response for such step loading is shown in Figure 5.25; each line represents a nodal temperature over time. It takes at least 30 seconds for all nodal temperatures to be within several percent of the final steady-state values (at far right), and around 60 seconds for the two temperature fields to be visibly indistinguishable. In that amount of time during a slew maneuver, the structure would have rotated 4.5°- 9°, meaning the heating load would have significantly changed before the structure had equilibrated temperature to the previous heating load. This means that the time elapsed is a critical factor to predicting accurate temperatures, making transient temperature analyses necessary for rapid slew maneuvers.

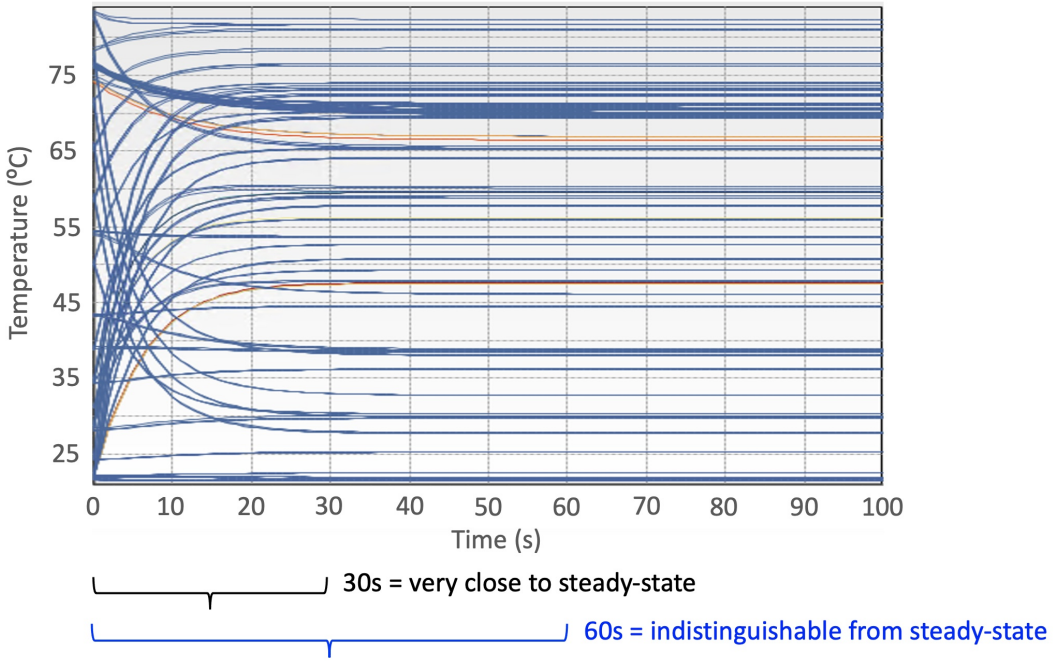

Figure 5.25: Randomly selected structure nodal temperature transients encountered when suddenly changing α angle from $0°$ to $30°$.

Dynamic Deflections

To determine whether dynamic simulations are appropriate, understanding the dynamic responses of our structures as a function of length is necessary; these dynamic

Table 5.1: Second-mode frequencies of various structural lengths.

	1 m	**2 m**	**5 m**	**10 m**
Longeron-bending mode (Hz)	21.5	12.2	2.79	0.68

characteristics can be encapsulated by calculating and examining the fundamental modes of each structural length. Accordingly, a linear perturbation analysis was run in Abaqus for 1 m, 2 m, 5 m, and 10 m structural lengths, yielding the fundamental modal frequencies and shapes depicted in Figure 5.26, as well as summarized in Table 5.1.

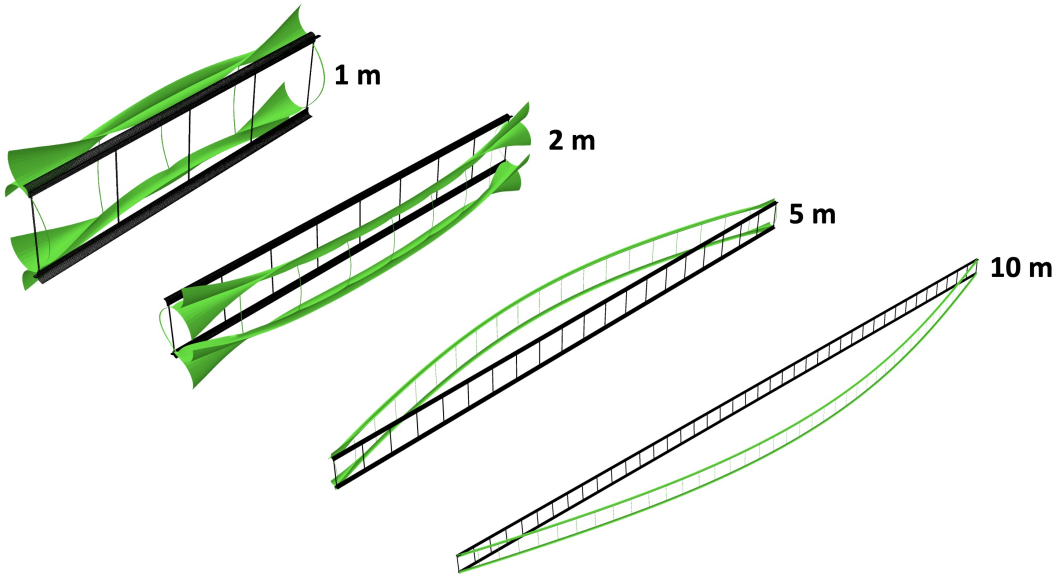

Figure 5.26: The second, i.e. "longeron-bending", mode for the 1 m, 2 m, 5 m, and 10 m structural lengths.

An important concept to understanding these modes lies in the relative flexibility of the two structural elements making up the structures: longerons and battens. These analyses reveal that for all structural lengths, including 10 m, the battens *as modeled* are more easily bent than the longerons; this means that the first mode for all structural lengths is a "batten-bending" mode, one where the battens bend in-plane and the longerons remain nearly straight.

The second mode for all structures is a "longeron-bending" mode, one where the longerons bend in the expected fundamental mode shape, and the battens bend out-of-plane in order to accommodate this; see Figure 5.26 for an illustration. Since the batten stiffness and connections can simply be tuned in future prototypes, our

analysis will focus on this second "longeron-bending" mode, which is in fact the main mode excited by the applied thermal loads.

According to Table 5.1, all the structures have a characteristic period (1/frequency) less than the time taken for the slew maneuver's heating to rotate even 1° (6.7 s), meaning that the argument used to justify thermal transients for our simulations does not always apply to dynamic ones. However, for larger and larger structures, this time period comparison is certainly beyond or on the cusp of needing to be accounted for; thus, in this work, dynamic deflections are calculated as a proof of concept, even if the simulation is not necessarily improved or changed by accounting for dynamics.

Chosen Structural Length

Examining the mode shapes of Figure 5.26, we can notice that among the second modes, there is a difference in the amount the longerons twist around their axis vs. bend out of plane. For 1 m, the longerons are barely able to bend over that short of a distance, meaning that they mostly twist twice throughout their length instead of bowing out of plane; for 2 m, 5 m, and 10 m, there is enough structural length for much out-of-plane deflection to occur. Therefore, this bowing characteristic of longer structures only occurs with sufficient length, and arguably starts dominantly occurring at a structural length of 2 m. Thus, 2 m appears to be the minimum length of structure that exhibits key characteristics of the dynamic deflection response of longer structures, and as such is the length of structure chosen here to perform the slew simulation.

Workflow and Modifications for Coupling Thermal Transient and Dynamic Deflection Simulations

The basic workflow presented earlier for coordinating Abaqus deflection analyses and Thermal Desktop thermal analyses had to be significantly modified to accommodate both dynamic and transient versions; it also had to account for a structure that did not begin at the typical initially unstressed state.

The proposed slew maneuver begins with the structure already at thermal equilibrium (and a resulting steady-state of deflection) at an incident solar angle (α or β) of 45°. Therefore, to start the slew simulation, a regular quasi-static coupled analysis is run according to the basic workflow described earlier. The Thermal Desktop orbital heating case, with the usual equatorial orbit with an altitude of 20,184 km (MEO),

is specified as the structure having a α or β of -45° and a orbital position of -90° (i.e. 3 o'clock looking down at the North Pole, 12 o'clock pointing toward the Sun).

Once this initial step has converged, the slew maneuver simulation is initialized by ensuring the Abaqus model refers to the result of the quasi-static simulation as an initial state predefined field, then changing the *Static, General step to a Dynamic, Implicit step. Thermal Desktop is similarly initialized by changing the steady-state analysis to a transient one using the result of the steady-state analysis as an initial state; in addition, the steady-state displacements of the prior analysis are carefully preserved in the new transient file to ensure accurate starting geometry for the thermal model. Figure 5.27 summarizes the changes.

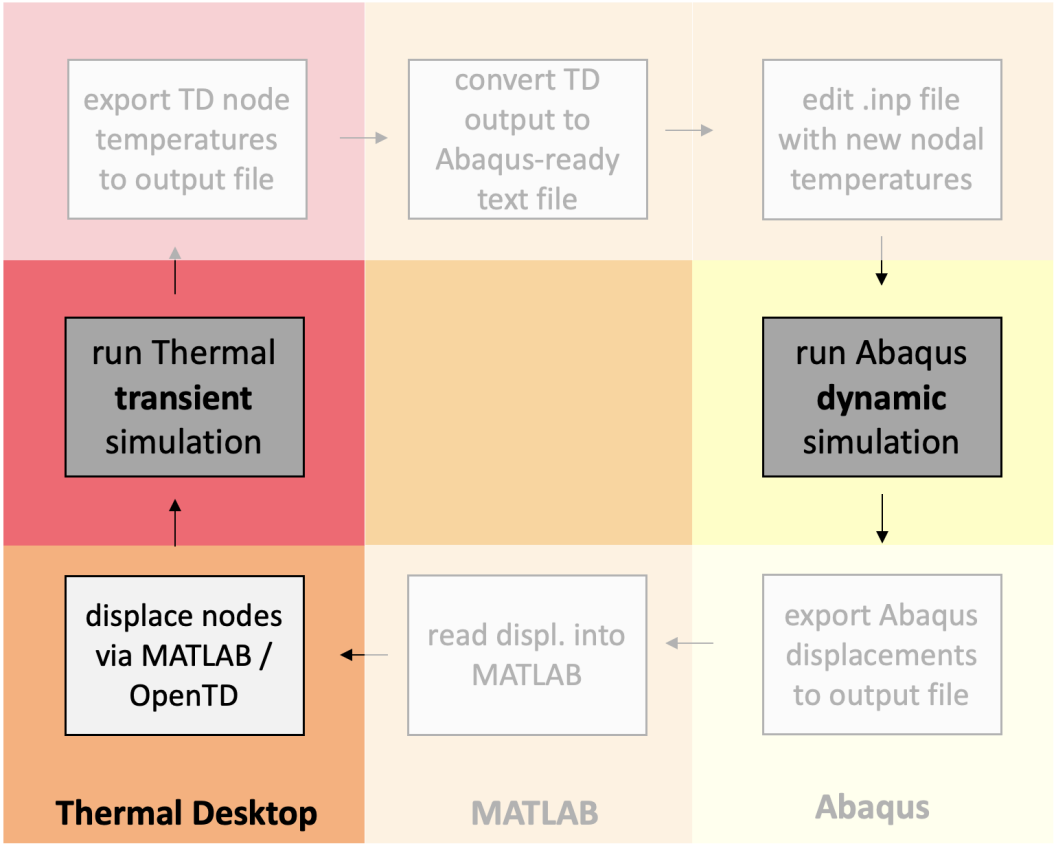

Figure 5.27: The Abaqus-Thermal Desktop coupling loop modified to couple dynamic deflections and thermal transients.

With these initializations carefully made, the MATLAB script then runs, coupling the two analyses in the manner of the basic workflow described earlier, with one major exception: the structure is rotated in the orbital heating case every loop according to the elapsed time step.

For the results presented here, the 10-minute 90° maneuver was split into 60 steps of 10 seconds each, meaning that the solar heating and structural view factors were recalculated every 1.5° of structural rotation. These changes to the orbital heating were executed in the MATLAB script using additional OpenTD commands. Therefore, an example loop ran in the following order: first, the orbital heating environment was rotated by 1.5°; the Thermal Desktop transient simulation then recalculated the new view factors and heating and ran for 10 seconds. The nodal temperatures were then passed by the MATLAB script to the Abaqus model, which ran a Dynamic, Implicit step for 10 seconds using these temperatures as a predefined field. The resulting deflections were then passed to the MATLAB script and used to adjust the Thermal Desktop model nodes. See Figure 5.28 for a diagram outlining these steps.

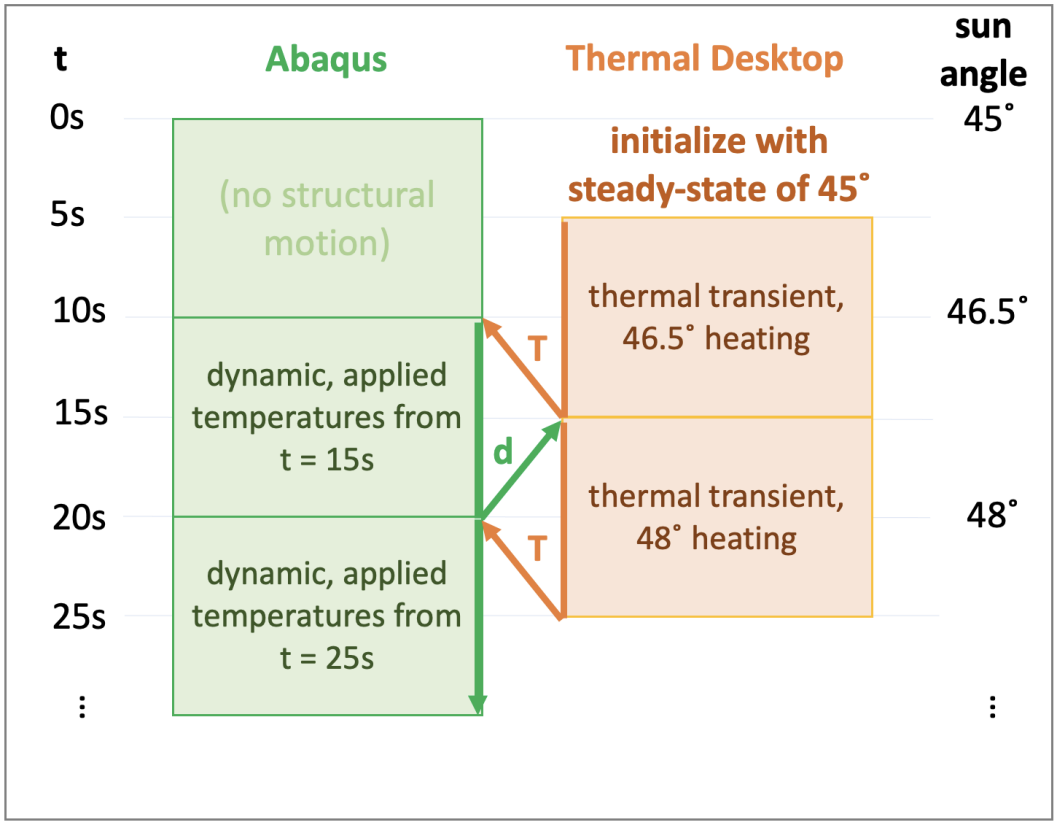

Figure 5.28: An example of the modified Abaqus-Thermal Desktop loop, "unfolded" for 2.5 loops for clarity.

It is important to note that, due to the relatively large timesteps involved (10 s), deciding when to apply the temperatures of one time step to the dynamic model is nontrivial. Temperatures arising from a sun angle of 10°, for example, could be

applied to the dynamic model at a time corresponding to a solar angle of 8.5° or 10° depending on whether the dynamic model should be purely reactive or slightly anticipatory of future temperatures. Since this choice, in the end, only time-shifts the dynamic results by a maximum of one time step (here, 10 s), it does not actually make too large of a difference to the final result.

There is an interesting side effect of applying each new temperature load at the beginning of each dynamic step; each temperature load being a suddenly applied step load, the structure reacts by violently vibrating at near its fundamental frequency. This shaking only continues for a few seconds due to numerical or thermoelastic damping, but it points out a serious problem in applying a continuously changing thermal load in such a discrete manner. This problem was solved by specifying the restarted *Dynamic, Implicit step to "ramp" up to the newly applied temperature field from the previous step's temperature field via linear interpolation; as Abaqus field variables do not work for linearly interpolating predefined temperature fields, the "AMPLITUDE=RAMP" option was used in the *STEP definition parameters.

Slew Simulation Results

The first result of note is that for the 2-m structure, when using the composite laminate material properties listed in Table 2.1, the linear deflection analysis failed to converge (i.e. yield a result) under 1354 W/m^2 sunlight with an an incident solar α angle of 45°. As shown in the steady-state deflections of Section 5.3, this α angle represents a local maximum of deflection magnitude; furthermore, the temperatures encountered were sufficient to expand the flange of one longeron so much that it buckled. Figures 5.29 and 5.30 illustrate this phenomenon; in particular, Figure 5.30 demonstrates the presence of compressive stresses, especially at the base of the longeron flange. In addition, nonlinear analyses were attempted, and negative structural eigenvalues were encountered; these two facts confirmed that buckling had in fact taken place. Further information on such buckling can be found in Appendix B.

A steady state was therefore impossible to find for our typical composite laminates under realistic orbital heating. This means that, if future SSPP prototypes are to keep the same structural framework, solutions must be implemented for thermal control.

The solution presented here, and one detailed in Chapter 4, is adding a 12-μm layer of graphitized polymer to the standard composite layup, dramatically increasing the thermal conductivity and reducing thermal gradients. See Figure 5.29 for a

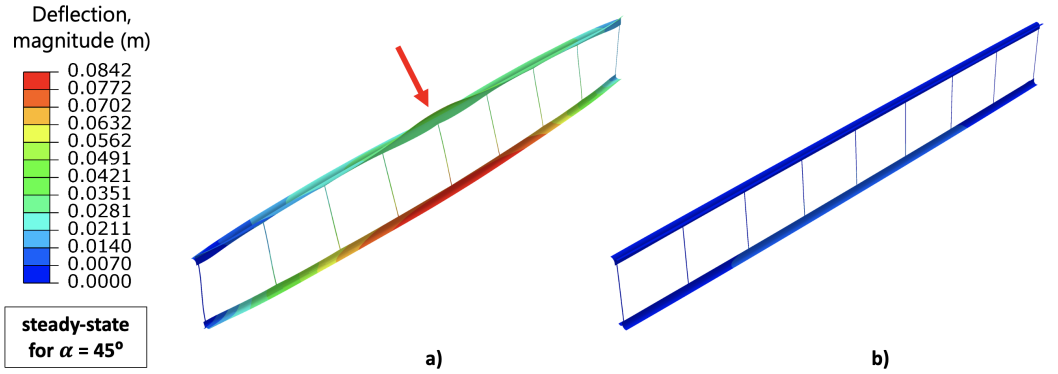

Figure 5.29: "Steady" states of the a) original composite laminate, and b) layup with graphitized polymer layer. The buckle formation of the original laminate (red arrow) precluded its use in the final slew maneuver simulation.

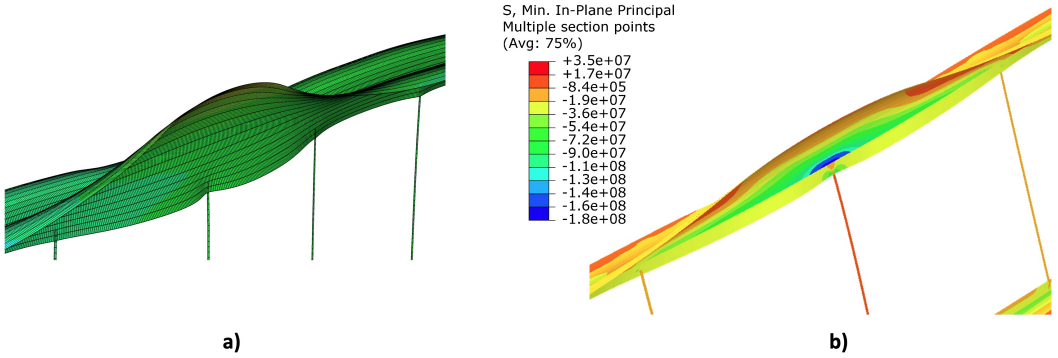

Figure 5.30: a) A zoom of the buckle shown in Figure 5.29 a), with b) the plotted in-plane principal stress showing compression occurring.

comparison of the steady-states of the original laminate (as used in Chapters 2 and 3) and the graphite laminate used from the next section onward; the deflections of the graphite laminate are about an order of magnitude less. Furthermore, since the original structure's bottom longeron is able to bend without buckling to a deflection of 8.4 cm (see Figure 5.29 a)), that implies that the graphite structure (with a deflection of around 7 mm) has at least a factor of 10 "margin" to not buckle in the same $\alpha = 45°$ position.

Therefore, to focus on the thermal and dynamic characteristics of the slew maneuver, and to not be concerned with any potential structural buckling, the 2-m structure simulation results from this point forward were specified to have a laminate with a graphite layer of the type described in Chapter 4, Sections 4.2, 4.3, and 4.4—that is, the same composite laminate, but with a 12-μm layer of graphite polymer on the

concave side of the flanges and on both sides of the web.

Transient Temperature Fields During Slews

Figures 5.31 and 5.32 illustrate snapshots of the transient temperature fields during the ten-minute maneuver, for both α and β angles on the structure respectively.

For α angles, the contribution of the transient analysis is apparent when compared with the steady-state results. Due to the mild thermal inertia of the structure, 93° represents the temperature field during which the structure "crosses over" from positive to negative deflection in the middle of the maneuver, just after it has passed through maximum self-shadowing. The onset of this self-shadowing occurs after 82.5°; this is evidenced by the band of colder temperatures on the bottom left flange that first appears for the 85° heating condition.

For β angles, the gentler trend noticed in steady-state simulations continues in the dynamic maneuver simulation. Due to the heavy amount of radiative cooling that occurs during the middle of the maneuver in the absence of impinging sunlight, the minimum temperatures were shown to occur at a β angle of 99°, past the halfway point of 90° due to thermal inertia. Other than this, the temperature fields are almost entirely symmetric about the 90° condition.

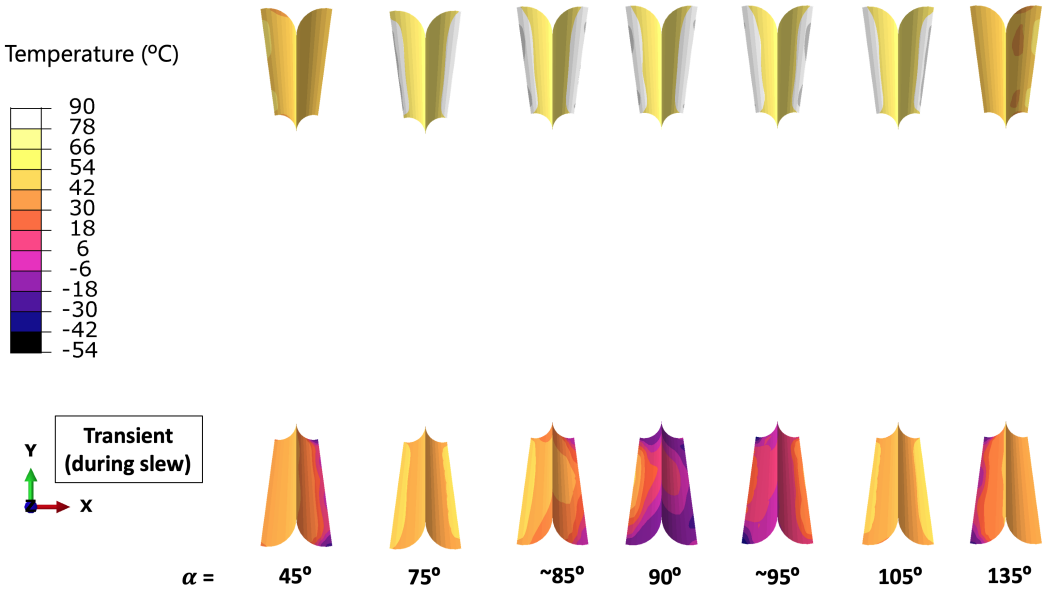

Figure 5.31: Transient temperature fields during a slew maneuver for a changing α sun angle, as viewed looking down the structure.

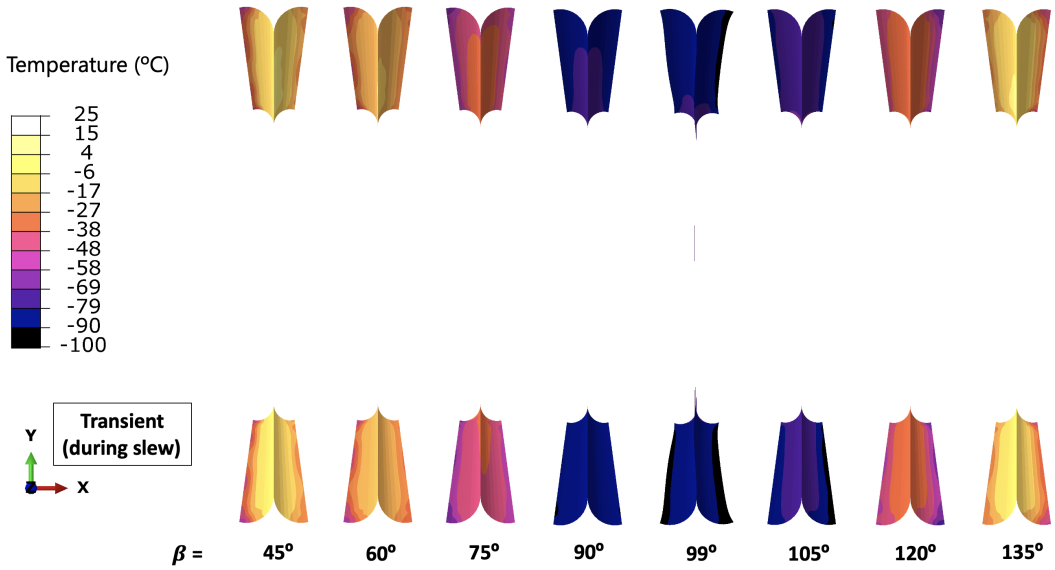

Figure 5.32: Transient temperature fields during a slew maneuver for a changing β sun angle, as viewed looking down the structure.

Dynamic Deflection Fields during Slews

The general dynamic behavior of the structure can be visualized by following the trajectory of a point on the top longeron and a point on the bottom longeron over time; these are shown in Figure 5.33 for the α angle case. This figure juxtaposes the deflection vs. time point graph with snapshots of the longeron at each position; the blue circle marks the point where the deflection is being measured. At first, deflections increase slightly, then taper to almost zero (e.g. α = 75°) until around 250 seconds in; at 85°, encountering the self-shadowing described previously, the deflection sharply increases (first green arrow) and remains there through the halfway point. When part of the bottom longeron emerges from shadow, the deflection rapidly swings to the other extreme (second green arrow), then quickly decreases in magnitude as the bottom longeron becomes more evenly heated. The structure then slowly approaches a local maximum of deflection before arriving at the 135° endpoint, the equivalent of the 45° case from the other direction. Indeed, the entire deflection vs. time curve can be viewed as an anti-symmetric deflection response to a symmetric heating load, but slightly offset and altered by the lag induced by thermal inertia.

The equivalent deflection vs. time graph for the β angle case is much less dramatic, as shown in Figure 5.34: the deflections gracefully transition from one extreme to the other due to the graceful heating described earlier. The deflections involved are

also much less than the α angle case, by a factor of up to 3.

Figures 5.35 and 5.36 illustrate snapshots of dynamic deflections corresponding to the temperature fields of Figures 5.31 and 5.32. These offer a more nuanced insight into the overall deflections of the longerons; readily observable is the much larger deflections of the bottom longeron as compared with the top one in the α angle case. Note that, in the α angle case, deflection fields similar to those shown in the 85° snapshot occur just after the 93° point, but in the other direction, as seen in the 95° snapshot.

The β angle case tells a similar story to the point deflection plot, showing the graceful and uniform progression of deflection from one extreme to the other.

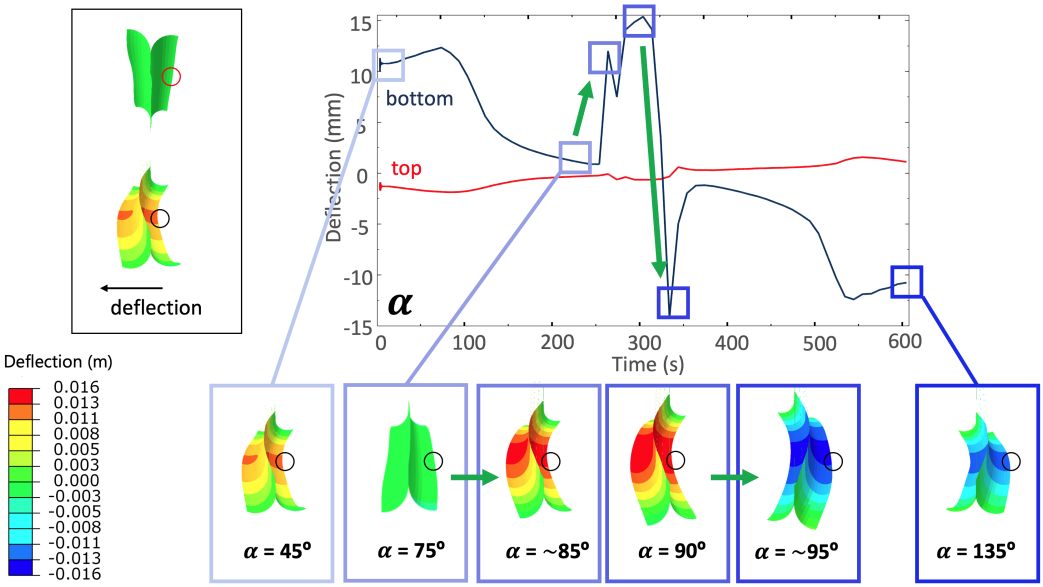

Figure 5.33: The deflection vs. time of two points on the sunward side of the structure under α angle heating during an α angle slew maneuver.

Decreased Time-Step Results

The sudden jump in bottom longeron deflection, shown just before α = 85° in Figure 5.33, partially results from the step size being 10 seconds; this duration is rather large compared to the speed at which self-shadowing moves across the bottom flange. Without going so far as to extensively modify the code to adaptively decrease the timestep in response to such large changes in heating, a smaller step size of 5 seconds was attempted to see if it improved simulation ability.

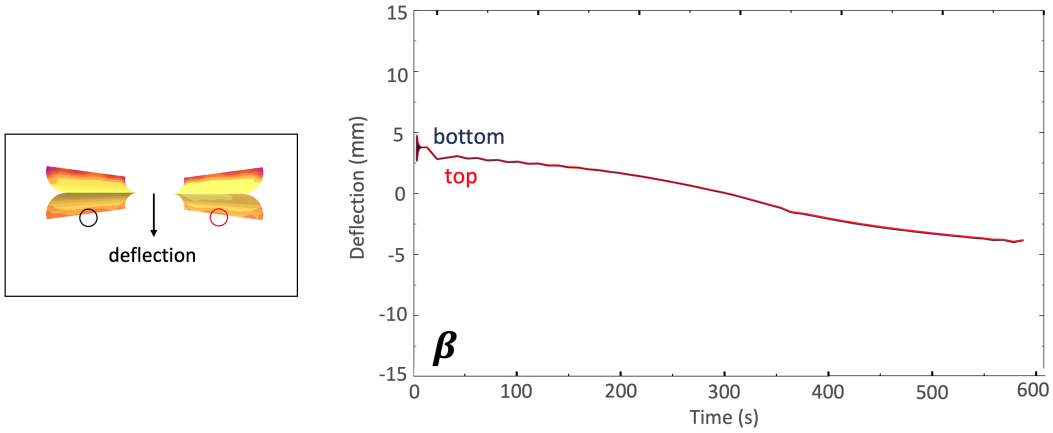

Figure 5.34: The deflection vs time of two points on the sunward side of the structure under β angle heating during an β angle slew maneuver.

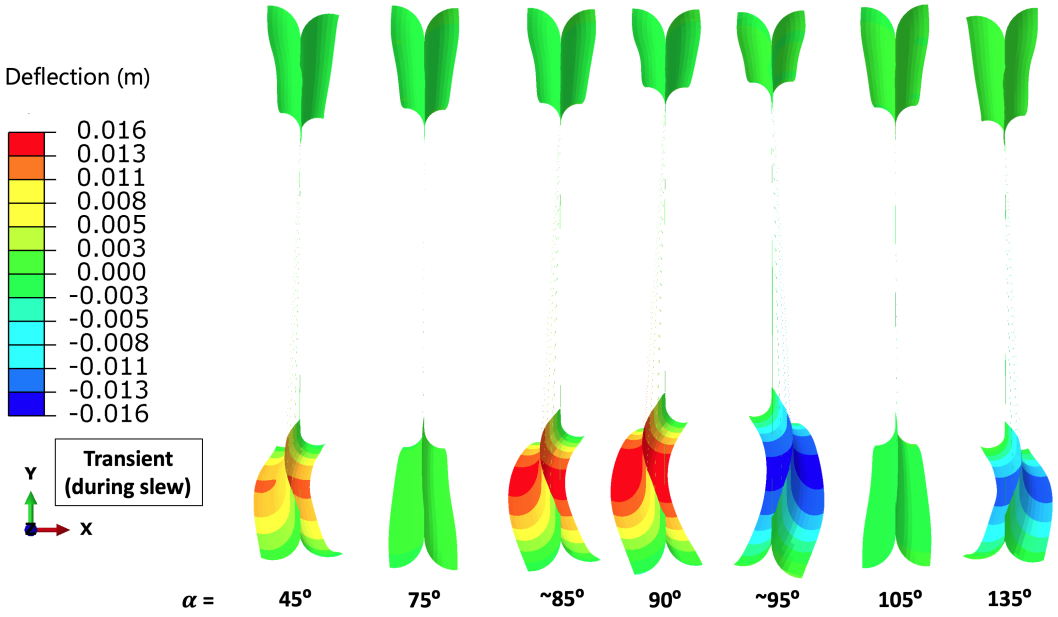

Figure 5.35: Dynamic out-of-plane deflection fields during a slew maneuver for a changing α sun angle, as viewed looking down the structure.

The partial results generated by this decreased timestep are shown in Figure 5.37. The simulated deflection is in fact smoother, but still struggles at the same self-shadowing onset angle around $\alpha = 82.5°$; indeed, the simulation failed to converge on a thermal solution at that very point.

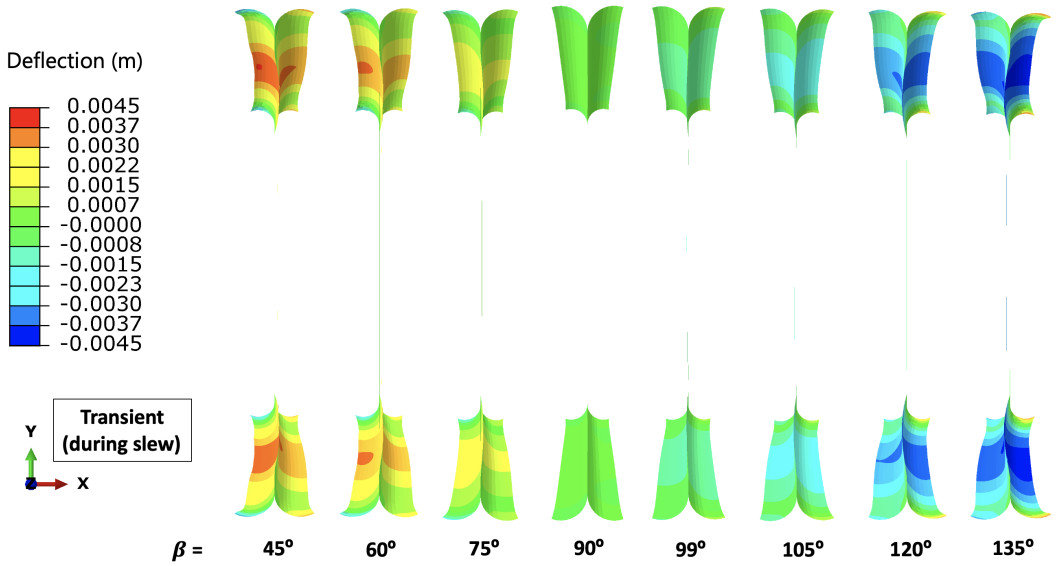

Figure 5.36: Dynamic out-of-plane deflection fields during a slew maneuver for a changing β sun angle, as viewed looking down the structure.

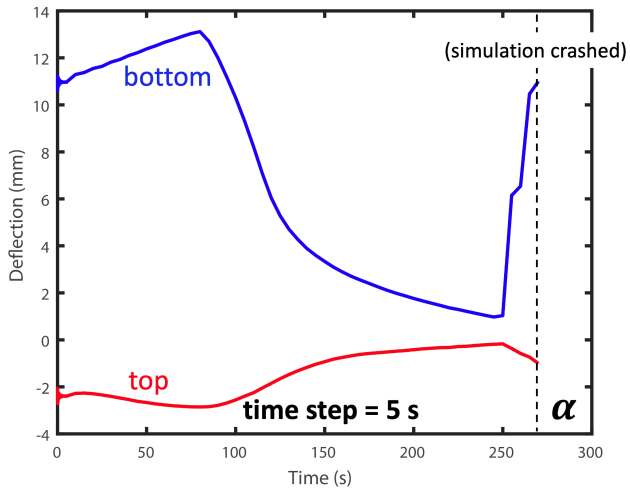

Figure 5.37: Partial results of the same dynamic simulation for α angle, using a shorter timestep of 5 seconds.

5.4 Discussion

There are a few key takeaways from the slew maneuver simulations presented in this chapter—the first being that self-shadowing by a slewing structure has a dramatic and sudden effect on temperature fields and subsequent deflections. In fact, the temperature gradients on even the steady-state angles are sufficient to buckle a two-meter structure built with the laminates tested experimentally in Chapter 2. Luckily, however, the deflections for structures with graphite layers are relatively small—only

about 15 mm, or less than 1% of the longeron length. However, such a deflection, applied suddenly, would almost certainly vibrate the spacecraft in an undesirable way, and thus would need to be accounted for in mission operations.

In addition, by comparison with the buckling results of the original laminate shown in Figure 5.29, we can roughly estimate how far the graphite structure is away from buckling. (This is not a perfect comparison, since the longerons are not bending in isolation, and the flux vs. deflection curve would also not be linear.) Since the original structure's (bottom) longeron is known to be able to deflect 8.4 cm out-of-plane without buckling, that implies that the maximum deflection seen in the graphite longerons, or 1.5 cm, is less than a fifth of the way there. Taken with a grain of salt due to the clear nonlinearity involved, such a measure could be useful in future structural analyses as a parameter to compare different designs.

Chapter 6

CONCLUSIONS

The individual components of this thesis, while dealing with topics as diverse as convection simulation to composite material implementation, combine to advance current techniques for understanding thermal deflections of thin structures on several fronts. Past and current limitations on the study of these potentially mission-critical structural effects have hampered efforts to control and eliminate them, making a fresh set of techniques sorely needed; it is my hope that this work demonstrates such a set, aiding forays into future solutions.

6.1 Summary and Contributions

The overarching narrative arc defining this work is this: to measure, predict, and reduce thermal deflections on thin-shell composite space structures, and use this knowledge to make unprecedented predictions of structural behavior during a satellite maneuver involving realistic orbital heating.

In Chapter 2, to directly measure thermally-induced deformations in the laboratory, as well as provide a ground truth by which to compare future simulation results, a remarkably unique experimental setup was devised. Emphasizing visibility in both the visible and infrared spectrum, the transparent acrylic chamber used allowed for full-field measurements of temperatures and deflections across the entire test structure – a complete departure from the typical thermal vacuum chamber's lack of sizeable viewports and camera compatibility. Despite the trade-off incurred by accepting non-negligible convection, such a setup allowed for the acquisition of a baseline of repeatable temperature and deflection results across multiple trials and samples; due to the lack of consumables use and shortened trial time, this was done at a fraction of the cost of even a *single* professional thermal vacuum chamber experiment.

Chapter 3 presented advanced multiphysics models of the experimental chamber and structure, showing that a combination of 3D modeling (radiation, conduction, shell solid mechanics) and 2D modeling (radiation, convection) is sufficient to capture all the physical effects causing thermal deflections on the structures tested. While neither model was able to fully capture all effects, and thus be able to

produce the temperature fields needed for accurate deflection predictions, the models themselves (and future models iterated from them) provided the knowledge and direction needed for the advances of Chapters 4 and 5. The convection modeling in particular, however, provided compelling evidence that, due to the modeling difficulty and large temperature effects created on the structure, convection should be avoided at all costs for future attempts at reproducing deflections of thin-shell structures in simulation.

In Chapter 4, a means of lowering thermal gradients (and therefore deflections) was simulated, implemented into test structures, and verified experimentally: graphitized polymer film. An extension of the COMSOL model of Chapter 3, when modified to include the thermal properties of such a graphite layer, predicted much lower thermal gradients and over an order-of-magnitude lower deflections. A sample manufactured to incorporate this layer was then shown to experience 4-10 times less deflection than the experimental baseline of Chapter 2. This rapid and simple progression from idea to prototyped verification offered direct experimental evidence that such a materials-based intervention works to reduce and almost eliminate thermal deflections on real structures. Furthermore, the nature of this graphite solution has many practical advantages that make it readily integrable into future composite space structures; most notably, its 12 μm thickness does not noticeably affect laminate or structural stiffness properties. In addition, the mechanism by which graphite reduces deflections works regardless of incident solar direction or structural geometry, making its application very flexible.

The tools gained from these previous endeavors culminated in the work of Chapter 5, a successful modeling of thermal effects during a satellite slew maneuver with a near-unprecedented recalculation of radiation view factors on a realistically-sized structure. The limitations of COMSOL modeling in accounting for deflection-induced heating changes are explained through example simulations, showing that progress in such simulations required different software. A coupled simulation technique involving passing temperature and deflection results between two finite-element solvers, first pioneered by Dr. Olive Stohlman for cylindrical booms, was therefore extended to model multi-component structures of arbitrary complexity. This achieved, a full study of the temperatures and deflections experienced during the orbital trajectory and maneuvers of an SSPP satellite was undertaken; both steady-state and transient results were obtained by modifying the underlying coupling loop, giving a full picture of structural behavior.

Most importantly, it was shown that attempting an $\alpha = 45^\circ$ steady-state heating of the original composite laminate 2-m structure results in longeron buckling; such behavior would seriously hinder or even jeopardize a mission incorporating such structures, and thus must be seriously addressed. It is then shown that adding a graphite layer to the structural material eliminates this buckling possibility, further lending support to its inclusion on future space missions. In addition, the simulations of Chapter 5 demonstrated that self-shadowing in such thin structures produces sudden and large temperature gradients, causing corresponding jumps in structural deflections that are mandatory to consider for any such slew maneuvers.

6.2 Future Work

In these forays, several avenues for future work were opened up, allowing for additional progress and advancements to be made.

Experimental Improvements

Future experiments could be improved by several different approaches, depending on which aspects of testing are desired to be emphasized.

The most obvious way to improve the experiments in this work would be to eliminate convection. Such an action could be achieved through better chambers and/or better roughing pumps, and many irregularities and simulation correlations would doubtless be improved by doing so.

If convection reduction is impossible, positioning the chamber such that convective air currents do not impinge on the structure might ameliorate undesired and unpredictable structural cooling. Since the lamp heat plume travels upward while the cold plate downdraft travels downward, it may be possible to reduce convection currents in the chamber if the setup were modified to have the lamp reflector facing down and the cold plate resting at the chamber bottom (i.e. with the structure horizontal between the two). This would cause pooling of the hot and cold residual air at the top and bottom of the chamber, away from the structure, which might leave its temperature fields less affected. Figure 6.1 illustrates this effect in an example convection simulation of the chamber modified in this way.

A final experimental improvement would be to improve both the number and angle of the infrared cameras aimed at the structure during testing. Even with wide-angle lenses, a single thermal camera has difficulty capturing the entire structure, much less the various components in detail. The high quality and inexpensive nature

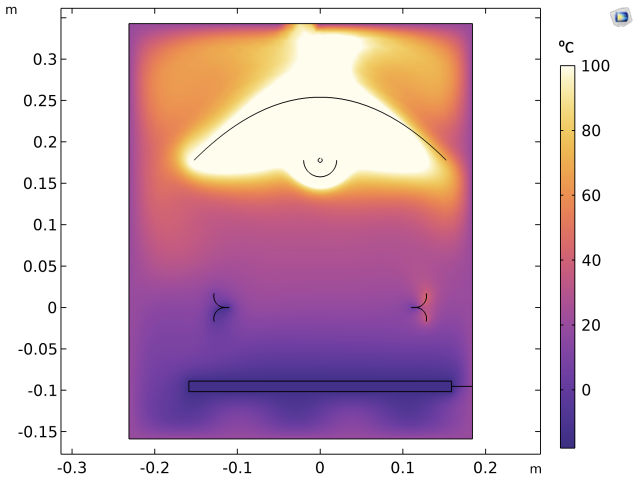

Figure 6.1: Steady-state temperature field of the 2D COMSOL model, simulating the chamber as effectively rotated by 90°.

of modern smartphone-compatible infrared cameras is unprecedented, and would allow several such cameras to record at various angles inside the chamber for a fraction of the cost of a typical thermal camera used for testing. This would allow for true full-field measurements of structural temperatures, allowing for fine-tuning of thermal models at a resolution far beyond what is currently available.

Graphite Film Implementation

The graphitized-polymer film used to dramatically increase our structures' thermal conductivity, while proven very successful in the prototype and instrumental in the feasibility of a realistic slew maneuver of a two-meter structure, is deserving of much further study.

While a 12-μm graphite film was chosen merely as the thinnest commercially available option, and thus the least likely to affect the well-characterized stiffness properties of the prototype structures' laminates, it is entirely possible that thicker layers of graphite could provide more benefit. With the low material strength of graphite, it is unlikely that increasing the thickness of the layer would significantly affect the stiffness of the laminate.

Indeed, as prototype and analyzed structures become larger (5-10 meter range and beyond), or have larger longeron dimensions, thicker layers of graphite film would have the ability to spread greater amounts of heat over longer distances in the structures; further testing of graphite performance at these various length and thickness scales would be a good start.

At the prototype level, integration into the lab's thin-ply composite layups was almost seamless. However, the graphite layer, being itself made of essentially layers of graphene, was found to almost prevent successful bonding of the batten due to surface flaking, as mentioned in Chapter 4. Therefore, future structures using an outer graphite layer would have to adjust their manufacturing procedures accordingly.

Slew Maneuver Simulations

While the slew maneuver simulations in this work push the boundaries of satellite thermal analysis, several immediate improvements could be made to extend its modeling capability to more realistic spacecraft simulations.

Extending the simulation to handle longer and larger structures would be the obvious first step; however, other improvements would have to be made to avoid excessively long simulation times. On a server running Windows 10 on 18 cores (Intel Xeon Gold 6354 3GHz CPU) with 1 Tb of RAM, the 2-m structural simulations performed for this work took approximately four days; for longer structures, the (uncompleted) simulation times were found to increase exponentially due to the increased time needed to calculate radiation view factors. Since such view factors are calculated for each element, and take into account the element's view factor toward every other element in the model, this exponential increase makes sense.

To combat such impractical simulation times, some radiation simplifications could readily be made; for example, applying a symmetry condition to split the length of the structure into two identical halves (from the perspective of incoming sunlight) might cut the simulation time in half, since the structures deformed almost completely symmetrically. In addition, mesh size was left unchanged at the maximum value required to ensure that any buckling behavior was captured. Since these analyses reveal exactly where in the slew maneuver deflections would be at their worst—and thus most likely to cause buckling—these points could be simulated in the steady-state with a finer mesh to ensure no buckling would occur, and then with a larger mesh for the actual dynamic maneuver simulation. Other schemes for mesh refinement studies of course exist, but this method would be an example of one that took advantage of the simulation's unique capabilities.

6.3 Closing

In conclusion: measuring, predicting, and eliminating thermal deflections on thin-shell composite structures requires careful testing, detailed simulations, and clever innovation; this thesis hopes to join the ranks of such works, pushing the limits of

space structures. Even though the "wings" of modern spacecraft have often been sensitive to sunlight like the wings of Icarus, with further investigations, the space structures of the future might not just match Icarus, but fly even higher than the sun—to soar on to the stars, and beyond.

BIBLIOGRAPHY

[1] JG Álvarez and C Bisagni. "Closed-form solutions for thermomechanical buckling of orthotropic composite plates". In: *Composite Structures* 233 (2020), p. 111622.

[2] JB Bai, RA Shenoi, and JJ Xiong. "Thermal analysis of thin-walled deployable composite boom in simulated space environment". In: *Composite Structures* 173 (2017), pp. 210–218.

[3] PM Bainum, N Hamsath, and R Krishna. "The dynamics and control of large space structures after the onset of thermal shock". In: *Acta Astronautica* 19.1 (1989), pp. 1–8.

[4] JR Blandino. "Analysis of thermal-mechanical interactions of STEM booms". In: *2nd AIAA Spacecraft Structures Conference* (2015). DOI: 10.2514/6.2015-1164.

[5] MK Chamberlain, SH Kiefer, and J Banik. "On-orbit structural dynamics performance of the roll-out solar array". In: *5th AIAA Spacecraft Structures Conference* (2018). DOI: 10.2514/6.2018-1942.

[6] SW Churchill and HHS Chu. "Correlating equations for laminar and turbulent free convection from a vertical plate". In: *International Journal of Heat and Mass Transfer* 18.11 (1975), pp. 1323–1329. DOI: 10.1016/0017-9310(75)90243-4.

[7] H Fernandes and X Maldague. "Use of infrared thermography to measure fiber orientation on carbon-fiber reinforced composites". In: *Proceedings of the 16th International Symposium on Applied Electromagnetics and Mechanics (ISEM), in Quebec City*. 2013.

[8] H Fernandes, H Zhang, and X Maldague. "An active infrared thermography method for fiber orientation assessment of fiber-reinforced composite materials". In: *Infrared Physics & Technology* 72 (2015), pp. 286–292.

[9] CL Foster et al. "Solar-array-induced disturbance of the Hubble space telescope pointing system". In: *Journal of Spacecraft and Rockets* 32.4 (1995), pp. 634–644.

[10] L Gaverina et al. "Pulsed Flying Spot Elliptic method for the estimation of the thermal diffusivity field of orthotropic materials". In: *International Journal of Thermal Sciences* 125 (2018), pp. 142–148.

[11] EE Gdoutos et al. "Development of the Deployable on-Orbit ultraLight Composite Experiment (DOLCE) for the Space Solar Power Project (SSPP) Demonstration Mission". In: *AIAA SCITECH 2022 Forum* (2022), p. 1266. DOI: 10.2514/6.2022-1266.

[12] DG Gilmore. “Spacecraft Thermal Control Handbook”. In: 2nd ed. The Aerospace Press, American Institute of Aeronautics and Astronautics, 2002. Chap. 4.

[13] HPMS Graphite. *Thermally Conductive Graphite*. 2009. URL: https://hpmsgraphite.com/thermallyconductivegraphite.

[14] L Holliday and J Robinson. “The thermal expansion of composites based on polymers”. In: *journal of Materials Science* 8 (1973), pp. 301–311.

[15] CH Jaggers, MJ Meshishnek, and JM Coggi. “Thermal Control Paints on LDEF: Results of M0003 sub-experiment 18”. In: *NASA. Langley Research Center, LDEF: 69 Months in Space. Part 3: Second Post-Retrieval Symposium*. 1993.

[16] PA Jones and BR Spence. “Spacecraft solar array technology trends”. In: *IEEE Aerospace and Electronic Systems Magazine* 26.8 (2011), pp. 17–28.

[17] RS Jones et al. “Thermal Conductivity of Carbon/Boron Nitride Heteronanotube and Boron Nitride Nanotube Buckypapers: Implications for Thermal Management Composites”. In: *ACS Applied Nano Materials* 6.17 (2023), pp. 15331–16105.

[18] R Kulkarni and O Ochoa. “Transverse and longitudinal CTE measurements of carbon fibers and their impact on interfacial residual stresses in composites”. In: *Journal of Composite Materials* 40.8 (2006), pp. 733–754.

[19] G Lebrun and J Denault. “Effect of annealing on the thermal expansion and residual stresses of bidirectional thermoplastic composite laminates”. In: *Composites Part A: Applied Science and Manufacturing* 41.1 (2010), pp. 101–107.

[20] C Leclerc. “Mechanics of Ultra-Thin Composite Coilable Structures”. PhD thesis. California Institute of Technology, 2020.

[21] K Liang, J Mu, and X Wang. “Nonlinear thermoelastic buckling analysis of thin-walled structures using a reduced-order method with mixed nonlinear kinematics”. In: *International Journal of Solids and Structures* 302 (2024), p. 112990.

[22] W Lu et al. “Application of high-thermal-conductivity diamond for space phased array antenna”. In: *AIAA SciTech 2024 Forum*. 2021, pp. 189–196. DOI: 10.1080/26941112.2021.1996211.

[23] W Luo and S Pellegrino. “Stability of Torsionally-Soft Deployable Structures Supporting Prestressed Membranes”. In: *Available at SSRN 4865607* (2024).

[24] J Mahaney and EA Thornton. “Self-shadowing effects on the thermal-structural response of orbiting trusses”. In: *Journal of Spacecraft and Rockets* 24.4 (1987), pp. 342–348.

[25] MA Marshall. “Dynamics of Ultralight Flexible Spacecraft During Slew Maneuvers”. PhD thesis. California Institute of Technology, 2022.

[26] MA Marshall, A Goel, and S Pellegrino. “Power-optimal guidance for planar space solar power satellites”. In: *Journal of Guidance, Control, and Dynamics* 43.3 (2020), pp. 518–535.

[27] HL McManus. “Control of space structure thermal deformation: an overview”. In: *Smart Structures and Materials 1993: Smart Structures and Intelligent Systems* 1917 (1993), pp. 545–554.

[28] D Mitchao et al. “Highly Thermal Conductive Deployable Membrane for Large Ka-band Active Phased Array Antenna”. In: *AIAA SciTech 2024 Forum*. 2024.

[29] M Murozono and EA Thornton. “Buckling and quasistatic thermal-structural response of asymmetric rolled-up solar array”. In: *Journal of spacecraft and rockets* 35.2 (1998), pp. 147–155.

[30] Buckeye Composites (a division of NanoTechLabs Inc.) *Material Technology*. 2009. URL: https://www.buckeyecomposites.com/material.html.

[31] DH Nguyen et al. “Thermal performance of the Hubble space telescope (HST) solar Array-3 during the disturbance verification Test (DVT)”. In: *4th International Symposium on Environmental Testing for Space Programmes*. 2001.

[32] S Ono et al. “Thermophysical properties of high-thermal-conductivity graphite sheet and application to deployable/stowable radiator”. In: *Journal of Thermophysics and Heat Transfer* 29.2 (2015), pp. 403–411.

[33] CJ Panetta et al. “Lessons learned from optics flown on the Materials International Space Station Experiment”. In: *Optical Interference Coatings*. Optica Publishing Group. 2013, MA–4.

[34] D Park, K Miyata, and H Nagano. “Thermal design and validation of radiation detector for the ChubuSat-2 micro-satellite with high-thermal-conductive graphite sheets”. In: *Acta Astronautica* 136 (2017), pp. 387–394.

[35] WJ Parker et al. “Flash Method of Determining Thermal Diffusivity, Heat Capacity, and Thermal Conductivity”. In: *Journal of Applied Physics* 32 (1961), p. 1679. DOI: 10.1063/1.1728417.

[36] S Pawlak et al. “Measurement of the anisotropic thermal conductivity of carbon-fiber/epoxy composites based on laser-induced temperature field: Experimental investigation and numerical analysis”. In: *International Communications in Heat and Mass Transfer* 139 (2022), p. 106401.

[37] JM Pederson, A Haraszti, and S Pellegrino. “Thermal Deformation of Ultrathin Composite Structures in a Vacuum Environment.” In: *AIAA SCITECH 2023 Forum* (2023). DOI: 10.2514/6.2023-1506.

[38] JM Pederson and S Pellegrino. “Thermal Deformation of Ultrathin Composite Structures in a Vacuum Environment.” In: *AIAA SCITECH 2024 Forum* (2024). DOI: 10.2514/6.2024-0412.

[39] HH de Sénarmont. *Mémoire sur la conductivité des substances cristallisées pour la chaleur: second mémoire*. Imprr. de Bachelier, 1848.

[40] R Spencer et al. “Fiber orientation evaluation in reinforced composites using digital image correlation and thermal excitation”. In: *Composites Part B: Engineering* 234 (2022), p. 109713.

[41] OR Stohlman. “Coupled radiative thermal and nonlinear stress analysis for thermal deformation in large space structures”. In: *5th AIAA Spacecraft Structures Conference* (2018). DOI: 10.2514/6.2018-0448.

[42] OR Stohlman and E Loper. “Thermal deformation of very slender TRAC booms”. In: *3rd AIAA Spacecraft Structures Conference* (2016). DOI: 10.2514/6.2016-1469.

[43] OR Stohlman, ER Loper, and TE Lockett. “Temperature-driven shape changes of the near earth asteroid scout solar sail”. In: *International Symposium on Solar Sailing*. NF1676L-25046. 2017.

[44] Y Takeda et al. “Thermo-mechanical Evaluation of Multilayer Graphite Sheet Structures for Space Deployable Antennas”. In: *AIAA SciTech 2024 Forum*. 2024.

[45] K Than. *Solar Power at All Hours: Inside the Space Solar Power Project*. 2023. URL: https://magazine.caltech.edu/post/sspp-space-solar-power-project.

[46] C S T The Composites Store. *Comparison Data for Pultruded Shapes*. 2018. URL: https://www.cstsales.com/rod_comp.html.

[47] EA Thornton. “Thermal Structures for Aerospace Applications”. In: 1st ed. American Institute of Aeronautics and Astronautics, 1996. Chap. 4, 9.

[48] EA Thornton, GP Chini, and DW Gulik. “Thermally induced vibrations of a self-shadowed split-blanket solar array”. In: *Journal of Spacecraft and Rockets* 32.2 (1995), pp. 302–311.

[49] EA Thornton and DB Paul. “Thermal-structural analysis of large space structures-an assessment of recent advances”. In: *Journal of Spacecraft and Rockets* 22.4 (1985), pp. 385–393.

[50] T Tian and KD Cole. “Anisotropic thermal conductivity measurement of carbon-fiber/epoxy composite materials”. In: *International Journal of Heat and Mass Transfer* 55.23-24 (2012), pp. 6530–6537.

[51] UK Ubamanyu. “Time-dependent Failure of Thin-ply Composite Laminates”. PhD thesis. California Institute of Technology, 2023.

[52] AA Yahia and EP Del Barrio. “Thermal systems modelling via singular value decomposition: direct and modular approach”. In: *Applied Mathematical Modelling* 23.6 (1999), pp. 447–468.

[53] J Zhang, A Gupta, and J Baker. “Effect of relative humidity on the prediction of natural convection heat transfer coefficients”. In: *Heat transfer engineering* 28.4 (2007), pp. 335–342.

[54] D Zhao et al. “Measurement techniques for thermal conductivity and interfacial thermal conductance of bulk and thin film materials”. In: *Journal of Electronic Packaging* 138.4 (2016), p. 040802.

Appendix A

MEASUREMENT OF ORTHOTROPIC CONDUCTIVITY OF THIN MATERIALS VIA LASER HEATING

To obtain measured estimates of the orthotropic thermal conductivity of the thin composite laminates forming the unit structures used in experiment, a modified version of the typical "laser flash" method was designed and performed in-house.

A.1 Background

The thermal conductivity of the composite laminates used to build space structures has a significant potential impact on the structures' deflection; previous studies have confirmed that thermal conductivity in the direction transverse to the composite fibers is the factor effectively dictating the thermal gradients that cause deflections [37]. Therefore, estimating the orthotropic thermal conductivities of our composite laminates—i.e. parallel to and transverse to the carbon fibers—was crucial to predicting temperature fields on the structures accurately.

Challenges of Thermal Conductivity Measurement

Measuring thermal conductivity in bulk materials is usually straightforward; there exists many testing procedures to do so, with many companies and organizations investing in and owning the often sophisticated testing equipment required. (For the purposes of this discussion, measuring thermal diffusivity is synonymous with measuring thermal conductivity, since the two quantities are related by the specific heat and density of the material; these were measured for our laminates and therefore known.) However, the simplest, most common, and least expensive methods, such as the guarded heat flow method, rely on much larger sample thicknesses (on the scale of centimeters) than the laminates used in this work [54]. Merely stacking thicknesses of thin-ply laminates will also not work, due to the large amount of interfacial thermal resistance induced by such a technique.

Many techniques for analyzing thin materials do exist, but the current state-of-the-art thermal conductivity measurement technique for materials too thin for guarded heat flow analysis is the laser-flash method; by briefly illuminating a sample with a pulsed laser and measuring the subsequent adiabatic temperature rise, the thermal diffusivity can be derived from Parker's Law, and subsequently converted into the

thermal conductivity [35]. However, the method assumes isotropy in the material to be tested; Parker's seminal paper on the method, as well as the law bearing his name that relates thermal diffusivity to half the thermal rise time, strictly only applies to heat conducting at the same rate in all directions [35]. In this technique, the laser illumination is ring-shaped and assumed to propagate toward the central measurement point equally from all directions; an orthotropic material like our laminates breaks this fundamental assumption, and therefore a different approach is needed.

Laser Flash and Composite Laminates

For carbon-fiber composite materials specifically, many research studies have used laser heating on thick orthotropic laminates; when heated by a laser and observed with a thermal camera, the layup displays a hot spot, which quickly becomes an ellipse as the carbon fibers conduct heat more efficiently than the surrounding matrix. However, the vast majority of studies simply stop here, using the technique only to determine the orientation of carbon fibers in samples of unknown orientation [7][8][40].

However, using such heating to determine directional thermal conductivity has clear precedent. Such analysis was first suggested, in fact, by M. Henri de Sénarmont in 1847; his experiments, generating elliptical isotherms by exposing orthotropic materials to a point heat source, demonstrated that the ratio of the major and minor axes was proportional to the square root of the ratio of the in-plane thermal conductivities [39].

Accordingly, a few studies have fact successfully measured orthotropic thermal conductivities by correlating infrared thermography of laser heating with analytical or simulation-based models. Gaverina et al., for example, used a pulsed "flying" laser spot technique to produce multiple thermal ellipses over the surface of a sample, using a sophisticated analytical model to determine in-plane diffusivities at those points [10]. More accessibly, Pawlak et al. successfully used a similar pulsed-laser-heating technique on a 19-layer composite laminate, showing that such a method is feasible for this work's 3- and 7-layer laminates. Pawlak used a digital-twin-style three-dimensional finite-element solver, one that iteratively varies in-plane conductivity parameters until agreement with experimental values is reached [36].

Continuous Laser Heating

However, the above laser-flash techniques all relied on high-power precision-pulsed lasers, which are expensive, require tuning to one's setup, and run the risk of overheating the sample if improperly timed. The main advantage of using a pulse is the approximation of an adiabatic heating condition, where little to no radiative or convective cooling has taken place by the time that the sample's conductive isotherms have developed.

A technique that used a laser of lower power illuminating the sample for a longer period of time, while not having the advantage of "adiabatic" conditions, would nonetheless be more practical and expedient if the effects of radiative and convective cooling were accounted for. This is the approach used in the present technique.

Previous Measurement

As a start, a sample of the 3-ply flange laminate used in the unit structures (see Chapter 2) was tested in a standard laser-flash apparatus by TA Instruments; the sample was flashed with an elliptical laser pulse, the transient temperature rise at the center was measured as a function of time, and the thermal diffusivity was calculated according to Parker's method [35].

Since the technique presumed the sample to be isotropic, the value produced by this analysis (which is here called k_{iso}, 0.66 W/m•K) was somewhere between the actual in-plane thermal conductivities; the conductivity of the laminate along the carbon fibers is here called k_1, and that transverse to the fibers is called k_2.

A.2 Methodology

Experimental Setup and Procedure

To obtain experimental temperature field data, a standard tabletop 30-mW laser (Melles-Griot) was used to *continuously* illuminate a coupon of composite laminate at a single point, while a FLIR thermal camera measured the 2D steady-state temperature rise of the coupon. A piece of black-painted Kapton was illuminated in the same manner to serve as a calibration target, since its emissivity, thermal conductivity, and thickness were all well-characterized and isotropic. The laser heating rig is pictured in Figure A.1, along with an example image during heating.

Correlation with Simulation

This temperature rise was then compared to a COMSOL model of the laser heating rig and sample, with the parameters of laser power, beam profile, and convective

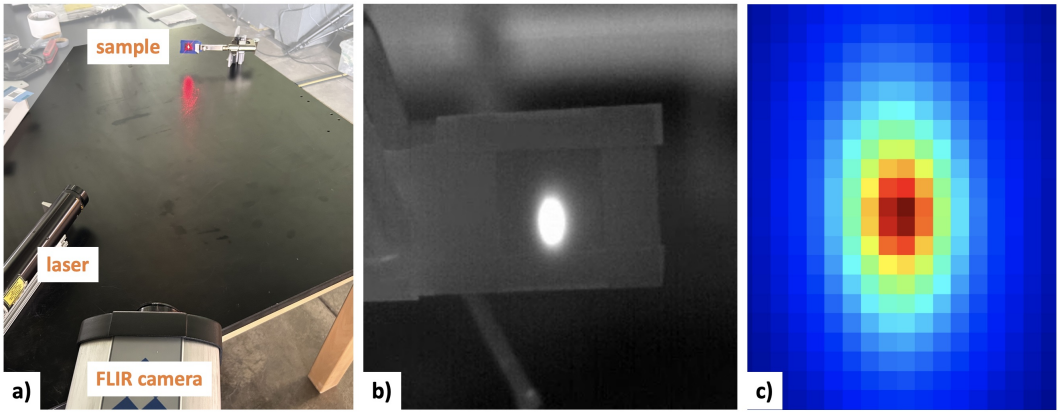

Figure A.1: a) The laser rig heating a composite laminate sample; b) raw IR camera data; c) zoomed and colored. Note elongation of spot from fiber conduction.

effects modified until they matched the heating experienced by the isotropic Kapton calibration target. Laser heating was modeled by a point source combined with a nonphysical mask with an aperture; adjusting the point source power and location, as well as the size of the mask hole, enabled precise tuning of the beam profile to the experimentally observed one. The thermal conductivities of the simulated sample in both orthogonal directions were then modified via parameter search until the temperature response best matched experimental data.

To more quickly accomplish this parameter search, an additional COMSOL model was created that heated the same sample using a ring of illumination heating (via a ring-shaped mask); this rig used a pulse of heating to mimic the laser-flash rig used by TA Instruments. Running the simulation with different thermal conductivities, the thermal rise time of an isotropic sample of conductivity k_{iso} was matched with that of various pairs of k_1 and k_2; setting a value of k_1 and varying k_2 until the thermal rise time matched the k_{iso} case generated a pair of in-plane conductivities that matched the known laser-flash response of the laminate. These viable pairs of in-plane conductivities were then iterated through in COMSOL.

Comparing the COMSOL results to the experimental data was accomplished using a MATLAB script; by perspective-warping, cropping, and down-sampling the fine-resolution COMSOL data, the script was able to accurately compare the response to the more pixelated thermal camera imagery. A simple similarity scoring algorithm was used to judge how accurately the two fields matchd, taking the lowest of several resamplings of slight translations of the COMSOL data to ensure that the two fields were correctly aligned.

After this parameter searching, the conductivities that best matched were 0.99 W/m•K parallel to the carbon fibers and 0.27 W/m•K in the perpendicular direction, showing that the laminates used in this work conduct heat approximately four times better along the fibers than transverse to them. See Figure A.2 for a diagram of the COMSOL model, as well as the two predicted temperature fields as compared with the experimental data.

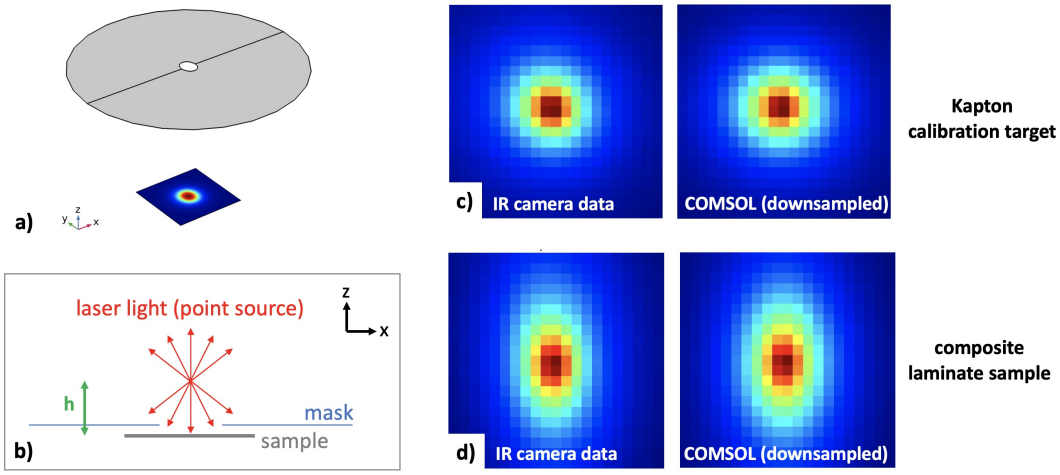

Figure A.2: a) COMSOL model showing sample and nonphysical laser mask; b) detail of beam profile generation; c) experimental data from calibration target and d) laminate, both compared with COMSOL temperatures.

These values were the ones used as material properties of the sample in the COMSOL analyses of the experimental chamber in Chapter 3 and the structure models of Chapter 4, as well as the thermal properties used by the Thermal Desktop models in Chapter 5.

This relatively low-tech approach provides a much simpler experimental technique for calculating thermal conductivities of thin orthotropic materials, and has the potential to make such thermal properties more readily obtainable for future analyses of space structures and beyond.

Appendix B

THERMAL BUCKLING OF THIN SPACE STRUCTURES

To justify the claims of thermally induced buckling shown in this thesis, especially those observed for the simulated structures in Chapter 5, a brief explanation of buckling under thermal loads is presented, focusing on the finite-element stiffness matrices and their eigenvalues.

B.1 Background

Many thin structures experience a "bifurcation" of deflection response under an increasing load—that is, at a certain level of loading, the force increment needed to produce an additional amount of deflection is greatly decreased or even negative. At this point, under force-control boundary conditions, the structure will experience rapidly increasing deflections or even "snap-through"—a sudden jump from one configuration to another. Either of these phenomena, for our purposes, would be considered "buckling", and would usually cause the structure to lose its stiffness. An example would be the bending of a steel tape measure lengthwise until it suddenly flattens; regardless of whether the bending occurs in the same sense or opposite sense as the original tape curvature, the buckled tape has much lower bending stiffness than the original configuration.

The point at which a given load will cause buckling can be determined by applying the load incrementally until buckling is encountered. In practice, this is accomplished by applying a unit load to the structure, multiplying it by some multiplier, and solving for the value of multiplier required. Buckling induced by both mechanical and thermal loads can be predicted in this way, even simultaneously; for example, Alvarez and Bisagni calculate various such scenarios in analytical form and in Abaqus [1].

As loads are applied to the finite-element model of a structure, its stiffness matrix will change to reflect the unique combination of loads; this means that the stiffness of the structure is altered by the loads applied to it. If the eigenvalues of this matrix are examined, they should correspond to the magnitudes of additional loading required to buckle the structure, as shown in [1]. The corresponding eigenmodes of the matrix, when plotted on the structure, represent shapes that the structure will deform into

if loaded in that manner. This implies that if any of these eigenvalues are zero, the structure has lost stiffness in that loading configuration; if any eigenvalues are negative, the structure has been loaded beyond the buckling limit such that one would have to apply the force in the opposite direction to stop the deformation.

Buckling of Structures in This Work

Applying these ideas to the thin-shell structures studied in this thesis, one realizes that if either of the two longerons comprising a structure were buckled, the resulting loss of stiffness would almost certainly compromise whatever science or mission the structure was supporting. Therefore, material configurations that buckle under ordinary sunlight must be replaced with ones that do not; this was the rationale for adding a highly conductive graphite layer mid-way through Chapter 5 in order to have meaningful dynamic simulation results. For a longeron to buckle, in turn, one of the flanges must flatten, which is known to occur during certain solar heating conditions.

This failure "mode" implies that, if the stiffness matrices of the structures are examined as the solar flux heat load is increased, the eigenvalues should move and become zero or negative when the structure experiences flattening or buckling. This hypothesis will therefore be tested by examining the finite-element stiffness matrices of the structures in this work.

Since the stiffness matrices for even a 25-cm structure are rather large (2,000-4,000 entries square) and therefore time-consuming to export, simulations were run with the solar flux load at 5-6 discrete levels, with the stiffness matrix extracted for each level. Both COMSOL and Abaqus were used to model the structure, and therefore both were used to examine this phenomenon.

B.2 COMSOL / MATLAB Stiffness Analysis

The COMSOL simulation of the 25-cm structure model (presented at the start of Chapter 5) was re-run with solar flux levels of 0, 100, 500, 1,000, and 1,260 W/m^2, and the stiffness matrix was exported for each level into MATLAB using LiveLink™ for MATLAB®. The ten smallest eigenvalues of this stiffness matrix were calculated using the MATLAB eigs() function; the eigenvalue results are plotted in Figure B.1, with the deflected structure shapes for each flux level shown in Figure B.2. Note that in Figure B.1, only eigenvalues that converged are plotted; this means that, except for 0 W/m^2, only 1-2 eigenvalues converged for the highest solar fluxes, with the rest being positive.

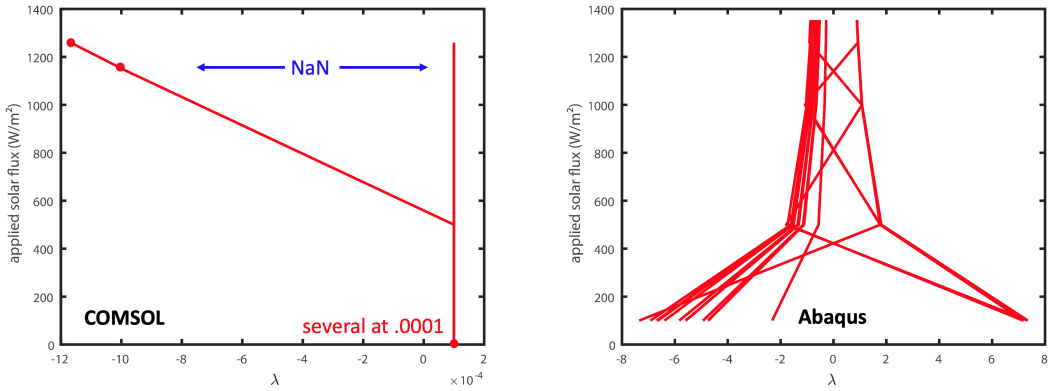

Figure B.1: A comparison of stiffness eigenvalues for the 25-cm structure, extracted from the COMSOL and Abaqus models.

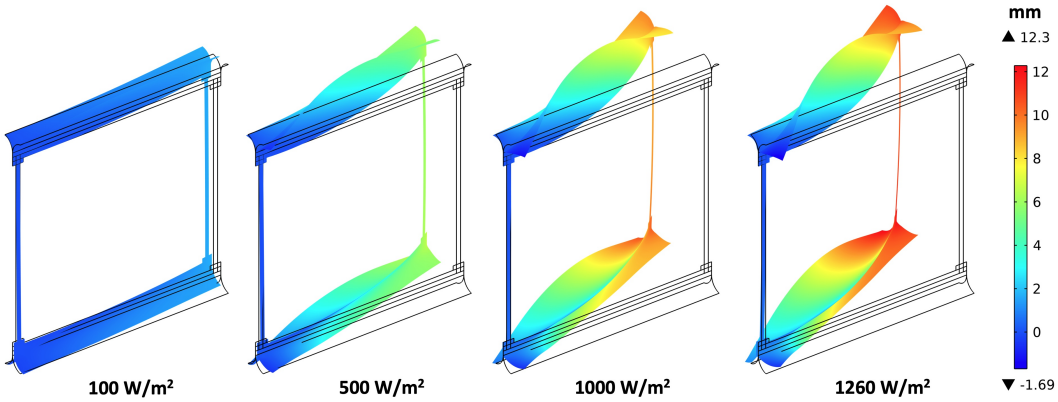

Figure B.2: Deflected shapes for the 25-cm structure in COMSOL at various solar flux levels.

The behavior of the eigenvalues matches the intuition presented in the introduction: the eigenvalues start out positive, and a few become negative as the structure becomes more and more deformed and buckled. However, the smallest ten requested eigenvalues for 0 W/m^2, though positive, were extremely small, implying that the structure has many modes of deforming for which the structure is very soft. The 25-cm structure is known to be relatively soft in small-angle torsion, but the other modes are somewhat less clear.

B.3 Abaqus Stiffness Analysis

Extracting stiffness eigenvalues from MATLAB took a different form: the steady-state Abaqus / Thermal Desktop loop described in Chapter 5 was modified to run in only one open loop—i.e. run a Thermal Desktop analysis, apply the temperature field as a heat load to Abaqus, and run the Abaqus analysis—for the same levels

of solar flux as the COMSOL model. In addition, the Abaqus model was modified to run a Buckle analysis step rather than a Static, General step; this generated the relevant eigenvalues and eigenmodes directly, without the need for exporting the stiffness matrix and calculating its eigenvalues.

Figure B.1 displays the eigenvalues calculated by this buckle analysis step, while Figure B.3 shows the corresponding eigenmode shapes. The eigenvalues generated by this analysis are very different than the COMSOL analysis, both in magnitude and change with respect to solar flux level: they not only differ by three orders of magnitude, but start out larger and grow closer to 0 as solar flux increases. Furthermore, the eigenvalues actually become more negative as the mode shapes become higher: Mode 1's eigenvalue of -2.32 is smaller in magnitude than Mode 13's eigenvalue of -6.92.

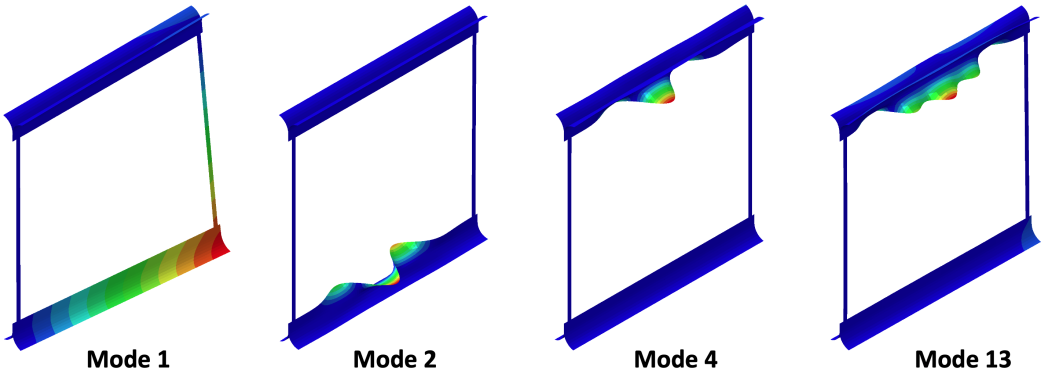

Figure B.3: Eigenmode shapes for the 25-cm structure in Abaqus.

These differences are difficult to understand. If not erroneous, they suggest a significant change of behavior may occur in the case of non-uniform thermal loading—which is the case for the present study. While many publications have focused on thermal buckling of plates under various mechanical loadings and boundary conditions, but almost always under uniform temperature increases [1, 21], buckling situations involving the scaling of a non-uniform thermal load are apparently much less common.

It is also important to note that the thermal gradients applied to the structure were strictly positive, in the sense that starting from a uniform room-temperature field, the temperature of each element either remained the same or increased. This contrasts with the steady-state and dynamic orbital simulations of Chapter 5, where the much colder radiative background of space caused negative temperature changes from the

initial room-temperature field. This detail is important, since it implies that non-intuitive buckling eigenvalue behavior may arise from strictly increasing thermal loads: for example, a negative multiplication of a non-uniform temperature load may be required to compress some part of the structure relative to another, thereby implying the existence of a negative eigenvalue.

B.4 Future Work

To understand this non-intuitive eigenvalue behavior, the gap in knowledge between the well-characterized thermal buckling of flat plates and the much-less-known thermal buckling of more complicated structural geometries subject to thermal gradients must be addressed. A recommendation for bridging this gap would be the study of a single tape spring, the buckling behavior of which, under mechanical loads, is near-canonical in the field of thin-shell simulation. Application of thermal loads directly to various regions of mesh elements would offer a rich testing ground for investigating how geometrically non-uniform temperature fields translate into buckling behaviors, as well as how their corresponding eigenvalues and eigenmodes change.